Università
degli Studi
di Napoli
Federico II

Facoltà di
Ingegneria

SEISMIC ISOLATION AND ENERGY DISSIPATION: THEORETICAL BASIS AND APPLICATIONS

Maria Rosaria Marsico

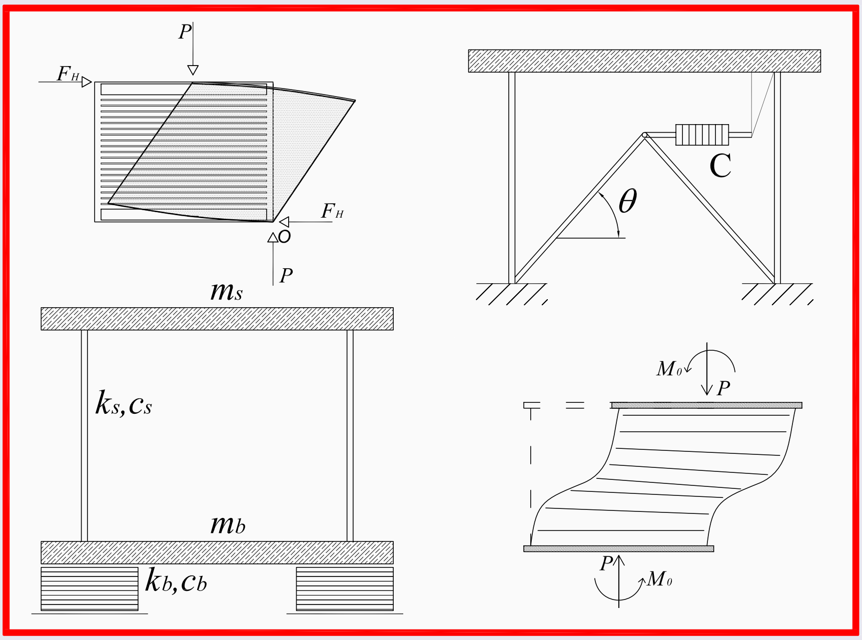

Dottorato di Ricerca in Ingegneria delle Costruzioni

Università degli Studi di Napoli Federico II
Facoltà di Ingegneria

Maria Rosaria Marsico

SEISMIC ISOLATION AND ENERGY DISSIPATION: THEORETICAL BASIS AND APPLICATIONS

Tesi di Dottorato
XXI ciclo

Il Coordinatore
Prof. Ing. Federico M. MAZZOLANI

Dottorato di Ricerca in Ingegneria delle Costruzioni

Ai miei cari genitori
con immenso grazie

ABSTRACT

The protection of the building from seismic events is a fundamental phase in the structures design should be introduced to avoid the loss of lives especially when it occurs in developing countries. This natural calamity produces social and economic consequences because a lot of people are killed by the collapse of brittle heavy unreinforced masonry or poorly constructed concrete buildings. The engineers can use in their professional practice seismic isolation or energy dissipation devices to prevent these disasters. The first ones are elements integral for the stability, the second ones are elements not forming part of the gravity frame system. It is spread to protect important or special structures but there is an increasing interest for using these devices in houses, schools and hospitals, especially in those countries with a large risk of earthquakes. The problem is to simplify the seismic design in order to propagate this project philosophy in the professional practice.

An example of seismic isolation analysed within this research is the intervention on the "Santuario delle Madonna delle Lacrime" in Siracusa, Italy. The seismic retrofit was made substituting the bearings supporting the impressive dome with sliding seismic isolators equipped with elasto-plastic dissipators. Each old bearing allowed the geometrical variations of the diameter of the base ring

supported the cover due to thermal and tensional variations inside itself, while the displacements in tangential direction were prevented. The new anti-seismic devices, installed between the 22 columns of the structure and the truncated-conical dome during the raising and lowering phases, are unidirectional bearings including elasto-plastic dissipators with “moon’s sickle” shape, able to transmit the horizontal seismic action on the dome to the columns through their elasto-plastic movement. The elastic behaviour of a “moon’s sickle” element up to the achievement of the steel yield stress in the most stressed point was analytically examined, in order to compute the elastic stiffness that approximately corresponds to the one experimentally observed. A Finite Element Structural Analysis Program has been used to construct the simplified and the complete numerical model of the structure, able to simulate its real behaviour. In the first one model, the dome of the Sanctuary has been assumed as a rigid body supported on 22 r.c. piers uniformly distributed along the circular perimeter of the Upper Temple’s plan. An analytical model was worked up and compared with the model developed through SAP-2000 software. The seismic input for the numerical analyses is represented by 7 couples of artificial accelerograms compatible with the elastic response spectrum defined by the new code, (Ministerial Decree of 14 January 2008, G.U. n. 29 del 4.02.2008 suppl. ord. n° 30) and for each accelerogram a duration of 26s has been assumed. It was therefore decided to reactivate the monitoring system, which contained some breakdown elements due to the default of maintenance, through an intervention of overtime maintenance and adaptation to the new constraint scheme of the dome, in order to finally start the operations of monitoring and continuous control of the construction. This structure has been recently included among those of the Italian network of buildings and bridges permanently monitored by the Italian Department of Civil Protection of the Seismic Observatory of Structures (OSS).

The energy dissipation study has been carried out with an extensive set of dynamic experimental tests, named JetPacs - Joint Experimental Testing on Passive and semi-Active Control Systems - within the topics no.7 of the ReLuis Project (University Network of Seismic Engineering Laboratories). The analysis have been performed by using a 2:3 scaled steel braced frame, available at the Structural Engineering Laboratory of the University of Basilicata in Potenza, Italy. During the experimental campaign, the structural model was subjected to three different sets of natural or artificial earthquakes, compatible with the response spectra of the Eurocode 8 and of Italian seismic code (OPCM 3431, 2005) for soil type A, B and D. The dissipation systems, developed with different materials and technologies, consist of six different types of passive or semi-active energy dissipating devices with different behaviours. The JETPACS mock-up model is a two storeys one-bay steel frame with composite steel-reinforced concrete slabs. It is well known that the efficacy of semi-active devices in controlling the dynamic response of a structure increases with the increase of the ratio between the first vibration period of itself and the time reactivity of the device.

In order to elongate the vibration periods of the test frame, a modified symmetrical configuration has been obtained by adding four concrete blocks on each floor. Instead the efficacy of passive and semi-active energy dissipating devices in controlling the torsional behavior was been considered with only two additional concrete blocks on both the first and the second floors, creating eccentricity with respect to the mass center. Therefore the model has been experimentally analyzed in three different configurations namely: i) bare frame without any additional mass, designated as CB; ii) frame with four additional concrete blocks at first and second floors close to each corner, designated as CS; iii) frame with two additional concrete blocks on first and second floors placed eccentric with respect to mass center, designated as CN.

Based on the detailed description of the JETPACS Mock-up model, attempt has been made to closely simulate the test specimen using the SAP-2000 software to match the experimental results of the dynamic characterization tests conducted at Structural Engineering Laboratory of the University of Basilicata. An uniform increase in thickness of 17 mm in the reinforced concrete slab has been considered, which is equal a certain increase of mass for each floor. The dynamic characteristics of the analytical model strongly depend on the extent of connectivity between the floor beam and the reinforced concrete slab. It was decided to completely ignore the rigidity between the floor beams and r.c. slab in the further analysis because during model fabrication, connections were quite weak and made just to support the vertical loads.

The most common devices used for isolated buildings are multilayered laminated rubber bearings. They can be constituted by dowelled shear connectors or held in place by recessed plate connections. At the Earthquake Engineering Research Center of the University of California in Berkeley, under the guide of Prof. James M. Kelly, a study on the buckling and roll-out instability behaviour of non-bolted bearings under lateral and vertical load was worked up.

The hypothesis that the onset of instability under lateral displacement is the critical pressure p_{crit} applied to the reduced area A_r was adopted to analyse the former aspects. This methodology rises observing that a large number of smaller bearings is less expensive than a smaller number of large bearings with variable sizes that need to be designed for different column loads. In fact the idea is that it is possible to adjust to the variable column loads by using one, two, three, four or five bearings under each column. The only question of concern is that of the stability of a set of bearings as compared to a single bearing with the same horizontal stiffness. Two case studies, in which the replacement of five small bearing with a single big bearing, have been examined.

The bearings have been subjected to the downward displacement of the top due to horizontal displacement and vertical load applied. This shortening is fundamental in the design process of the bearing itself and can be considered by the buckling analysis. Three different bearing configurations under vertical loads and lateral displacements have been studied and the results compared with a numerical model available at UCB to simulate the real behaviour.

The shape of the isolators usually is circular, rectangular or long strip. The latter are often used in buildings with masonry walls. The buckling and the roll-out displacement for an infinite strip bearing with width 2b was analyzed and it has been defined the ratio f, between the load and the critical load applied to the reduced area, to calculate the roll-out.

New formulas have been elaborated to design the non-bolted bearings in order to adopt them in a future seismic code updating.

AKNOWLEDGEMENTS

At the end of this wonderful and interesting stage of my life I can finally say that part of my dreams have come true, which seemed so difficult to fulfil.

I sincerely thank Prof. Giorgio Serino who has always relied on my competence and has offered me this great possibility. I have been very lucky to meet him since he has been an excellent teacher and a paragon of life. He has always encouraged me in the most difficult moments and conveyed me enthusiasm and passion.

I thank Prof. Federico M. Mazzolani of the Department of Structural Engineering of the University of Naples for his careful and helpful guidance for this research work. I am also grateful to Prof. James M. Kelly of the Department of Structural Engineering of the University of California and participating faculty of the Earthquake Engineering Research Center (EERC) of the University, for his valuable help during my stay at Berkeley as a Visiting Scholar.

I am extremely grateful to all the Faculty members of the Department of Structural Engineering for their direct and indirect support during my research. My special thanks go to both Prof.

Gaetano Manfredi, the Director of the Department, and Prof. Edoardo Cosenza, the Dean of the Faculty of Engineering, for their administrative assistance.

A great thanks to my parents who have always supported me and have always been an example of life and love; I thank my mother for her unconditioned love and care and my father for handing me down his love for culture and research.

I also thank my sisters Valeria and Federica, and the rest of my family, for the deep respect they gave me every day.

My final thanks goes to Gigi whose love has always pushed me to go on and not give up.

Maria Rosaria

TABLE OF CONTENTS

LIST OF FIGURES

LIST OF TABLES

Chapter I

1. SEISMIC ISOLATION

Many early example of innovative earthquake resistant designs referred to as base isolation or seismic isolation, are spread in different places in the word. Many mechanisms, invented over the past century to protect buildings from damaging earthquakes, use some type of support that uncouples them from the ground.

The concept of base isolation is quite simple. The isolation system educes the effect of the horizontal components of the ground acceleration by interposing structural elements with low horizontal stiffness between the structure and the foundation. This gives the structure a fundamental frequency that is much lower than both its fixed-base frequency and the predominant frequencies of the ground motion. The first dynamic mode of the isolated structure involves deformation only in the isolation system, the structure above being, for all intents and purposes, rigid. The higher modes producing deformation in the structure are orthogonal to the first mode and consequently, to the ground motion. These higher modes do not participate in the motion, so that if there is high energy in the ground motion at these higher frequencies, this energy cannot be transmitted into the structure. The isolation system does not absorb the earthquake energy, but deflects it through the dynamics of the system. Although a certain level of damping is beneficial to suppress any possible resonance at the isolation frequency, the concept of isolation does not depend on damping. In fact, excessive damping can reduce the effectiveness of the isolation system by acting as a conduit for energy to be induced in the higher modes of the isolated structure.

Most recent examples of isolated buildings use multilayered laminated rubber bearings -with steel reinforcing layers as the load-carrying component of the system. Because of the reinforcing steel plates, these bearing are very stiff in the vertical direction but are soft in the horizontal direction, thereby producing the isolation effect. These bearings are easy to manufacture, have no moving parts, are unaffected by time, and resist environmental degradation (Kelly, 2004).

In the United States the most commonly used isolation system is the lead-plug rubber bearing. These bearings are multilayered, laminated elastomeric bearings with lead plugs inserted into one or more circular holes. The lead plugs are used to incorporate damping into the isolation system. Although some isolation systems are composed of only lead-plug rubber bearings, in general they are used in combination with multilayered elastomeric bearings (which do not have lead plugs).

The second most common type of isolation system uses sliding elements. This approach assumes that a low of friction will limit the transfer of shear across the isolation interface -the lower the coefficient friction, the lesser the shear transmitted.

Japan is at the forefront of applying isolation method for earthquake-resistant design, with the completion of the first large base-isolated building in 1986. All base isolation projects in Japan are approved by a standing committee of the Ministry of Construction. Many of the completed buildings have experienced earthquake, and in some cases it has been possible compare their response with adjacent conventionally designed structures. In every case the response of the isolated building has been highly favourable, particularly for ground motions with high levels of acceleration.

The isolation method continues to increase in Japan, especially in the aftermath of the 1995 Kobe earthquake.

To date, most base isolation applications have focused on large structures with sensitive or expensive contents, but there is an increasing interest in the application of this technology to public housing, schools, and hospitals in developing countries. The challenge in such applications is to develop low-cost isolation system that can be used in conjunction with local construction methods, such as masonry block and lightly reinforced concrete frames. A number of base-isolated demonstration projects have been completed, are currently under construction, or are in the planning phase. In most cases, an identical structure of fixed-base construction was built adjacent to the isolated building to compare their behaviour during earthquake.

Although isolation techniques have been used for new construction of recently completed buildings, the 1989 Loma Prieta and 1994 Northridge earthquakes in California stimulated much interest in applying these techniques for the retrofit of historical structures. A basic dilemma exists in restoring historic buildings vulnerable to strong ground shaking or damaged in the past by earthquakes. The conservation architect, concerned primarily with preserving a building's historical and cultural value by maintaining its original aesthetic, is adamant for minimum intervention and the conservation of the original structural forms and materials. Safety of the structure is a secondary consideration.

In contrast, the structural engineer is equally adamant to strengthen the structure to a level that will protect life safety and minimize future damage to the repaired structure (Bozorgnia and Bertero, 2004).

1.1 Theoretical Basis of seismic Isolation

Insight into the behaviour of an isolated building can be obtained by using a simple 2-DOF model in which a mass, m_s, representing the superstructure of the building is carried on a linear structural system on a base mass, m_b, which in turn is supported on an isolation system. All the structural elements are assumed to be linearly elastic with linear viscous damping. Because most isolation systems are intrinsically nonlinear, this analysis will be only approximate for such systems; the effective stiffness and damping will have to be estimated by some equivalent linearization process. The parameters of the model are shown in Figure 1.1.

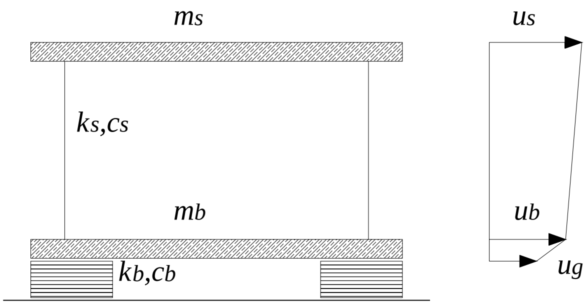

Figure 1.1 Parameters of two degree of freedom isolation system model.

A very detailed analysis of the response of this model to ground motion input is given by Kelly (1990). The important results are summarized here. The main results are expressed in terms of relative displacements, v_s, v_b derived from the absolute displacements, u_s, u_b, u_g, by $v_s = u_s - u_b$ *and* $v_b = u_b - u_g$.

The fixed-base structural frequency, $\omega_s = \sqrt{\frac{k_s}{m_s}}$, and the isolation frequency (the frequency if the superstructure were rigid), $\omega_b = \sqrt{\frac{k_b}{(m_s + m_b)}}$, are assumed to be very widely separated. Parameter $\varepsilon = \frac{\omega_b^2}{\omega_s^2}$ characterizes this separation between the two frequencies and varies between 10^{-1} and 10^{-2}. A mass ratio $\gamma = \frac{m_s}{(m_s + m_b)}$, is also required and is always less than 1.

The damping factors for the structure and isolation system, β_σ and β_b, respectively $\beta_\sigma = \dfrac{c_s}{(2m_s\omega_s)}$ and $\beta_b = \dfrac{c_b}{\left(2\omega_b\left(m_s + m_b\right)\right)}$, are of the same order of magnitude as ε.

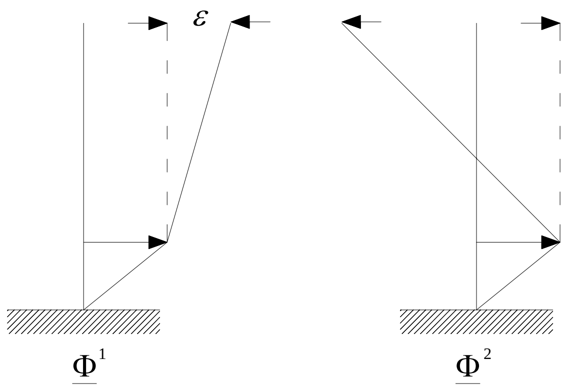

Figure 1.2 Mode shapes of two degree of freedom isolation system model.

Figure 1.2 shows the mode shapes of two degree of freedom isolation system model. The structure is nearly rigid in $\underline{\Phi}^1$, whereas $\underline{\Phi}^2$ involves deformation in both the structure and the isolation system, with the displacement of the top of the structure of the same order as the base displacement, but opposite in direction.

The frequency of the first mode can be thought of as the modification (due to the flexibility of the superstructure) of the frequency of the isolated model when the structure is rigid, and because the structure is stiff as compared to the isolation system, the modification is small. The second mode is very close to a motion where the two masses, m_s, m_b, are vibrating completely free in space about the center of mass of the combined system.

The practical significance of this result is that high accelerations in the second mode of an isolated structure do not need to be accompanied by a large base shear.

1.2 Seismic Isolation Hardware

The base isolation technology is used in many countries and there are a number of acceptable isolation systems, whose mechanisms and characteristics are well understood.

Elastomeric-Based Systems: in 1969 was used a system with large rubber blocks without steel reinforcing plates. The system was tested on the shake table at the Earthquake Engineering Research Center (EERC) in 1982 (Staudacher, 1982). Many other buildings have been built on natural rubber bearings with internal steel reinforcing plates that reduce the lateral bulging of the bearings and increase the vertical stiffness.

Low-Damping Natural and Synthetic Rubber Bearings (LDRB): have been widely used in Japan in conjunction with supplementary damping devices, such as viscous dampers, steel bars, lead bars, frictional devices etc. The isolators typically have two thick steel end plates and many thin steel shim.

Lead-Plug Bearing (LRB): are laminated rubber bearings similar to LDRBs, but contain holes into which one or more lead plugs are inserted. The bearings have been used to isolate many buildings, and buildings using them performed well during the 1994 Northridge and 1995 Kobe earthquake.

Figure 1.3 LRB under hospital structure (Los Angeles, California).

High-Damping Natural Rubber (HDNR) Systems: the development of a natural rubber compound with enough inherent damping to eliminate the need for supplementary damping elements was achieved in 1982, in the United Kingdom. The damping is increased by adding extra-fine carbon black, oils or resins, and other proprietary fillers.

Figure 1.4 Example of high-damping rubber bearing: Hearst Memorial Mining Building retrofit project.

Isolation Systems Based on Sliding: a considerable amount of theoretical analysis has been done on the dynamics of structure on sliding systems subjected to harmonic input or to earthquake input. The most commonly used materials for sliding bearings are unfilled or filled Polytetrafluoroenthylene (PTFE or Teflon) on stainless steel, and the frictional characteristics of this system are dependent on temperature, velocity of interface motion, degree of wear and cleanliness of the surface.

TASS System: the TASS system was developed by the TASISEI Corp. in Japan (Kelly, 1988) where the entire vertical load is carried on Teflon-stainless steel elements, with laminated neoprene bearings carrying no load used to provide recentering forces.

Friction Pendulum System (FPS): is a frictional system that combines a sliding action and a restoring force by geometry. The FPS isolator has an articulated slider that moves on a stainless steel spherical surface. The side of the articulated slider in contact with the spherical surface is coated with a low-friction composite material. The other side of the slider is also spherical, coated with stainless steel, and sits in a spherical cavity, also coated with the low-friction composite material. As the slider moves over the spherical surface, it causes the supported mass to rise and provides the restoring force for the system.

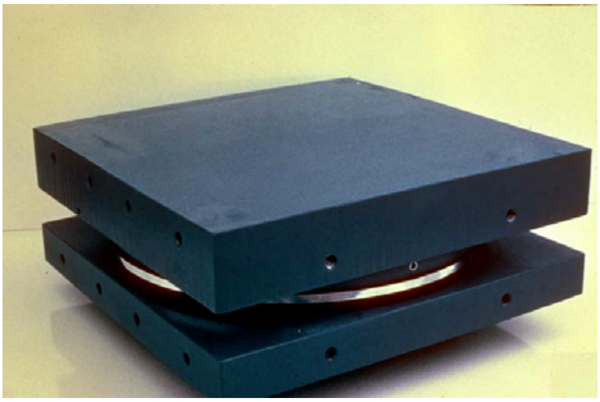

Figure 1.5 Example of friction pendulum bearing.

Sleeved-Pile Isolation System: when is necessary to use deep piles, for example, for buildings on very soft soil, it can be advantageous to use SPIS pile to provide the horizontal flexibility needed for an isolation system. The piles are made flexible by enclosing them in tube with a suitable gap for clearance (Kelly, 2004).

1.3 American Earthquake Regulation for Seismically Isolated Structures

In 1985 in the United States the first buildings to use a seismic isolation system was completed. By many engineers and architects was visited. The Structural Engineers Association of Northern California (SEAONC) created a working group to develop design guidelines for isolated buildings. The Seismology Committee of the Structural Engineers Association of California (SEAOC) is responsible for developing provisions for earthquake-resistant design of structures. These previsions, published for Recommended

Lateral Design Requirements and Commentary (SEAOC, 1985), generally known as the Blue Book, have served as the basis for various editions of the Uniform Building Code (UBC). Published by International Conference of Building Officials (ICBO), it is the most widely used code for earthquake design. In 1986 the SEAONC subcommittee produced a document entitled Tentative Seismic Isolation Design Requirements (SEAONC, 1986) -known as the Yellow Book- as a supplement to the fourth edition of the Blue Book.

The SEAOC Seismology Committee formed a subcommittee in 1988 to produce an isolation design document entitled General Requirements for the Design and Construction of Seismic-Isolated Structures (SEAOC, 1989).

The UCB code differs from the SEAONC guidelines in that it explicitly requires that the design be based on two levels of seismic input. A Design Basis Earthquake (DBE) is defined as the level of earthquake ground shaking that has a 10% probability of being exceeded in a 50-year period. The design provisions for this level of input require that the structure above the isolation system remains essentially elastic. The second level of input is defined as the Maximum Capable Earthquake (MCE), which is the maximum level of earthquake ground shaking that may be expected at the site within the known geological frame-work. This is taken as the earthquake ground motion that has a 10% probability of being exceeded in 100 years. The isolation system should be designed and tested for this level of seismic input and all building separations and utilities that cross the isolation interface should be designed to accommodate the forces and displacements for this level of seismic input.

The 1994 version of the UBC (ICBO, 1994) incorporated many changes. The vertical distribution of force was changed from a uniform one to a triangular one generally used for fixed-base structures. The 1994 code specified an extensive, detailed series of prototype tests that must be carried out prior to construction of the isolators. These tests were not for determining quality control in the manufacturing of the isolators, but were intended to establish the design properties of the isolation system.

Further changes have been made in the 1997 version of the UBC regulations for isolated structures (ICBO, 1997), resulting in a code that both more conservative and more complicated. A large number of new terms have been added. For example, there are now six different displacements that have to be computed. The number of soil profile types has been increased to six, of which there are hard rock, rock and soft rock and there are three soil types.

All isolated projects are currently designed using dynamic analysis, but static analysis is still required to ensure that the design quantities do not fall below certain minimal levels from the static analysis.

The 1997 UCB was replaced in 2000 by the International Building Code (IBC), which has essentially the same provisions for seismically isolated structures, with some changes in notation, but with the same conservatism in calculating design displacements and seismic forces.

In total, the 1997 version of the UBC regulations for seismic-isolated structures turned the simple, straightforward and rational code developed in the 1986 Yellow Book into a complicated and conservative set of requirements that will seriously undermine the use of isolation technology by the general engineering community.

There have been further publications that include code requirements for isolate structures, for example, chapter 9 of FEMA-356 (2000) for the seismic rehabilitation of existing buildings and chapter 13 of FEMA-368 (2001) for new construction but these are essentially identical to the 1997 UBC and the 2000 IBC.

Although seismic technology is a mature technology, only a few projects each year are initiated in the United States; these are generally state, country or city projects, with not one multi-family housing project either completed or in the design stage to date.

Because the governing codes are labyrinthian and unnecessarily conservative, professional engineers perceive that isolation design is complicated when in fact it should simplify the design process and lead to more reliable design.

1.4 Italian Seismic code

In Italy the development and the practical exploitation of the advantages of the technologies for the control of the seismic structural vibrations has been slowed down by the lack of a specific norm. The enforcement of the OPCM n. 3274 of 20.03.2003 and the successive modifications and integrations (OPCM n. 3431 of 03.05.2005), including two chapters on the seismic isolation of buildings and bridges, represented a turning point for their practical use, so that most of the new strategic buildings are now designed with seismic isolation. However there still are several problems to be further studied and better solved, to make applications more and more reliable and easy. The last Italian code is called "Nuove Norme tecniche per le Costruzioni", (Ministerial Decree of 14 January 2008, G.U. n. 29 of 4.02.2008 suppl. ord. n° 30), and moves closer to European code. The Eurocode 8 gets the parts 1 and 2 (CEN-1998-1-1 2003, CEN-1998-1-2 2004) about the buildings (and general structures) and bridges. These specific chapters deal with seismic isolated structures design.

Regarding the calculation, the elastic behaviour of the structure is considered, because the design procedures more reliable are and the design model is close the real behaviour under earthquake.

In the Italian code, as well as in many other codes, the equivalent static analysis is strongly limited due to the difficulty of defining a reasonably conservative distribution of inertia forces along the height of the building, as soon as the behaviour of the isolation system is non linear and/or the damping is high.

The concerned problems are relevant to the four main control techniques (seismic isolation, passive energy dissipation, tuned mass, semi-active control) as applied to structures with usual characteristics (R/C and steel buildings, bridges with R/C piers) or peculiar structures (R/C precast buildings, monumental masonry buildings such as churches and palaces, light structures). Almost all the currently used technologies are considered, both the well established ones (rubber and sliding isolators, viscous, visco-elastic and hysteretic energy dissipating devices) and the most recently proposed (shape memory alloy, magneto-rheological, wire rope devices). The design problems to be dealt with are relevant to both new and existing constructions. For these latter, particular attention should be devoted to monumental buildings, deck bridges and the application of energy dissipating devices to R/C buildings. A specific aspect to be dealt with is the response of structures with seismic isolation or energy dissipation protection systems to near-fault earthquakes, with the aim of studying suitable provisions in the design of the devices or of the structure, as a second line of defence to guarantee adequate safety margin with respect to the total collapse of the structural system (Reluis, 2006)

Glossary

Isolation system—Collection of individual isolator units that transfers force from foundation to superstructure

HDNR isolator—An isolation unit made from natural rubber specially compounded for enhanced energy dissipation

LP isolator—An elastomeric isolation unit where energy dissipation is provided by a centrally located lead plug

FPS isolator—A metallic isolation unit based on pendulum action and sliding friction

Effective stiffness—Aggregate stiffness of all isolation units in system at a specified displacement

List of Symbols

c_b nominal damping constant of the isolation system

c_s nominal damping constant of the structure above the isolation system

k_b nominal stiffness of the isolation system

k_s nominal stiffness of the structure above the isolation system

m_b base mass

m_s superstructure mass

u_s absolute displacement of superstructure mass

u_g absolute ground displacement

v_b base displacement relative to ground

v_s superstructure displacement relative to base mass

β_b nominal damping factor in the isolation system

β_s nominal damping factor in the superstructure system

$\underline{\Phi}^1$ first mode shape

$\underline{\Phi}^2$ second mode shape

ω_b nominal isolation frequency

ω_s nominal fixed-base structure frequency

Chapter II

2. ENERGY DISSIPATION

The objective to adding energy dissipation (damping) hardware to new and existing construction is to dissipate much of the earthquake-induced energy in disposable elements not forming part of the gravity framing system. Key to this philosophy is limiting or eliminating damage to the gravity-load-resisting system.

Supplemental damping hardware is parsed into three categories: hysteretic, velocity-dependent and others. Examples of hysteretic (displacement-dependent) dampers include devices based on friction and yielding of metal. Figure 2.1 presents sample force-displacement loops of hysteretic dampers.

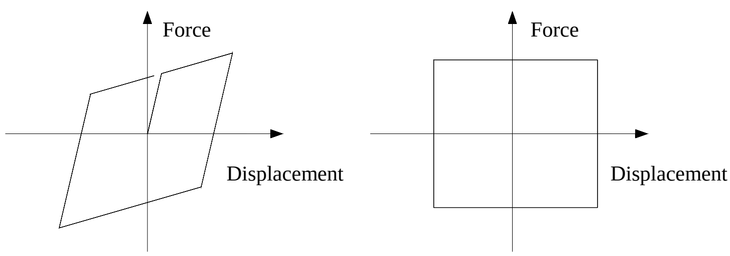

Figure 2.1 Force-displacement relations for hysteretic dampers.

Examples of velocity-dependent systems include dampers consisting of viscoelastic solid materials, dampers operating by deformation of viscoelastic fluids (e.g., viscous shear walls) and dampers operating by forcing fluid through an orifice (e.g., viscous fluid dampers).

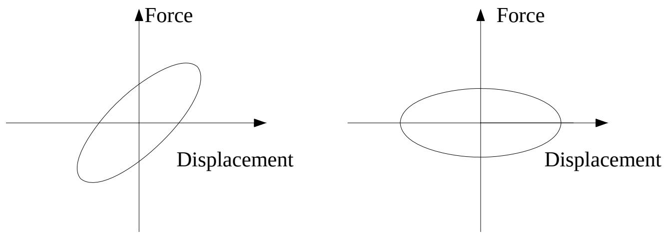

Figure 2.2 Force-displacement relations for velocity-dependent dampers.

Figure 2.2 illustrates the behaviour of these velocity-dependent systems. Other systems have characteristics that cannot be classified by one of the basic types depicted in Figure 2.1 or Figure 2.2. Examples are dampers made of shape memory alloys, frictional-spring assemblies with recentering capabilities and fluid restoring force/damping dampers (Constantinou *et al.*, 1998).

2.1 Hysteretic Dampers

Hysteretic dampers exhibit bilinear or trilinear hysteretic, elasto-plastic (frictional) behaviour, which can be easily captured with structural analysis software currently in the marketplace. An alternative metallic yielding damper, the unbonded steel brace, is shown in Figure 2.3.

This damper was developed in Japan in the mid-1980s (Watanabe *et al.*, 1988) and has been used in a number of projects in California and also found widespread application in Japan.

Figure 2.3 Close-up detail of longer unbonded brace (buckling restrained) connection to steel framing. (University of California, Berkeley).

2.2 Velocity-Dependent Dampers

Solid viscoelastic dampers typically consist of constrained layers of viscoelastic polymers. The effective stiffness and damping coefficient are dependent on the frequency, temperature and amplitude of motion (Soong and Dargush, 1997). The frequency and temperature dependences of viscoelastic polymers generally vary as a function of the composition of the polymer.

Fluid viscoelastic devices, which operate on the principle of deformation (shearing) of viscoelastic fluids, have behaviour that resembles a solid viscoelastic device. Fluid and solid viscoelastic devices are distinguished by the ratio of the loss stiffness to the effective or storage stiffness.

Fluid viscous dampers are widely used in the United States at present. Much of the technology used in this type of damper was developed for military, aerospace and energy applications.

Figure 2.4 is a schematic section through a single-ended fluid viscous damper. Figure 2.5 shows a fluid damper picture. Such dampers are often compact because the fluid drop across the damper piston head generally ranges between 35 and 70 MPa.

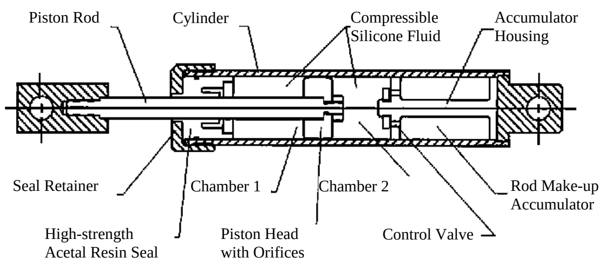

Figure 2.4 Schematic section through a fluid viscous damper.

Figure 2.5 Large damper testing at EERC Laboratories, University of California, Berkeley (Courtesy of Cameron Black, SIE Inc).

2.3 Analysis Procedures for Supplemental Dampers

The lack of analysis methods, guidelines and commentary has been the key impediment to the widespread application of supplemental dampers in buildings and bridges.

FEMA-273, entitled *Guidelines for seismic Rehabilitation of Buildings*, was published in 1997 after more than 5 years of development. FEMA-273 represented a paradigm shift in the practice of earthquake engineering in the United Stated because deformations and not forces were used as the basis for the design of ductile components. Performance and damage were characterized in terms of component deformation capacity of ductile components.

Four methods of seismic analysis were presented in FEMA-273/356 (republished in 2000): linear static procedure (LSP), linear dynamic procedure (LDP), nonlinear static procedure (NSP) and non linear dynamic procedure (NDP).

All four procedures can be used to implement supplemental dampers in buildings although the limitations on the use of the linear procedures likely will limit their widespread use. Of the four, only the NDP can explicitly capture nonlinear deformations and strain -and load- history effects.

The other three procedures are considered to be less precise then the NDP, although given the additional uncertainties associated with non linear analysis, the loss of accuracy might be small (Bozorgnia and Bertero, 2004). The two nonlinear procedures lend themselves to component checking using deformations and displacements; most of the component deformation limits are based on engineering judgment and evaluation of test data.

Linear static procedure (LSP): is substantially different from the elastic lateral force procedures adopted in modern seismic code. A pseudo lateral force, *V*, is applied to a linear elastic model of the building frame such that its maximum displacement is approximately equal to the expected displacement of the yielding building frame. The objective is to estimate displacements in a yielding building using a linear procedure.

Nonlinear static procedure (NSP): is a displacement-based method of analysis. Structural components are modelled using nonlinear force-deformation relations and the stiffness of the supplemental dampers is included in the model. Lateral loads are applied in a predetermined pattern to the model, which is incrementally pushed to a target displacement thereby establishing a force (base shear) versus displacement (roof) relation for the building. Component deformations are calculated at the target displacement.

Linear static procedure: Supplemental Dampers: the LSP can be used only if the framing system exclusive of the dampers remains essentially linearly elastic in the design earthquake after the effects of the added damping are considered. Further, the level of effective damping must not exceed 30% of critical in the fundamental mode. Dampers are modelled using their secant stiffness at the point of maximum displacement. The stiffness of each damper must be included in the mathematical model.

Nonlinear static procedure: Supplemental Dampers: two methods of nonlinear static analysis are provided in FEMA-273/356 for implementing supplemental dampers: Method 1 (known as the coefficient method) and Method 2 (known as the capacity-spectrum method). The two methods are equally precise.

2.4 New Configurations for damping Systems

Small interstory drifts and velocities characterize stiff seismic framing systems and all framing systems for wind excitation. Many have assumed that such systems are not candidates for the addition of dampers because significant drifts and velocities are needed to dissipative substantial energy.

The interstory response of a stiff lateral load-resisting system, such as a reinforced concrete shear wall system or a steel-braced dual system, is generally characterized by both small relative velocities and small relative displacements, so are best structural systems suited for implementation of energy dissipation devices. This observation is correct for conventional damper configurations involving diagonal (in-line) or chevron installations.

Recent work at the University at Buffalo, State University of New York (Constantinou and Sigaher, 2000; Constatninou at al., 2001; Sigaher and Constantinou, 2003) has sought to expand the utility of fluid viscous damping devices to the short-period range and for wind applications through the use of mechanisms that magnify the damper displacement for a given interstory drift. Such magnification permits the use of dampers with smaller force outputs (smaller damper volume), larger strokes and reduced cost. Two configurations are the toggle-brace and the scissor-jack.

To illustrate the effectiveness of the toggle-brace and the scissor-jack assemblies for short period framing systems, consider the six damper configurations presented in Figure 2.6.

Diagonal	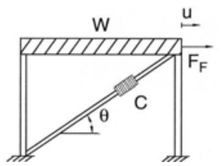	$f=\cos\theta$	$\theta=37°$ $f=0.799$ $\beta=0.032$
Chevron	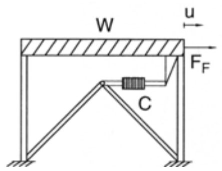	$f=1.00$	$f=1.00$ $\beta=0.05$
Lower Toggle	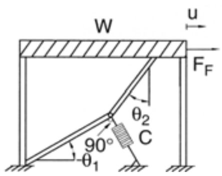	$f=\dfrac{\sin\theta_2}{\cos(\theta_1+\theta_2)}$	$\theta_1=31.9°,\theta_2=43.2°$ $f=2.662$ $\beta=0.344$
Upper Toggle	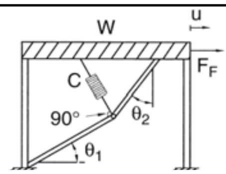	$f=\dfrac{\sin\theta_2}{\cos(\theta_1+\theta_2)}+\sin\theta_1$	$\theta_1=31.9°,\theta_2=43.2°$ $f=3.191$ $\beta=0.509$
Reverse Toggle	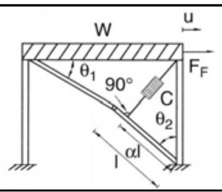	$f=\dfrac{\sin\theta_2}{\cos(\theta_1+\theta_2)}-\cos\theta_2$	$\theta_1=30°,\theta_2=49°,\alpha=0.7$ $f=2.521$ $\beta=0.318$
Scissor-Jack	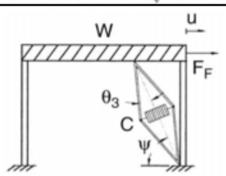	$f=\dfrac{\cos\psi}{\tan\theta_3}$	$\theta_3=9°,\psi=70°$ $f=2.159$ $\beta=0.233$

Figure 2.6 Effectiveness of damper configurations (Sigaher and Constantinou, 2003).

Glossary

Damper—Device added to a building frame to mitigate response due to earthquake shaking

Displacement-dependent damper—Hysteretic damper

Energy dissipation device—Damper

Hysteretic damper—A damper that dissipates energy through yielding of metal or friction where energy dissipation is not a function of the rate of loading

Scissor jack assembly—Assembly that amplifies the motion of a damping device

Toggle-brace assembly—Assembly that amplifies the motion of a damping device

Velocity-dependent damper— A damper that dissipates energy through shearing of solid or fluid viscoelastic materials or by forcing fluid through or past a piston head

List of Symbols

f	displacement magnification factors in damper
β	damping ratio of the single-short frame nominal damping constant of the structure above the isolation system
θ_3	angle of damper axis with respect to the 90° line

Chapter III

3. SEISMIC ISOLATION OF A WORSHIP STRUCTURE

The “Santuario della Madonna delle Lacrime” (Figure 3.1) represents an imposing reinforced/prestressed concrete structure (IIC, 2001; IIC, 2006), which was built in Siracusa (Italy) at the centre of a green park not far from the spot where – from 29th August until 1st September 1953 – a small picture representing Our Lady wept human tears.

Figure 3.1 Bird’s flight view of the Sanctuary.

The building was designed by the illustrious Prof. Riccardo Morandi, who passed away in 1989 after his last visit to the site of the building Sanctuary.

The underground portion of the building, consisting of the foundations and the Crypt, was built during the years from 1966 to 1968, while the construction of the Upper Temple began at the end of the 80's. The latter, able to contain approximately 11.0000 persons on a clear area of approximately 4000 m^2, was inaugurated in 1994 by the Pope John Paul II.

3.1 Description of the Sanctuary before the seismic retrofit

The Upper Temple is characterized by an imposing truncated-conical dome made up of 22 sub-vertical ribs, each having two straight parts with different slope and a V cross-section with arms of variable length along the height, arranged according a radial symmetry with respect to the central vertical axis. The external surface of all the structure's reinforced concrete elements is of fair-face without any covering, except a silicon transparent waterproofing paint. Assuming equal to 0.00 m the elevation of the extrados of the Crypt's covering plane, the r.c. structure of the dome rises from the elevation 4.00 m, at the top of the 22 vertical supporting piers rising from the foundations of the Crypt, up to elevation 74.30 m on the top of the dome (Figure 3.2). The 22 ribs are connected each other horizontally by eight circular rings having a decreasing diameter along the height.

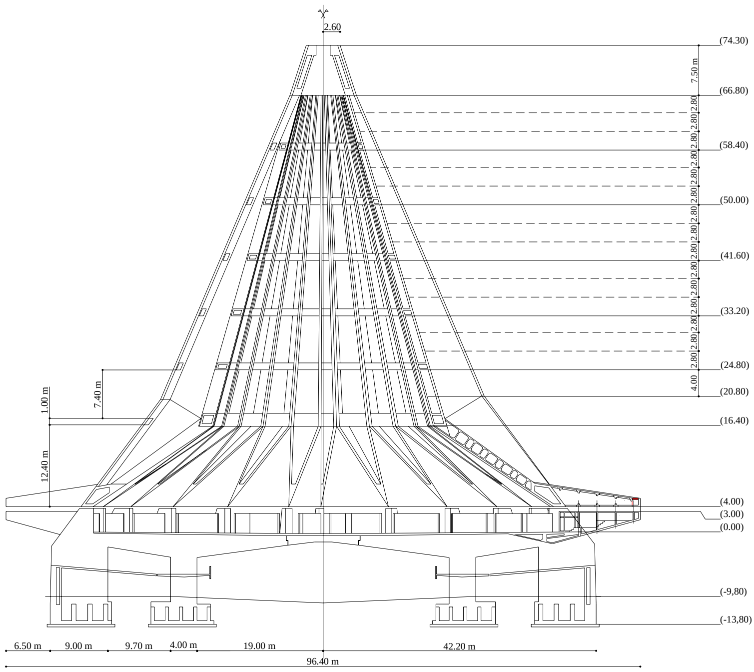

Figure 3.2 Vertical cross-section of the Sanctuary.

The assembly of the highest parts of the 22 rib forms a truncated cone, hollow in top, which contains a 20 m high stainless steel crown, supporting a central stele with a bronze statue of Our Lady on the top.

From the lowest ring (base of the conical surfaces), 19 sub-horizontal external cantilevers depart, each of 17.00 m in span, which represent the covering of as many chapels, whose floor is suspended to each cantilevered box-section member by means of 8 steel tendons. The prestressed concrete connection ring at the base of the conical surfaces has special dimensions because, besides to absorb all the horizontal thrusts acting on it, also counteracts the torsional moments induced by the cantilevered chapels. Each of the

22 ribs consists in two r.c. slabs with a constant 20 cm thickness, which converge in the apex of the V shape.

Up to elevation 16.40 m, the plane zone bounded by the ribs is constituted by a big properly lightened sub-horizontal r.c. slab of variable thickness. Towards outside, the apexes of two adjacent Vs are separated by a 50.00 m high window structure, horizontally interrupted by the presence of the r.c. connection ribs. As said at the beginning of the description, the base ring is supported at elevation 4.00 m on 22 r.c. piers (one for each of the 22 dome ribs) with trapezoidal shape (variable thickness from 0.80 m at the bottom to 1.00 m at the top), placed along the perimetrical circle at 10.00 m spacing, and 3.74 m high starting from the elevation 0.00 m of the Crypt's covering extrados. Between each column and the base ring above, a pot bearing with a steel-teflon sliding surface and 1000 t capacity was installed. Each bearing allowed the geometrical variations of the diameter of the covering's base due to thermal and tensional variations inside the ring, while the displacements in tangential direction were prevented.

3.2 The seismic isolation of the Sanctuary of Siracusa

According to the Italian seismic code in force at the time of construction of the building (Law N. 64 of 02.02.1974 and following Ministerial Decree of 03.03.1975 and 24.01.1986), the verification of the structure was made by using the allowable stress method. The stresses induced by permanent and accidental loads, wind, seismic actions, thermal variations, shrinkage and viscosity deformations were considered.

With the new seismic code and the following modifications and integrations (OPCM n. 3274 of 20.03.2003, OPCM n. 3431 of 03.05.2005), the intensity of the seismic design actions, relative to the seismic zone including Siracusa, substantially increased, even if the classification of this zone was not modified. The particular shape of the structure of the Sanctuary allows significant overstrength margins for all the vertical elements above the piers supporting the base ring, but a violent earthquake could have caused structural damages concentrated in the columns and in the bearings, and therefore compromise the equilibrium of the upper structure. This knowledge, joined to the need to substitute the 22 original bearings of the dome due to their inadequate behaviour (leakage of rubber from the pot bearings), made necessary an intervention of seismic isolation of the dome from the lower structure, that was carried out in the period February-March 2006. The pre-existent bearings were substituted by new sliding seismic isolators, manufactured by FIP Industriale (Padova, Italy) and widely employed for the isolation of bridge decks from the supporting piers. The new antiseismic devices are unidirectional bearings including elasto-plastic dissipators with “moon’s sickle” shape (Figure 3.3), able to transmit the horizontal seismic action on the dome to the columns through their elasto-plastic movement.

Figure 3.3 New antiseismic bearing opened.

The isolators support a nominal vertical load equal to 11000 kN and a maximum vertical load of 14000 kN; allow rotations up to 0.01 rad, radial displacements (due to thermal variations) up to ± 200 mm, and tangential displacements up to ± 150 mm; develop a horizontal load of 1050 kN at the maximum tangential displacement, and a vertical displacement smaller than 1 mm under the nominal vertical load. Therefore, in case of a seismic event whose intensity involves an inelastic behaviour of the structure, the plasticization is concentrated in the special “moon’s sickle” steel elements of the new seismic isolators, which dissipate energy in a hysteretic mechanism. This prevents damaging of the columns because reduces the forces transmitted to them, which represent the most vulnerable elements of the construction. Besides, in case of a moderate earthquake either the church or the new devices should not be damaged, so keeping the total functionality of the construction.

The substitution of the old bearings of the Sanctuary’s dome was a rather complex intervention: the complete raising of the whole dome was preceded by a first preliminary unloading test performed on only one of the pre-existent bearings by the use of 2 identical hydraulic jacks installed towards the exterior of the Sanctuary, and afterwards a second preliminary unloading test of the 22 bearings supporting the dome, simultaneously, by means of the operation of 44 identical hydraulic jacks (2 for each column). After the suspension of both the preliminary tests, due to the advanced cracking pattern observed in the area close to the upper plate of the jacks and caused by the high torsional moments induced by the jacks on the annular beam, it was decided to carry out the substitution intervention (Serino *et al.*, 2007b) by simultaneously raising (Figure 3.4) the 22 supporting points of the whole dome (whose total mass is approximately 22.000 t) through 114 jacks (5 for each pier – 2 of them corresponding to those of the preliminary tests plus further 3 jacks installed towards the interior of the Sanctuary) operated simultaneously by an electronic control system (Figure 3.6), then substituting the pre-existent bearings with the new seismic isolators (Figure 3.7), and finally lowering the whole dome through the unloading of all the jacks (Figure 3.5).

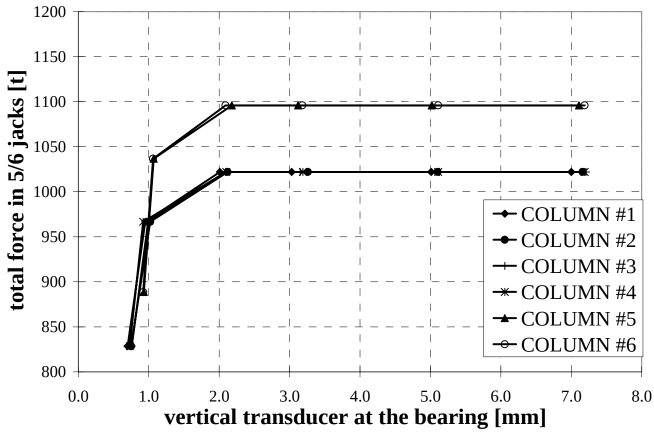

Figure 3.4 Force – displacement diagrams relative to one of the four hydraulic systems: complete raising of the dome

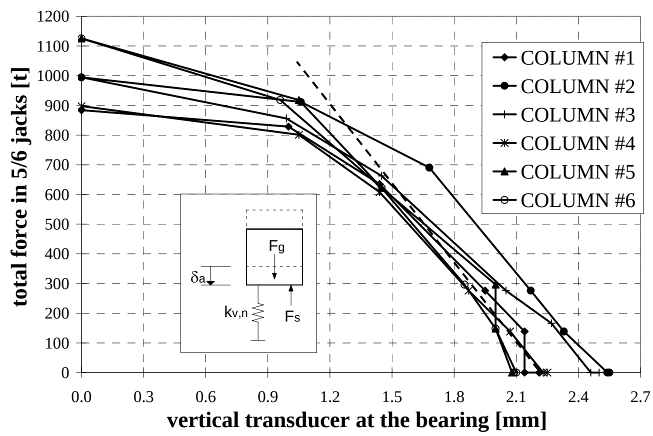

Figure 3.5 Lowering phase of the dome: force – displacement curves relative to one of the hydraulic systems

Figure 3.6 Hydraulic control systems of the jacks.

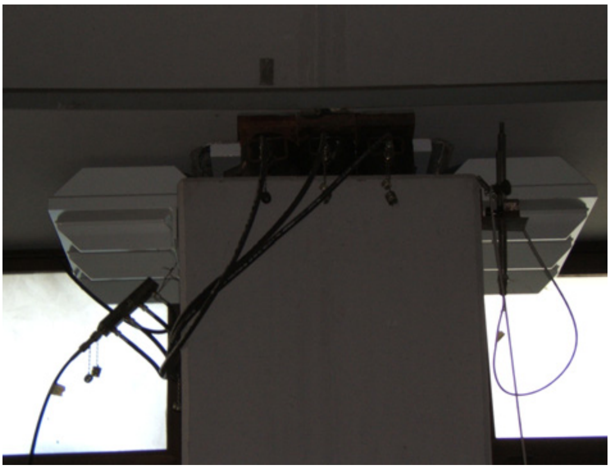

Figure 3.7 New antiseismic bearing installed.

The decision to perform a rigid raising and lowering of the whole covering by simultaneously acting on all the jacks, was taken in order to avoid the overloading of the adjacent bearings occurring when only one bearing was unloaded and to avoid excessive stresses in the r.c. annular beam and in the ribs above due to dangerous differential displacements. Moreover, the vertical stiffness of the pre-existent bearings, as well as that one of the new antiseismic bearings, have been easily deduced by the experimental curves relative to the raising and lowering phases of the dome (Serino *et al.*, 2006).

3.3 Analytical modeling of the antiseismic devices

The elastic behaviour of a “moon’s sickle” element up to the achievement of the steel yield stress in the most stressed point it was analytically examined, in order to compute the elastic stiffness: for the steel element of Figure 3.8, characterized by a constant transversal thickness b and an height $h(s)$ variable along the barycentric line, and loaded by two equal and opposite forces applied in the anchor joints, the relative displacement along the straight line connecting the joints has been evaluated as sum of the contributions due to bending moment, axial and shear forces (Serino *et al.*, 2007a).

Figure 3.8 contains the geometry of the dissipative steel element with respect to the reference system (O,X,Y): it is defined by a semicircle with centre $O \equiv C_1$ and radius R_i, and by the semicircular outline with radius R_e and centre C_2. The latter is located on the Y axis at a distance Δ from the centre O in the positive direction. The system of forces $\pm F$ is applied at the ends of the chord l lying on the straight line connecting the centres of the anchor joints, parallel to the X axis at a distance a in the –Y direction.

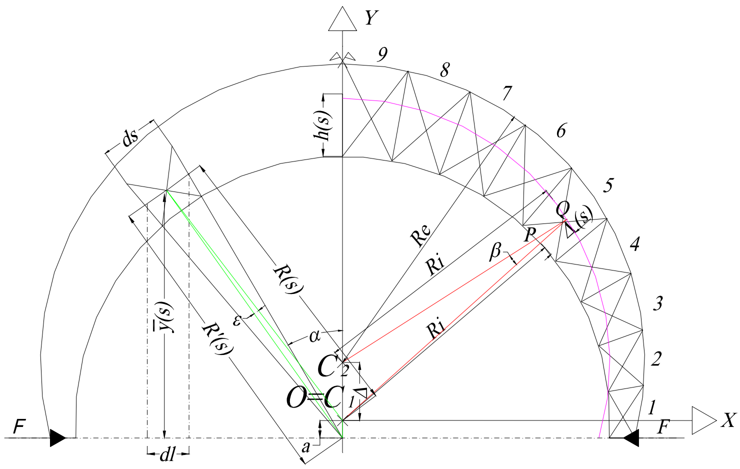

Figure 3.8 Reference scheme in the analytical study.

The generic cross-section *S*, sloping of α with respect to the vertical Y axis and having abscissa *s* along the semicircle, is loaded by normal force $N(s) = -F \cdot \cos\alpha(s)$, shearing force $T(s) = F \cdot sen\alpha(s)$ and bending moment $M(s) = -F \cdot \bar{y}(s)$, where $\bar{y}(s)$ is the distance of the centroid of the cross-section *S* from the line of action of the forces.

The normal force $N(s)$ gives rise to a shortening of the length *ds* of the generic arch portion, whose orthogonal projection on the X axis has the value $\delta(dl)^N = \delta(ds)^N \cos\alpha(s)$ so $\delta(dl)^N = -\left[F \cdot \cos^2\alpha(s)\right] / \left[E \cdot b \cdot h(s)\right] \cdot ds$ where *E* is the Young's modulus of steel and $A(s) = b \cdot h(s)$ the area of the cross-section. By integrating the expression of $\delta(dl)^N$ on the whole “moon's sickle” element (i.e. by varying $\alpha(s)$ from –90° to +90°, without considering the edge effects at the connections), the total change of length of the chord *l* due to $N(s)$ can be obtained as below:

$$\Delta l^N = \int_S \delta(dl)^N = -\frac{F}{E \cdot b} \int_S \frac{\cos^2 \alpha(s)}{h(s)} ds \qquad (3.3.1)$$

The bending moment *M(s)* causes a relative rotation between the end cross-sections of the generic arch portion *ds* and a corresponding shortening of its length, whose orthogonal projection on the X axis assumes the value $\delta(dl)^M = \delta\varphi \cdot \bar{y}(s) = -\left[12 \cdot F \cdot \bar{y}^2(s)\right] / E \cdot b \cdot h^3(s) \cdot ds$, where $b \cdot h^3(s)/12 = I(s)$ represents the moment of inertia with respect to the centroidal axis, that is orthogonal to the XY plane. The total change of length of the chord *l* due to *M(s)* can be deduced by integration:

$$\Delta l^M = \int_S \delta(dl)^M = -\frac{12F}{Eb} \int_S \frac{\bar{y}^2(s)}{h^3(s)} ds \qquad (3.3.2)$$

The shear force *T(s)* causes a relative sliding between the end faces of the generic arch portion *ds* and hence a relative transversal displacement between its end cross-sections, whose orthogonal projection on the X axis has the value $\delta(dl)^T = -\delta s_T \cdot sen\alpha(s) = -\chi \cdot \left[F \cdot sen^2\alpha(s)\right] / \left[G \cdot b \cdot h(s)\right] \cdot ds$, with χ shape factor of the cross-section ($6/5$ for a rectangle) and *G* shear modulus of steel. The total change of length of the chord *l* due to *T(s)* can be computed by integrating the expression of $\delta(dl)^T$ on the whole “moon’s sickle” element as:

$$\Delta l^T = \int_S \delta(dl)^T = -\chi \frac{F}{G \cdot b} \int_S \frac{sen^2\alpha(s)}{h(s)} ds \qquad (3.3.3)$$

The total shortening of the chord *l* is the sum of all the contributions above, that is $\Delta l = \Delta l^N + \Delta l^M + \Delta l^T$. It is worth to point out that the expression of the height $h(s) = R_e - R_i + \Delta(s) = \Delta R + \Delta(s)$, that is present in the above formula and is variable with the cross-section *S*, can be derived through simple geometrical considerations: it depends on the distance $\Delta(s) = \overline{PQ} = R_i \cdot \cos\beta(s) + \Delta \cdot \cos\alpha(s) - R_i$ between the point P, belonging to the semicircle of centre O and radius R_i, and the point Q, representing the intersection of the straight line OP with the semicircle of centre C_2 and radius R_i. Being the quantity Δ very small with respect to the inner radius R_i, the angle $\beta(s) = \mathrm{C_2QC_1} = arcsen\left[\Delta \cdot sen\alpha\left(s\right)/R_i\right]$ can be assumed close to zero, and $\Delta(s)$ reduces to the simple product $\Delta\cos\alpha(s)$. The applied forces $\pm F_y$ corresponding to the achievement of the steel yield stress in the key cross-section are obtained as $f_y = N/A + M/W = -F_y/(b \cdot h) - \left(6 \cdot F_y \cdot \bar{y}\right)/\left(b \cdot h^2\right)$ so $\pm F_y = \pm\left(f_y \cdot b \cdot h\right)/\left(1 + 6 \cdot \bar{y}/h\right)$, where *h* and $\bar{y}$ are relative to α=0. In the case of the steel used to manufacture the “moon’s sickle” elasto-plastic dissipators ($f_y = 355\,\mathrm{N \cdot mm^{-2}}$) the system of forces inducing the yielding of the key cross-section is $\pm F_y = \pm\,24761\,\mathrm{N}$, and the total shortening $\Delta l = -5.60\mathrm{mm}$ of the chord l is the sum of the contributions of all the arch portions, which the "moon's sickle" element is divided (their length ds corresponding to an angle $\Delta\alpha$=10°). Table 3.1 and Table 3.2 report the stress plasticization values for each arch portion referring to half semicircle and the calculation of Δl respectively. It is worth to notice that the contribution of the bending moment (Eq. 3.3.2) is of course greater than those of the normal and shearing forces (Eqs. 3.3.1 and 3.3.3, respectively). The elastic stiffness of the elasto-plastic dissipators is then equal to the value $K = F_y / \Delta l = 4422\,\mathrm{N \cdot mm^{-1}}$ and approximately corresponding to the one experimentally observed (Figure 3.9).

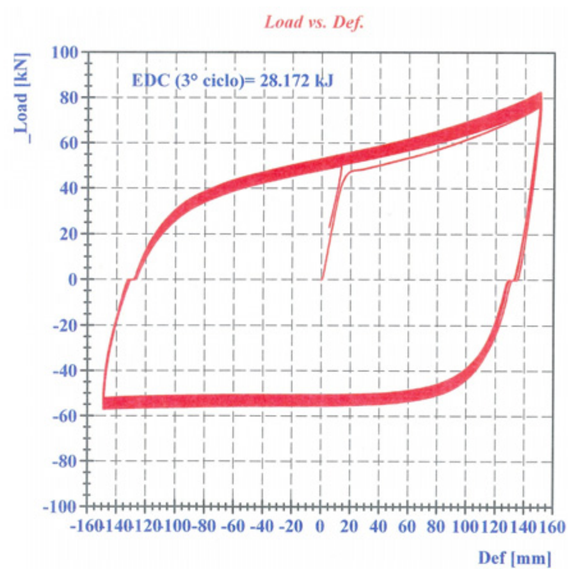

Figure 3.9 Load–deformation cycles relative to a single elasto-plastic dissipator.

Table 3.1 Calculation of Δl.

LENGTH VARIATION OF THE CHORD l												
	$a(s)$	$a(s)$	$\Delta(s)$	h(s)	R(s)	y(s)	Δs	Δl^N	Δl^M	Δl^T	Δl	$2\Delta l$
	[°]	[rad]	[mm]	[mm]	[mm]	[mm]	[mm]	[mm]	[mm]	[mm]	[mm]	[mm]
cross section 1	85	1.4835E+00	3.49	26.49	195.24	17.08	34.08	-4.61E-05	-3.03E-02	-1.94E-02		
cross section 2	75	1.3090E+00	10.35	33.35	198.68	52.14	34.68	-3.28E-04	-1.44E-01	-1.47E-02		
cross section 3	65	1.1345E+00	16.90	39.90	201.95	87.37	35.25	-7.44E-04	-2.40E-01	-1.10E-02		
cross section 4	55	9.5993E-01	22.94	45.94	204.97	121.38	35.77	-2.10E-03	-3.08E-01	-7.92E-03		
cross section 5	45	7.8540E-01	28.28	51.28	207.64	152.70	36.24	-1.67E-03	-3.55E-01	-5.36E-03		
cross section 6	35	6.1087E-01	32.77	55.77	209.88	179.89	36.63	-2.08E-03	-3.87E-01	-3.28E-03		
cross section 7	25	4.3633E-01	36.25	59.25	211.63	201.60	36.94	-2.41E-03	-4.08E-01	-1.69E-03		
cross section 8	15	2.6180E-01	38.64	61.64	212.82	216.74	37.14	-2.65E-03	-4.22E-01	-6.12E-04		
cross section 9	5	8.7266E-02	39.85	62.85	213.42	224.52	37.25	-2.77E-03	-4.28E-01	-6.83E-05		
key section	0	0.0000E+00	40.00	63.00	213.50	225.50	37.26					
								-1.48E-02	-2.72E+00	-6.40E-02	-2.80 E+00	-5.60 E+00

Table 3.2 Stress plasticization values.

STRESS VALUES													
	$a(s)$	$a(s)$	y(s)	N	T	M	h(s)	A	I	W	$\sigma_{\inf}$	$\sigma_{\sup}$	$\tau_{\max}$	σ_{eqG}
	[°]	[rad]	[mm]	[N]	[N]	[N*mm]	[mm]	[mm^2]	[mm^4]	[mm^3]	[N/mm^2]	[N/mm2]	[N/mm^2]	[N/mm^2]
cross section 1	85	1.4835299	17.075786	-2158.11	24667.36	-422823.45	26.49	662.16	38709.64	2923.00	147.91	-141.39	-4.89	9.07
cross section 2	75	1.3089969	52.137492	-6408.77	23917.85	-1291006.71	33.35	833.82	77295.49	4635.03	286.22	-270.85	-11.53	21.40
cross section 3	65	1.134464	87.368181	-10464.70	22441.61	-2163374.28	39.90	997.62	132382.91	6634.95	336.55	-315.57	-15.73	29.20
cross section 4	55	0.9599311	121.37945	-14202.66	20283.50	-3005546.95	45.94	1148.58	202031.20	8794.85	354.10	-329.37	-18.55	34.42
cross section 5	45	0.7853982	152.70252	-17509.08	17509.08	-3781155.69	51.28	1282.11	281003.24	10958.65	358.69	-331.38	-20.48	38.02
cross section 6	35	0.6108652	179.88577	-20283.50	14202.66	-4454256.00	55.77	1394.15	361300.99	12957.73	358.30	-329.20	-21.82	40.50
cross section 7	25	0.4363323	201.60008	-22441.61	10464.70	-4991936.62	59.25	1481.31	433385.78	14628.49	356.40	-326.10	-22.72	42.18
cross section 8	15	0.2617994	216.74116	-23917.85	6408.77	-5366853.79	61.64	1540.93	487847.34	15829.68	354.56	-323.52	-23.28	43.21
cross section 9	5	0.0872665	224.51805	-24667.36	2158.11	-5559421.71	62.85	1571.19	517164.55	16457.69	353.50	-322.10	-23.55	43.71
key section	0	0	225.5	-24761.58	0	-5583736.47	63.00	1575.00	520931.25	16537.50	353.36	-321.92	-23.58	43.77

3.4 Numerical model of the worship structure

The isolation system of the Sanctuary's dome was designed according to the Italian seismic code delivered in March 2003 (OPCM n. 3274 of 20.03.2003), therefore the verifications of damage limit state (DLS) and of ultimate limit state (ULS) were checked. In the enclosure to the code, Siracusa is classified as II category seismic zone, so a peak ground acceleration at ULS equal to *0.25g* (rigid soil) was considered. But, the same code allows, for more accurate determinations, deviations not larger than 20% with respect to the value assigned to the category. On the other hand, the National Institute of Geophysics and Volcanology (INGV) provided a map of seismic risk values (expressed in terms of maximum acceleration of the ground with excess probability of 10% in 50 years related to rigid soils, and computed for two points grids with spacing of 0.05° and 0.02°) and, therefore, assigned at the grid's point closest to Siracusa a seismic risk value equal to approximately *0.20g*, which is just that one obtained by reducing of 20% the value defined by the seismic classification. The designers of the isolation system assumed the value *0.20g* as maximum horizontal acceleration of the ground, and determined the elastic response spectrum, describing the seismic action to be considered according to the Italian seismic code (OPCM n.3274), by considering a ground acceleration $a_g = 0.200\,g = 1.962\,\mathrm{m}\cdot\mathrm{s}^{-2}$, a lithoid foundation soil (ground type $A \rightarrow S = 1$, $T_B = 0.15$ *s*, $T_C = 0.40$ *s*, $T_D = 2.5$ *s*), a maximum spectral amplification factor equal to 2.5, and a conservative equivalent viscous damping coefficient (5%). The numerical investigation has been carried out by applying the new Italian seismic code delivered on 4 February 2008 (Ministerial Decree of 14 January 2008). The elastic response spectrum provided by the new code is different from that one previously described (Figure 3.10), because it is characterized by the following parameters defining the seismic action: maximum horizontal ground acceleration $a_g = 0.211g = 2.070\,\mathrm{m \cdot s^{-2}}$ with excess probability of 10% in 50 years with a return period of 475 years, rigid foundation soil (ground type $A \rightarrow S = 1$, $T_B = 0.14$ s, $T_C = 0.42$ s, $T_D = 1.7$ s), maximum spectral amplification factor equal to 2.272, and equivalent viscous damping coefficient of 5%.

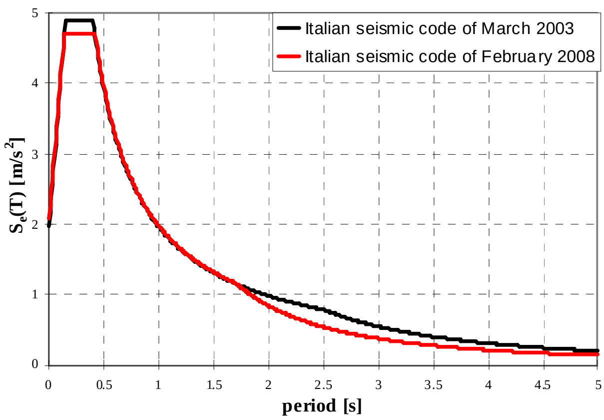

Figure 3.10 Elastic response spectra.

The effectiveness of the seismic retrofit intervention is shown by comparing the response of the isolated structure to the earthquake excitation compatible with the latter elastic response spectrum, and the correspondent results of the numerical analyses on the construction before the isolation intervention.

A Finite Element Structural Analysis Program has been used to design a simplified numerical model of the structure, able to simulate its real behaviour (Serino *et al.*, 2008b). The dome of the Sanctuary has been assumed as a rigid body supported on 22 r.c. piers uniformly distributed along the circular perimeter of the Upper Temple's plan: the columns are defined by 44 nodes and 22 beam elements with variable cross-section and fixed at the base, while the rigid body is simulated by a constraint connecting the 22 nodes placed at the elevation of the prestressed concrete base ring where the upper plates of the bearings are located, with a master node set at the elevation of the dome's centroid (evaluated approximately at 19.20 m) and characterized by a translational mass along each of the three directions equal to the whole mass of the dome, corresponding to the total force of 227800 kN exerted by the 114 jacks during the raising phase of the covering. The rigid body is connected to the beam elements representing the columns through 22 elements simulating the new antiseismic bearings. They are characterized by the following link properties: *i)* in vertical direction, an elastic stiffness equal to the experimentally measured vertical stiffness $k_{v,n} = 9000\,\mathrm{kN \cdot mm^{-1}}$ of the bearings; *ii)* in radial direction, a friction link defined through a friction coefficient of 1%, equal to the experimental value determined for the sliding of a steel surface on a lubricated teflon surface; *iii)* in tangential direction, an elasto-plastic Wen-type law, whose parameters have been deduced by experimental tests, considering that in each antiseismic device there are 16 steel dissipators of “moon’s sickle” shape which work in parallel. The plasticization force F_p=640 kN has been obtained by multiplying by 16 the value obtained by experimental cycles (F_p=40 kN × 16 = 640 kN), the elastic stiffness k_e= 69600 kN·m^{-1} is equal to 16 times the corresponding stiffness derived from experimental tests k_e=4350 kN·m^{-1} × 16 = 69600 kN·m^{-1}), the post-elastic stiffness k_{pe}=1778 kN·m^{-1} has been computed by multiplying by 16 the mean experimental value in the approaching and withdrawing phases of the ends of the “moon’s sickle” (k_{pe} = 110 kN·m^{-1} × 16 = 1778 kN·m^{-1}), the displacement of first yield read on the experimental cycle being equal to 15 mm. The model of the Sanctuary before the structural intervention of seismic isolation has been simply derived, by locking in tangential direction the 22 elements representing the bearings, in order to simulate the behaviour of the covering’s pre-existent bearings.

3.5 Analytical model: matrix analysis

The circumference can be subdivided in 22 parts and is possible to define the angle $\alpha = \frac{360}{22} = 16.363636°$ to define the position of the bearings. In Figure 3.11 are shown the radial and tangential directions for an isolator with respect to the global coordinates designates 1 and 2. From some geometric consideration we know that (Figure 3.12):

$$\sin\alpha = b \tag{3.5.1}$$

$$\cos\alpha = a \tag{3.5.2}$$

and

$$F_T = K_T \cdot a \tag{3.5.3}$$

$$F_R = K_R \cdot (-b) \tag{3.5.4}$$

(negative sign is due to the fact that radial force is applied positive whereas the displacement is negative).

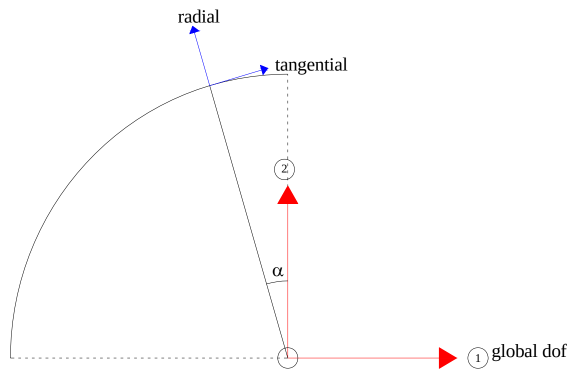

Figure 3.11 Global coordinates.

By considering the dome as a rigid body having two degrees-of-freedom (along 1 and 2 in the global directions), the stiffness coefficients for each isolator are derived, in the global degrees-of freedom.

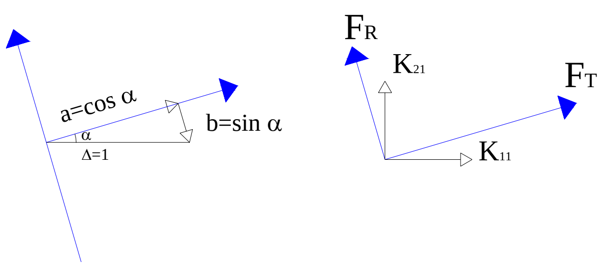

Figure 3.12 Coordinates of the displacements and forces.

By giving unit displacement in the 1st degree-of-freedom, we get $k_{11} = F_T \cdot \cos\alpha - F_R \cdot \sin\alpha$ so:

$$k_{11} = k_T \cos^2\alpha + k_R \sin^2\alpha \tag{3.5.5}$$

and $k_{21} = F_T \sin\alpha + F_R \cos\alpha = k_T \sin\alpha\cos\alpha - k_R \sin\alpha\cos\alpha$ so:

$$k_{21} = \left(k_T - k_R\right)\sin\alpha\cos\alpha \tag{3.5.6}$$

where k_T and k_R are tangential and radial stiffness values of isolators, takes as 69600 kN/m and 1000000 kN/m respectively. Similarly, by giving unit displacement in 2nd degree-of-freedom, we get:

$$k_{22} = \left(k_T a\right)\sin\alpha + \left(k_R b\right)\cos\alpha = k_T \sin^2\alpha + k_R \cos^2\alpha \tag{3.5.7}$$

$$k_{12} = \left(k_T - k_R\right)\sin\alpha\cos\alpha \tag{3.5.8}$$

$$\left[K\right] = \begin{bmatrix} k_{11} & k_{12} \\ k_{21} & k_{22} \end{bmatrix} \tag{3.5.9}$$

Also k_{11} and k_{22} shall be identical since the isolators are placed symmetric about both the axes. The stiffness coefficients for all the isolators are obtained by summing up the values respectively given in Eqs. 3.5.5 and 3.5.6 for appropriate values of α. The stiffness matrix thus formed is symmetrical with the off-diagonal elements tend to zero. Thus the total stiffness matrix becomes as $K = \begin{bmatrix} 11765600 & \cong 0 \\ \cong 0 & 11765600 \end{bmatrix} \frac{kN}{m}$. The horizontal time period of the rigid body can be computed considering the matrix of the masses $M = \begin{bmatrix} 22000 & 0 \\ 0 & 22000 \end{bmatrix} ton$ as:

$$[A] = \left| K - \omega^2 m \right| = 0 \qquad (3.5.10)$$

In other words $\omega^4 - 1069.6\omega^2 + 564.8^2 = 0$ so $\omega = \pm\sqrt{564.8} = 23.76\dfrac{rad}{\sec}$. The horizontal time period will be $T = \dfrac{2\pi}{\omega} = 0.2715$ *sec*. The vertical stiffness of the isolator K_v is taken as 9.6*kN/m* (from the unloading test) and the time period in vertical direction is calculated as $\omega = \sqrt{\dfrac{198 \cdot 10^6}{22000}} = 94,86\dfrac{rad}{\sec}$ so $T = \dfrac{2\pi}{\omega} = 0.066$ *sec*. Table 3.3 shows the calculation. The time periods of rigid body model constructed with SAP 2000 are 0.40 s and 0.087s in the horizontal and vertical directions respectively. The difference is due to the fact that the analytical model is rigid instead the SAP model is flexible due to its connectivity between the finite element members. Figure 3.13 shows the finite element model used for SAP analysis.

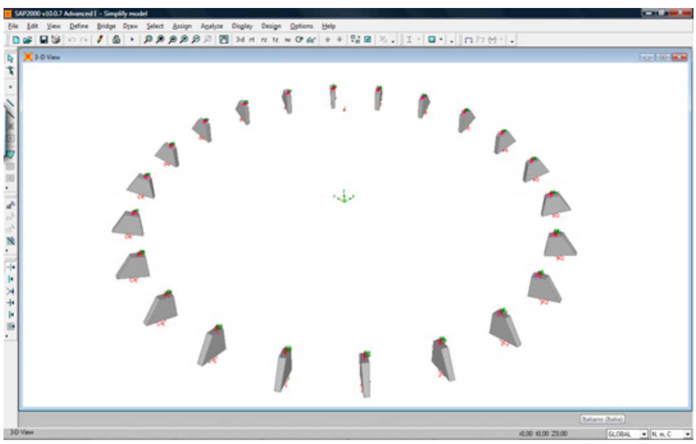

Figure 3.13 Finite element simplify model.

Table 3.3 Analytical calculation.

COLUMN	SQUARE	$\alpha(s)[°]$	$\alpha(s)[rad]$	$a = \sin\alpha$	$b = \cos\alpha$	radial force =b*x_1	tangential force =a*x_2	k_{22}	k_{12}
						[kN]	[kN]	[kN/m]	[kN/m]
1	I SQUARE	16.36	0.29	0.28	0.96	959492.97	19608.59	926151.14	-251506.11
2		32.73	0.57	0.54	0.84	841253.53	37628.60	728051.06	-423160.80
3		49.09	0.86	0.76	0.65	654860.73	52600.17	468595.14	-460464.93
4		65.45	1.14	0.91	0.42	415415.01	63310.39	230158.79	-351574.70
5		81.82	1.43	0.99	0.14	142314.84	68891.57	88443.87	-131061.99
6	II SQUARE	98.18	1.71	0.99	-0.14	-142314.84	68891.57	88443.87	131061.99
7		114.55	2.00	0.91	-0.42	-415415.01	63310.39	230158.79	351574.70
8		130.91	2.28	0.76	-0.65	-654860.73	52600.17	468595.14	460464.93
9		147.27	2.57	0.54	-0.84	-841253.53	37628.60	728051.06	423160.80
10		163.64	2.86	0.28	-0.96	-959492.97	19608.59	926151.14	251506.11
11		180.00	3.14	0.00	-1.00	-1000000.00	0.00	1000000.00	0.00
12	III SQUARE	196.36	3.43	-0.28	-0.96	-959492.97	-19608.59	926151.14	-251506.11
13		212.73	3.71	-0.54	-0.84	-841253.53	-37628.60	728051.06	-423160.80
14		229.09	4.00	-0.76	-0.65	-654860.73	-52600.17	468595.14	-460464.93
15		245.45	4.28	-0.91	-0.42	-415415.01	-63310.39	230158.79	-351574.70
16		261.82	4.57	-0.99	-0.14	-142314.84	-68891.57	88443.87	-131061.99
17	IV SQUARE	278.18	4.86	-0.99	0.14	142314.84	-68891.57	88443.87	131061.99
18		294.55	5.14	-0.91	0.42	415415.01	-63310.39	230158.79	351574.70
19		310.91	5.43	-0.76	0.65	654860.73	-52600.17	468595.14	460464.93
20		327.27	5.71	-0.54	0.84	841253.53	-37628.60	728051.06	423160.80
21		343.64	6.00	-0.28	0.96	959492.97	-19608.59	926151.14	251506.11
22		360.00	6.28	0.00	1.00	1000000.00	0.00	1000000.00	0.00
								11765600	**-1.7948E-10**

3.6 Complete numerical model

The dome is subdivided in 9 Rings placed at variable height connected their self by 22 sub-vertical elements not aligned with the axes of the columns (Figure 3.14).

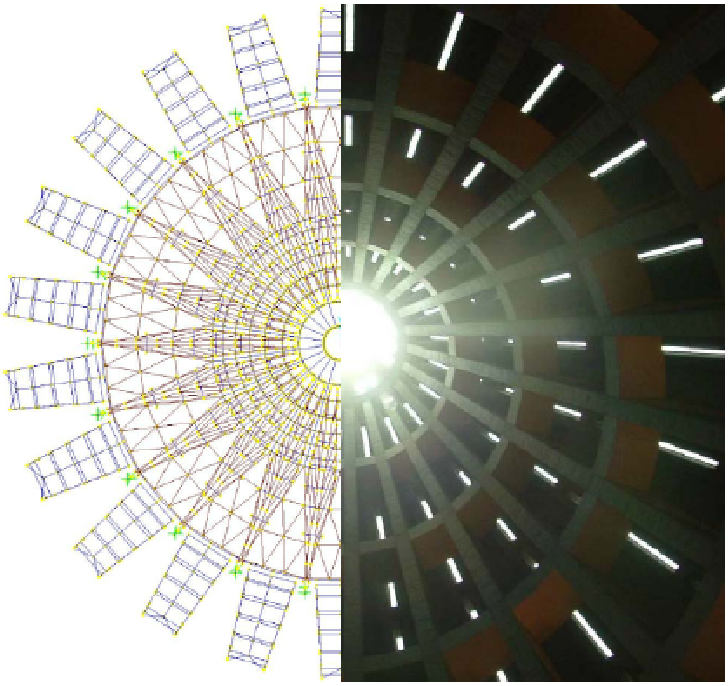

Figure 3.14 Plan SAP 2000/internal view.

The main beam ring, denoted by Ring 3, is designed at +4.00 m (the height of the p.r.c. ring) from the extrados of the Crypt cover plan. It is subdivided in full and hollow parts switching around the circumference. The full sections expand for ±2.363° on the right and on the left with respect to the columns while the remaining parts are hollow. From +4.00 m to +66.80 m are constructed the other eight sections (Table 3.4) approximately at inter-axes 8 m.

Table 3.4 Rings height.

RING	HEIGHT
	[m]
4	17.406
5	25.301
6	33.701
7	42.101
8	50.501
9	58.902
10	67.736
11	73.100

Also the Rings 10 and 11 have irregular sections: the full parts expand for ± 2.474° (Ring 10) and ± 9.572° (Ring 11) on the right and on the left with respect to the axes of the columns and the others parts are hollow. The subvertical elements' section thickness is 20 cm, but the horizontal section of each one is variable at different heights and they are reported in Table 3.5, while Figure 3.15 shows the Finite element model and the geometric construction.

Table 3.5 Subvertical sections.

SUB VERTICAL ELEMENT	**HEIGHT**	**SECTION**
	[m]	[m]
4	17.406	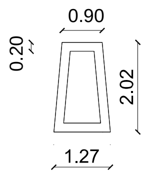
5	25.301	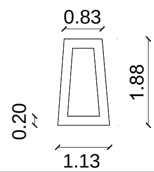
6	33.701	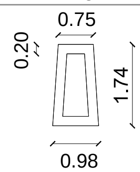
7	42.101	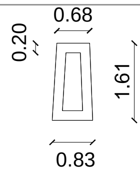
8	50.501	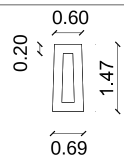
9	58.902	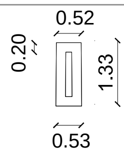
10	67.736	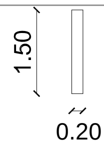

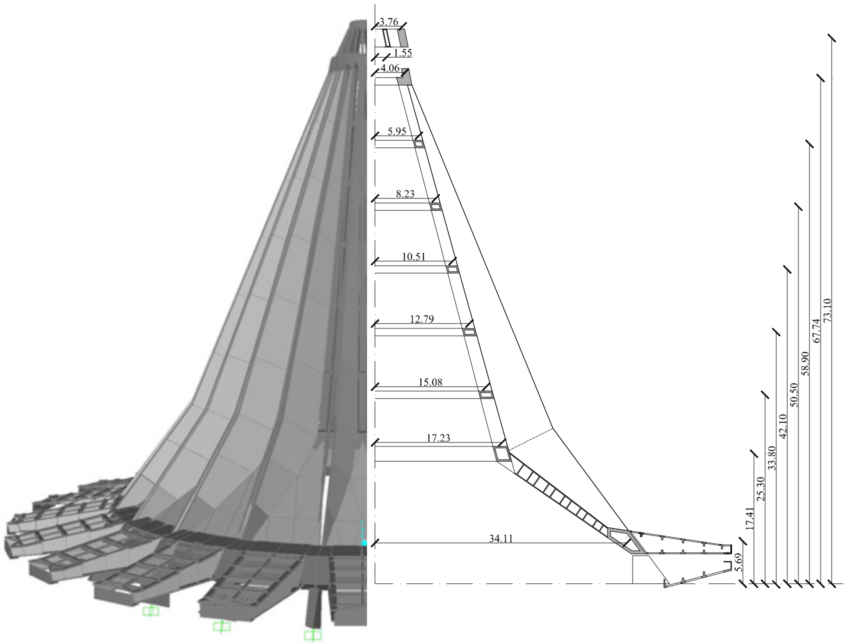

Figure 3.15 Extrude view section/geometric construction.

The rings have been designed using *grid lines* with variable radii, inversely proportional to the height. On the external side of the circumference there are 19 chapels. The lower part of these chapels (at +4.00 m) is connected to the prestressed reinforced concrete ring by means of two body constraints (at two lateral ends); the transversal T shape beams are horizontal and the longitudinal beams are only in the lateral extremely. The L section beam is connected with the higher external part by a body.

The lateral walls of the chapels are shell elements 20 cm thick. From Ring 3 (p.r.c.) to Ring 4, considering the horizontal section, and between the subvertical elements (considering the vertical section) there are 21 shell elements. Table 3.6 shows, for each ring, the heights of the centers of mass and the radii of the *grid lines*.

Table 3.6 Rings positions.

RING	HEIGHT	RADIUS
	[m]	[m]
3	5.69	34.105
4	17.41	17.229
5	25.30	15.079
6	33.70	13.402
7	42.10	10.515
8	50.50	8.228
9	58.90	5.947
10	67,736	4.005
11	73.100	1.550

Each shell element is subdivided into 8 parts having a thickness calculated as the theoretical thickness of a parallelepiped with the base 2.85mx1.00m wide. Points 2 and 3 (Figure 3.16) of each singular shell are connected to the Ring 3 with a body constraint and so at the chapel. Points 1 and 4 are connected at the Ring 3 with a body constraint and therefore at the top of the columns. Aligned with the columns there are 22 wings subdivided in 9 parts from Ring 3 to Ring 10 (at the top of the dome).

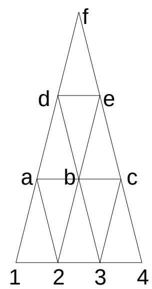

Figure 3.16 Subdivision of a shell.

The internal joints of the wings are connected to the *Sections* by means of body constraints and the wings are tilted so that the relative distance between two adjacent wings is constant and equals to 70 cm (space for the windows). Figure 3.17 shows the complete geometrical study of the Church.

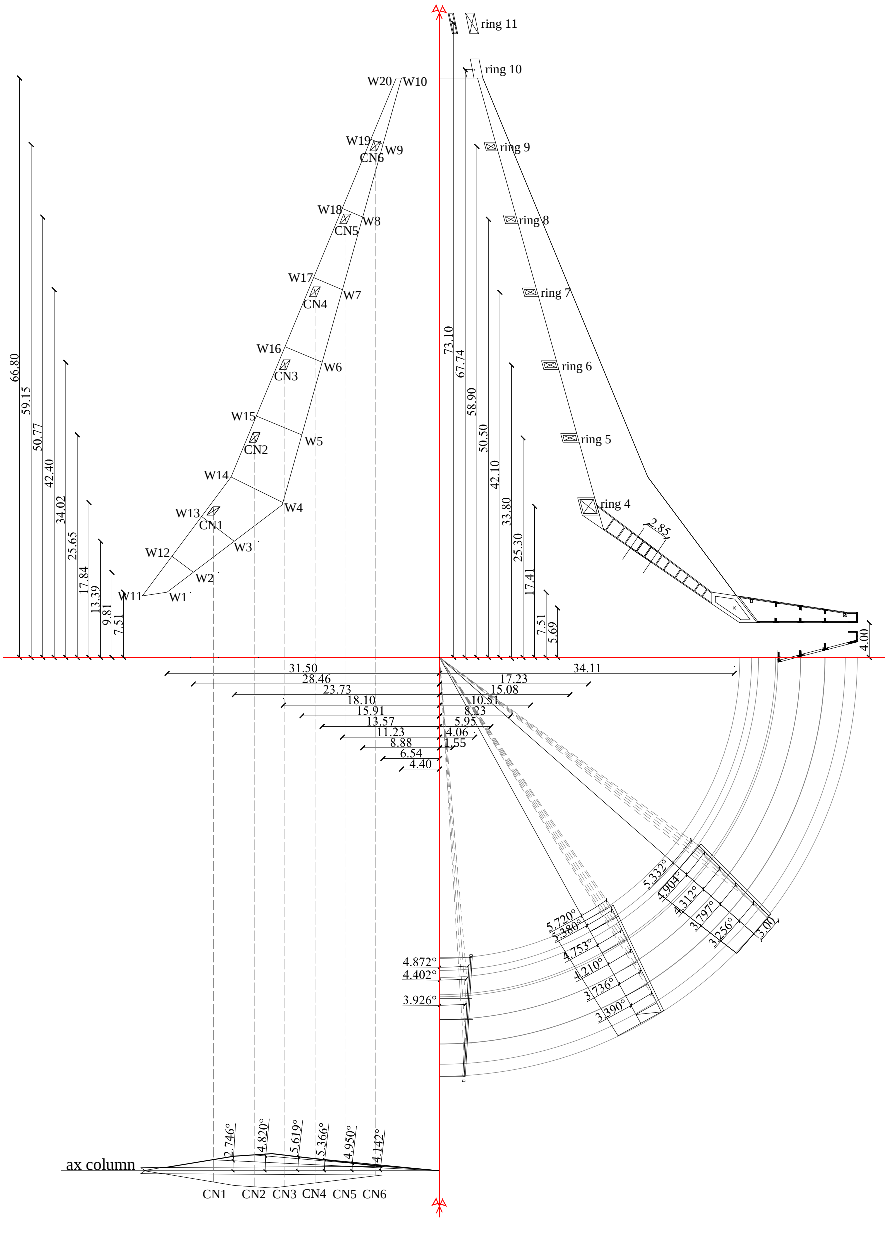

Figure 3.17 Geometrical study.

The two wings of each column are interconnected by means of 6 sections 0.80x1.20m placed 40 cm inside with respect to the external border of the wings. Figure 3.18 shows the complete SAP model.

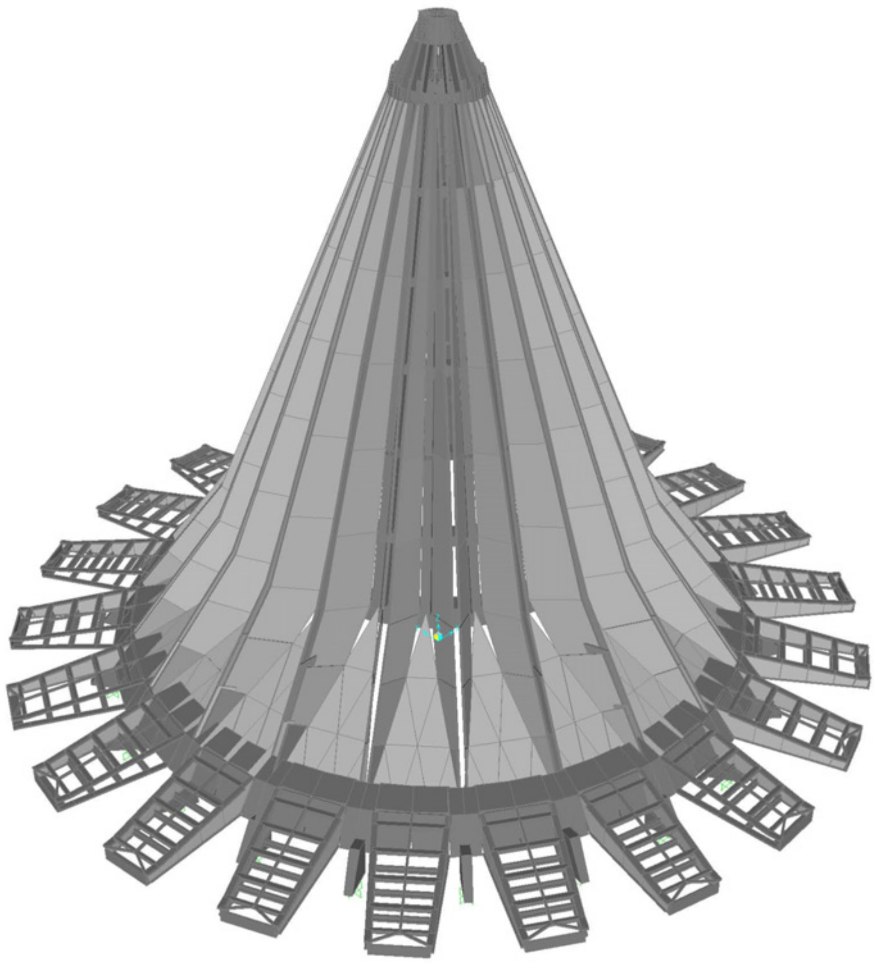

Figure 3.18 Complete SAP model.

3.7 Structural performance after the isolation intervention

The numerical analyses carried out on the numerical model of the construction, assuming the dome as a rigid body, are summarized in this paragraph: the seismic input is represented by 7 couples of artificial accelerograms compatible with the elastic response spectrum defined by the new code (Ministerial Decree of 14 January 2008) and for each accelerogram a duration of 26s has been assumed.

Figure 3.19 refers to one couple of accelerograms and shows the force – deformation cycles in transversal direction for one of the 22 new dissipative devices.

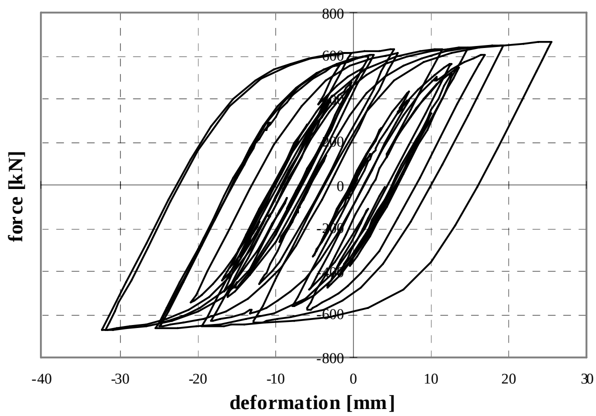

Figure 3.19 Force-deformation cycles in the isolator.

Table 3.7 provides the maximum values, in radial and tangential directions, of the shear forces expressed in kN (T_{rad} and T_{tan}, respectively) and the bending moments expressed in kN·m (M_{rad} and M_{tan}, respectively), at the base of all the 22 piers: it shows, for each kind of action, the per cent reduction determined by the seismic isolation intervention. It can be observed, as expected, that the isolation of the dome from the columns determines a considerable reduction of the shear forces and bending moments in the piers, at the same time introducing dome's displacements widely lower than those allowed by the new bearings (Serino *et al.*, 2008c).

Figure 3.20 shows the maximum values considering 7 different indicators correspondent to the 7 couples of accelerograms: the results relative to the structure before the seismic isolation (BI) are reported in dark green, while the results relative to the isolated structure (AI) are shown in fuchsia with the same indicators. The figure makes clear, for each kind of action, the reduction determined by the seismic isolation intervention.

Table 3.7 Shear forces [kN] and bending moments [kN·m] in the piers.

Pier	Radial bending stress M_{rad}			Tangential bending stress M_{tan}			Radial shearing stress T_{rad}			Tangential shearing stress T_{tan}		
	Before isolation	After isolation	Variation [%]	Before isolation	After isolation	Variation [%]	Before isolation	After isolation	Variation [%]	Before isolation	After isolation	Variation [%]
1	8779	1517	– 83	11838	2137	– 82	2360	412	– 83	2889	521	– 82
2	1565	704	– 55	7576	2939	– 61	394	195	– 51	1849	717	– 61
3	95893	1925	– 98	19329	899	– 95	25068	518	– 98	4717	220	– 95
4	1652	575	– 65	7664	2820	– 63	389	184	– 53	1870	688	– 63
5	8776	1462	– 83	9683	2133	– 78	2344	401	– 83	2794	521	– 81
6	84745	1790	– 98	16877	817	– 95	22154	473	– 98	4118	199	– 95
7	21426	1660	– 92	14120	1462	– 90	5661	449	– 92	3446	357	– 90
8	3522	1081	– 69	7779	2552	– 67	908	297	– 67	1898	622	– 67
9	1214	210	– 83	7222	3068	– 58	240	58	– 76	1762	748	– 58
10	3532	1144	– 68	9630	2751	– 71	958	299	– 69	2350	671	– 71
11	26779	1906	– 93	14571	1570	– 89	7059	496	– 93	4313	383	– 91
12	95893	1925	– 98	19329	899	– 95	25068	518	– 98	4717	220	– 95
13	8779	1518	– 83	1184	2137	+ 80	2360	412	– 83	2889	521	– 82
14	1565	704	– 55	7576	2939	– 61	394	195	– 51	1849	717	– 61
15	1652	648	– 61	7664	2820	– 63	389	184	– 53	1870	688	– 63
16	8776	1462	– 83	9683	2133	– 78	2344	401	– 83	2794	521	– 81
17	84745	1790	– 98	16877	817	– 95	22154	473	– 98	4118	199	– 95
18	21426	1660	– 92	14120	1462	– 90	5661	449	– 92	3446	357	– 90
19	3522	1081	– 69	7779	2552	– 67	908	297	– 67	1898	622	– 67
20	1214	210	– 83	7222	3068	– 58	240	58	– 76	1762	748	– 58
21	3532	1144	– 68	9630	2751	– 71	958	299	– 69	2350	671	– 71
22	26779	1906	– 93	17674	1570	– 91	7059	496	– 93	4313	383	– 91

Piers with maximum shear force or bending moment
Piers with maximum reduction of action

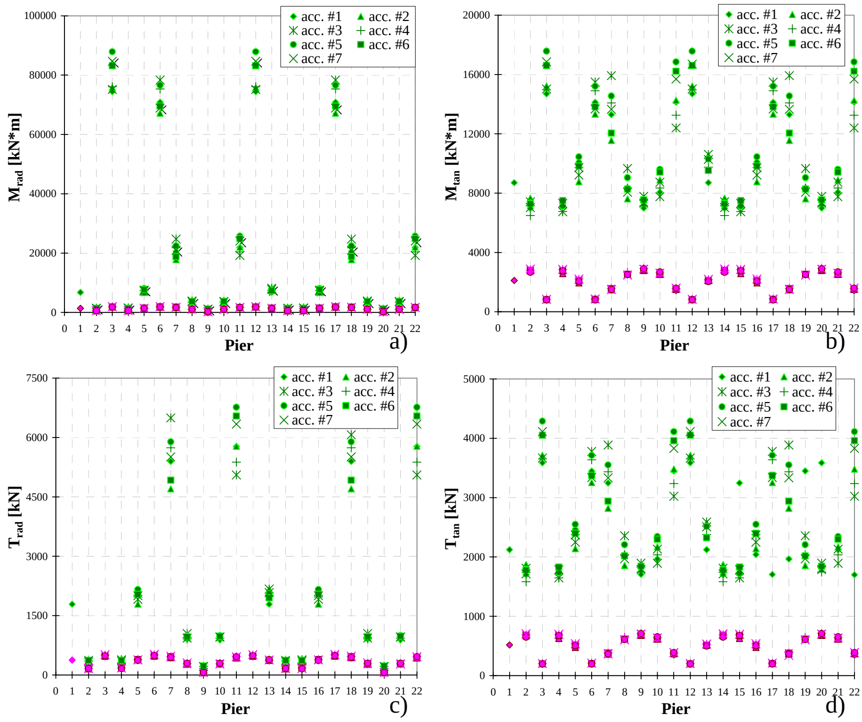

Figure 3.20 Reduction of structural response: radial bending stress (a), tangential ending stress (b), radial shearing stress (c), tangential shearing stress (d).

3.8 Description of the original monitoring system and the design of the upgraded

The design of the original monitoring system, completed in December 1995, provided for the monitoring of: (a) the radial displacements and the rotations in the radial plane of 12 of the 22 bearings; (b) the deformations in 24 vibrating-wire strain gages at 4 of the 22 columns below; (c) the vertical displacements of the annular beam at elevation +16.40 m; (d) the accelerations at 14 points properly distributed among the Crypt plane (elevation -10.80 m), at the top of the r.c. columns supporting the dome and at the intrados of the annular beam (elevation +4.00 m), at the level of the further annular beam immediately above (elevation +16.40 m), and at the top of the structure. As the weather environmental conditions can determine a variation of the above listed parameters, the design of the monitoring system included also the control of: (e) the internal temperature and relative humidity of the upper church by 4 of the 22 columns placed according to the 4 cardinal points; (f) the velocity and direction of the wind, the external temperature and relative humidity at the top of the structure. The drawings shown in

Figure 3.21 make clear the locations of most of the sensors of the old monitoring system, together with the modifications introduced by the upgrading of this system: the legend allows to understand the scheme of the pre-existent and new sensors. The data acquired, adequately processed, could have allowed the identification of the structural system, in addition to the control and prediction of its behaviour under the external actions. The accelerations (d) should have been acquired automatically and processed by a dynamic data station, consisting of a PC with data acquisition boards for the acceleration sensors and their signal conditioners; the quantities (a) and (b) automatically by a static data station, consisting of a second PC interfaced with a remote data acquisition station; the environmental parameters (e) and (f) automatically by a weather data station, consisting of a third PC interfaced with a further remote data acquisition station; the displacements (c) should have been measured periodically using a mobile topographic station.

The conditions of the original monitoring system were quite satisfactory: however, some sensors were found damaged, and the three pre-existent static, dynamic and weather data acquisition systems, though still working, were obsolete and had to be updated. The identical PCs of the three data acquisition systems, besides being obsolete, were also little suited for a continuous monitoring of the structure. The rehabilitation and upgrading design of the existing monitoring system provides for the substitution of the obsolete equipment with new dedicated digital instrumentation equipped with power and mass storage convenient for a continuous monitoring, and the addition of a server connected to the Internet network for the centralized storage of the data coming from the data acquisition systems and the possibility to examine such server and download the data by a remote authority via Internet. This allows a more efficient check of the real condition of the construction, with management costs of the whole system much lower than those corresponding to the periodical visit of specialized personnel. The proposed solution of an effective continuous monitoring system of the Sanctuary is based on the use of only one digital dynamic acquisition system with 64 channels, which are planned to be connected to: the 30 pre-existent accelerometers (20 by the Crypt plane and the bearings, and the remaining 10 at elevation +16.40 m and on the top of the dome); 8 new displacement transducers to be placed in couples by 4 of the 22 bearings, and having a stroke compatible with the maximum design displacement of the isolators (±200 mm in radial direction and ±150 mm in tangential direction);

5 thermo-hygrometers to measure the temperature and relative humidity; 1 barometer and 1 tachy-gonio-anemometer (measuring the velocity and direction of the wind) of the old monitoring system (Serino *et al.*, 2008a). Therefore, at present, it has been decided not to connect the 12 mono-axial inclinometers and the 24 vibrating-wire strain gages, and to uninstall the existing displacement transducers having a stroke (±10 mm), completely inadequate with respect to the new requirements. A special attention is devoted to the autonomy of the acquisition/processing/storage system (acquisition system + server) for lack of electric energy, and to the automatic restoration of the continuity of the system after a blackout. Indeed, an Uninterruptible Power System is provided for the acquisition system, the server and the relevant peripheral devices, dimensioned in order to guarantee at least 30 min of autonomy, and configured via software for the automatic shutdown of the server after 20/25 min; furthermore, the server is configured in terms of hardware and software, so that it can automatically restart and all the applications are restored as soon as the network power returns.

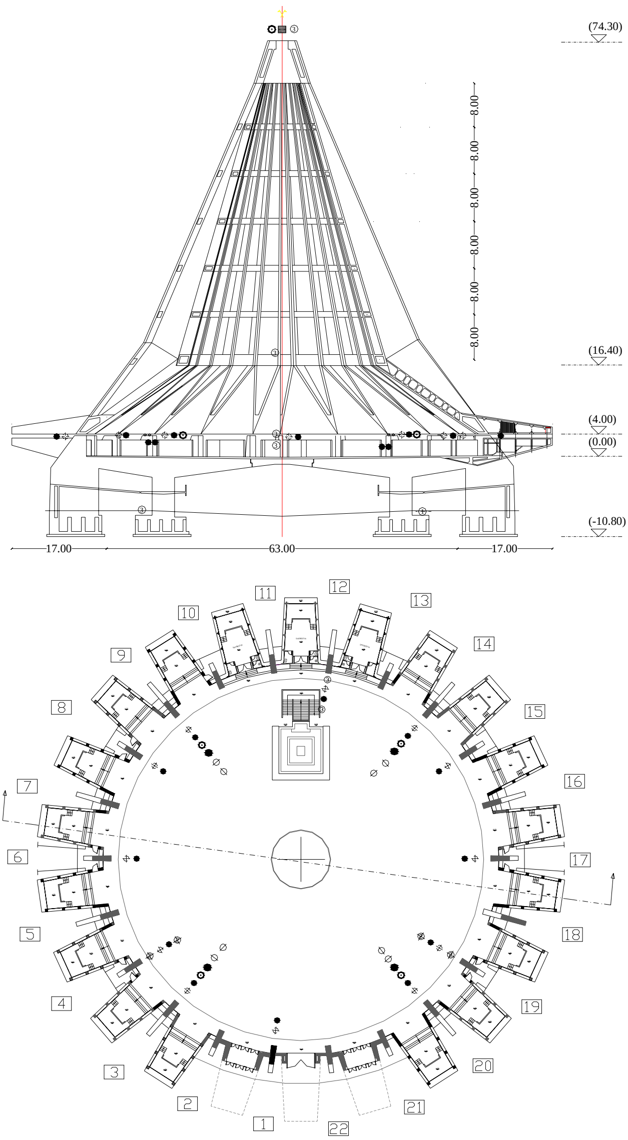

SENSORS CONNECTED TO THE NEW ACQUISITION SYSTEM	
①	UNIDIRECTIONAL ACCELEROMETER
②	BIDIRECTIONAL ACCELEROMETER
③	TRIDIRECTIONAL ACCELEROMETER
⊖	NEW UNIDIRECTIONAL DISPLACEMENT TRANSDUCER
⊙	THERMO-HYGROMETER
	BAROMETER
▦	TACHY-GONIO-ANEMOMETER

OLD SENSORS NON CONNECTED TO THE NEW ACQUISITION SYSTEM	
●	MONO-AXIAL INCLINOMETER
●	VIBRATING-WIRE STRAIN GAGE
	POSITION OF THE UNISTALLED DISPLACEMENT TRANSDUCER

Figure 3.21 Vertical section and plan at elevation 4.00 m: locations of the sensors.

3.9 The management and maintenance of the monitoring system

The "Santuario della Madonna delle Lacrime" has been accepted among the structures selected within the *Italian Observatory of Structures* (OSS) (Nicoletti *et al.*, 2005). The latter represents a network of the National Seismic Service (SSN) of the Italian Dept. of Civil Protection (DPC), which deals with a set of public constructions (buildings and bridges) in use in Italian seismic areas, which are instrumented with a local system, after a thorough study of their characteristics. This local system monitors permanently their seismic response, under the control of a network central computer, installed in the SSN headquarters, which also collects via modem and processes the recorded data. The OSS comprises: the Fundamental Network (105 public buildings, 12 bridges, 1 dam), with complete instrumentation and thorough theoretical and experimental study of the structure; the Additional Network (300 public buildings, strategic for Civil Protection), with simplified minimum instrumentation and collection of the available data only. The Project is mainly aimed at producing original data on the seismic behaviour of the selected structures, in order to assess the capacity of structures of special interest for the management of the seismic emergency (city halls, hospitals, schools, bridges and dams) to survive further shakes, and to disseminate the collected data to the scientific community for the progress of knowledge and the improvement of the technical regulations.

The digital dynamic acquisition system used for the monitoring of the "Santuario della Madonna delle Lacrime" has 64 channels and consists of two acquisition boards (DAQ), each one with 32 channels, which can be operated in different way in terms of sampling frequency and acquisition strategy. DAQ #1 is connected to the 30 accelerometers and is devoted to a threshold acquisition strategy, which is activated when a seismic event occurs that exceeds a fixed threshold value. DAQ #2 is connected to the 8 displacement transducers, the 5 thermo-hygrometers, the barometer and the tachy-gonio-anemometer, and is devoted mainly to compute and store the mean value recorded by the above sensors using a periodical acquisition strategy, which is going to be activated every 6 hours. Furthermore, using a continuous time acquisition strategy the mean and standard deviation, as well as minimum and maximum values of wind velocity and direction, over a 15 minutes period, is also recorded and stored, with a sampling frequency lower than that one required for the accelerometers during a seismic event and higher than that one required for the other sensors for the usual thermal variations. Besides, when a seismic event activates a threshold acquisition, the 8 displacement transducers are also acquired at the same sampling frequency of the accelerometers, so as to record dynamically also the relative displacements of the isolators. All the parameters of the three acquisition strategies (e.g., threshold value, sampling frequencies as well as duration and periodicity of acquisition) can be modified by a remote access via ADSL. Now, the updated monitoring system allows the automatic transfer of the data having a format compatible with the OSS's software over ftp areas, statically reachable via ADSL and indicated by the DPC: the data will be saved in different files according to the kind of acquisition strategy, and located in three proper directories.

The file containing the data of a threshold acquisition is produced at the end of a seismic event, while the files containing the data of a periodical acquisition and of a continuous time acquisition are delivered weekly. Then, the new monitoring system allows the transmission of alarms via e-mail and, in case, by SMS to predetermined addresses (for example, to the Dept. of Structural Engineering of the University of Napoli Federico II), besides having the possibility to be questioned, in case of need, by a remote access via ADSL, upon password authentication.

Chapter IV

4. A MOCK-UP MODEL FOR EXPERIMENTAL TESTS

Structural control techniques in mitigating seismic effects on constructions are becoming more and more popular in Italy. This is confirmed by the issuing of the "Nuove Norme Tecniche per le Costruzioni" released on February 4th 2008 (Ministerial Decree of 14 January 2008), encouraging the design and development of new applications within this area.

The damages suffered by buildings after catastrophical earthquakes lead to increasing repair cost, thus compelling the scientific community to develop appropriate control techniques that are efficient and cost effective as well.

An extensive set of dynamic experimental tests, named JetPacs - **J**oint **E**xperimental **T**esting on **P**assive and semi-**A**ctive **C**ontrol **S**ystems -, has been carried out within the topics no.7 of the ReLuis Project (University Network of Seismic Engineering Laboratories). These analyses have been performed by using a 2:3 scaled steel braced frame, available at the Structural Engineering Laboratory of the University of Basilicata, Potenza, Italy. The frame has been the subject of a wide experimental campaign which will be performed using an actuator with a maximum force of 500 kN and a maximum displacement of ±250 mm, driven by an hydraulic pump having a maximum flow rate of $1200l/\min$ and capable of applying accelerations up to *1g* (Serino *et al.*, 2008).

Present study aimed to conduct analytical investigations on the scaled prototype steel frame in two phases namely: *i)* the analytical determination of the model’s dynamic characteristics and the comparison of these results with those obtained during the dynamic characterization tests; *ii)* the extension of the study by conducting a time-history analysis on the analytical model with different damping devices and the comparison of the obtained results with those available from the experimental investigations. Structural response to both natural and artificial earthquakes was evaluated experimentally and analytically. During the experimental campaign, the structural model was subjected to three different sets of natural or artificial earthquakes, compatible with the response spectra of the Eurocode 8 and Italian seismic code (OPCM 3431, 2005) for soil type A, B and D (Ponzo *et al.*, 2007), i.e.:

(i) a set of natural records compatible with the response spectrum provided by Eurocode 8 for soil type A, Seismic Zone 1 (Figure 4.1);

(ii) a set of natural records compatible with the response spectrum provided by Eurocode 8 for soil type B, Seismic Zone 1 (Figure 4.2);

(iii) a set of artificial acceleration profile type Spectrum-compatible waveforms with the response spectrum provided by OPCM 3431 (03.05.2005) for soil type D, Seismic Zone 1 (Figure 4.3).

Registrations of natural seismic inputs were scaled in acceleration by using a Scaling Factor (SF); then all the acceleration profiles are scaled down in time by a $(1.5)^{1/2}$ factor, for consistency with the scale of the model.

The dissipation systems, developed with different materials and technologies, consist of six different types of passive or semi-active energy dissipating devices with different behaviours. All the devices are based on both currently used (i.e. viscous, visco-elastic, metallic yielding steel plates) and innovative technologies (i.e. shape memory alloy wires, magnetorheological fluids).

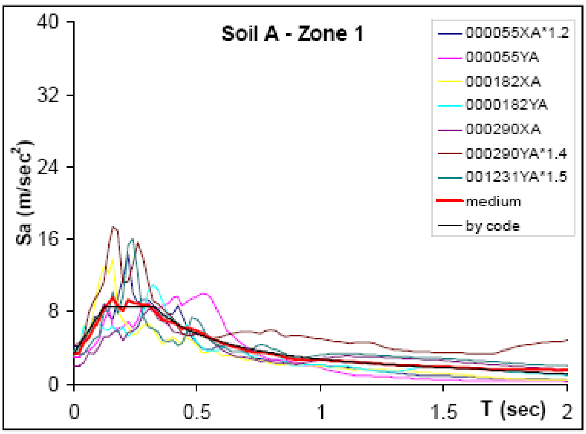

Figure 4.1 Elastic response spectra of a set of natural accelerograms for soil type A, Seismic Zone 1; time scaled down as ($t/\sqrt{1.5}$).

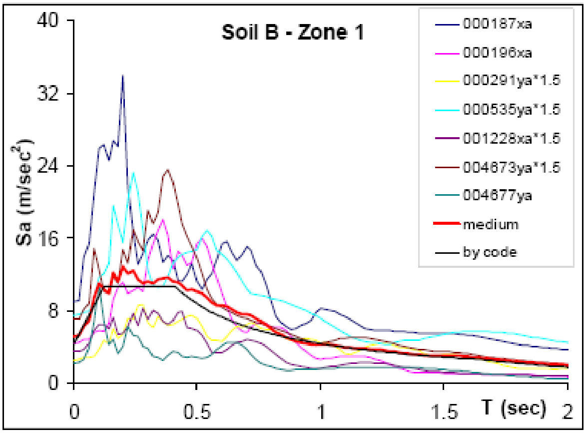

Figure 4.2 Elastic response spectra of a set of natural accelerograms for soil type B, Seismic Zone 1; time scaled down as ($t/\sqrt{1.5}$).

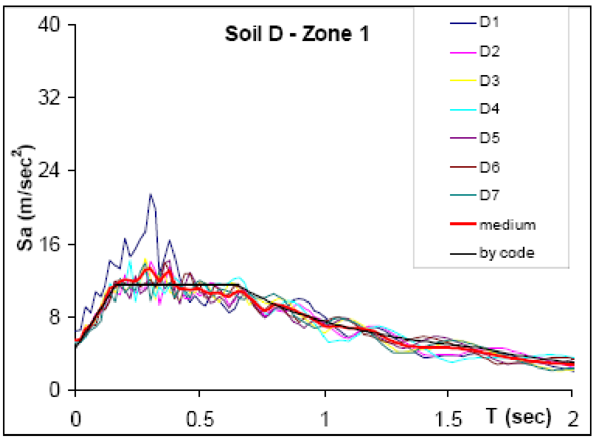

Figure 4.3 Elastic response spectra of a set of artificial accelerograms for soil type D, Seismic Zone 1; time scaled down as ($t/\sqrt{1.5}$).

Table 4.1 reports the list of the devices proposed for the investigation, while Figure 4.4 and Figure 4.5 show pictures of the two devices that have been tested at the Structural Engineering Laboratory of University of Naples Federico II.

Table 4.1 Energy dissipation devices proposed for the investigations.

No.	Type	Manufacturer
1	viscous fluids	FIP Industriale, Italy
2	visco-elastic materials	Jarret Industries, France
3	magnetorheological fluids	Maurer&Söhne, Germany
4	magnetorheological fluids	LORD Corporation, USA
5	visco-re-centring elements	TIS (Rome), Italy
6	hysteretic components	

Figure 4.4 Viscous device by FIP Industriale.

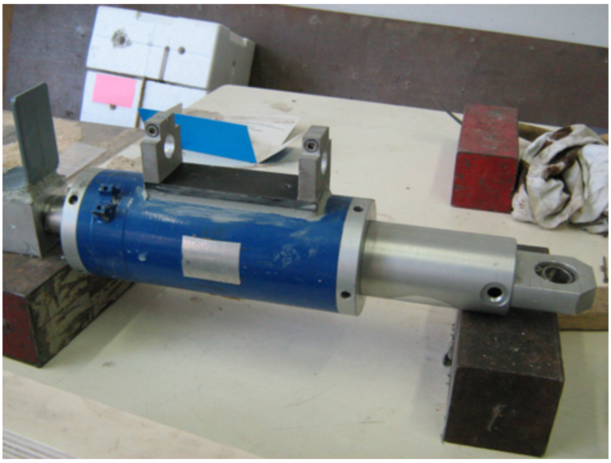

Figure 4.5 Magnetorheological device by Maurer&Söhne.

Experimental investigations of the reported devices and verification of the experimental results by analytical modelling are scarce in the literature. The main goals of the analytical studies are: *i*) to validate the proposed analytical model by comparing its modal characteristics with those obtained from experimental investigations; *ii)* to improve the knowledge about the frame's behaviour by using the energy dissipating devices systems listed above; *iii)* to simplify and standardize the design procedures for buildings equipped with such dissipating bracing systems.

4.1 JETPACS mock-up model description

The JETPACS mock-up model is a two storeys one-bay steel frame with composite steel-reinforced concrete slabs. The model has been experimentally analyzed in three different configurations namely: *i)* bare frame without any additional mass, designated as CB; *ii)* frame with four additional concrete blocks at first and second floors close to each corner, designated as CS; *iii)* frame with two additional concrete blocks on first and second floors placed eccentric with respect to mass center, designated as CN.

The JETPACS mock-up model is of plan size 3m *x* 4m with a height of about 4.5 m (dimensions refer to member axes). Figure 4.6 shows an image of the model available at Potenza, whereas Figure 4.7 shows its plan, elevations and a 3D view.

Figure 4.6 Image of the JETPACS model in Potenza.

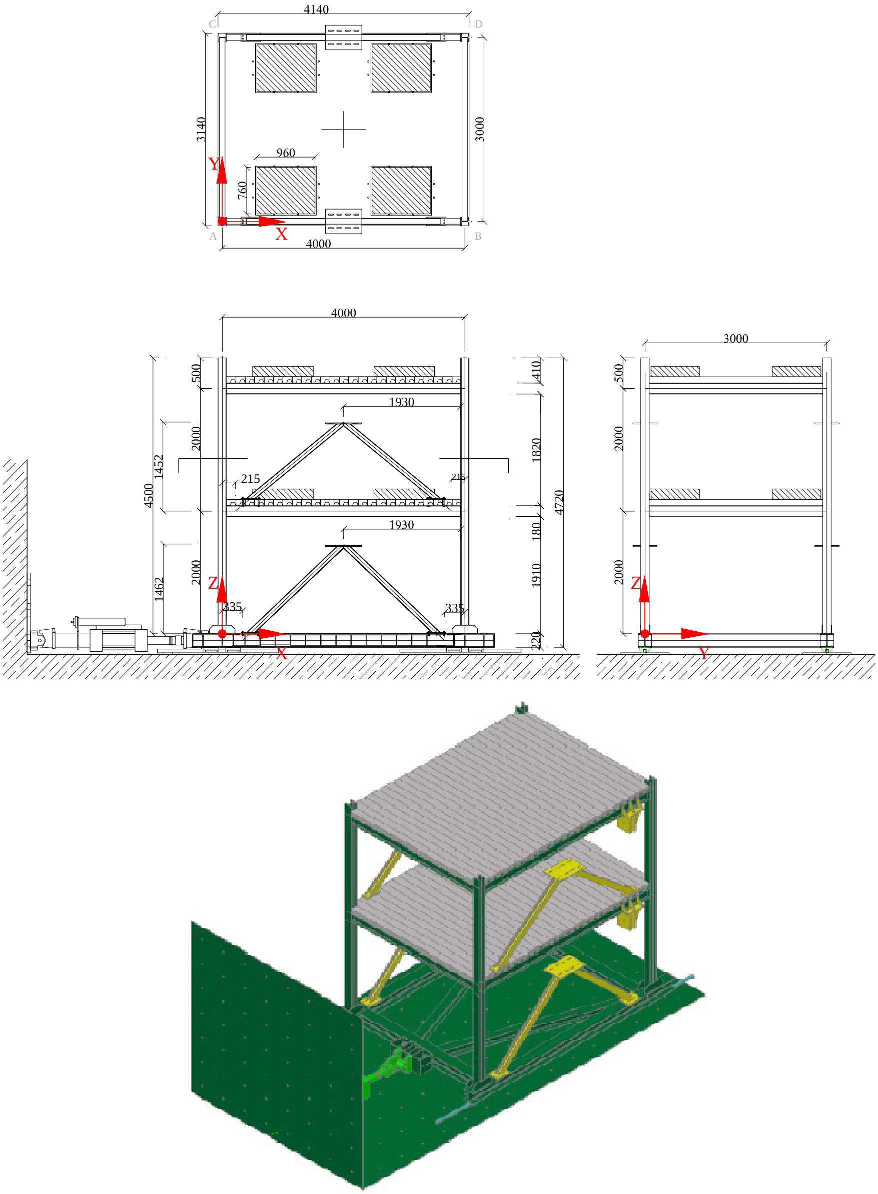

Figure 4.7 JETPACS model: plan; front elevation; side view; 3D view.

The frame has three floors namely: *i)* ground floor or base level; *ii)* first floor; and *iii)* second floor. Four HEB140 columns, designated as A, B, C and D and shown in Figure 4.7 are placed at the corners with their flanges oriented parallel to the transverse Y axis. These columns extend by 410mm above the second floor level. Four IPE180 lateral beams, welded to the columns to reach a high degree of rigidity, form the first and second floors while four lateral HEB220 beams form the ground floor. In order to have sufficient stability and comfortable mounting of the loading jack, a horizontal HEA160 bracing is provided on the XY plane at the ground floor.

To facilitate the mounting of different dissipating devices, chevron type HEA100 bracings are mounted parallel to XZ plane in both the storeys and are connected to the respective lower floor beams. It is interesting to note that the connection nodes at the base of the bracings are well away from the columns, thus offering the required degree of flexibility to the frame.

The bracings' tops are fitted with a gusset plate on which proposed damping devices shall be housed (Figure 4.8 and Figure 4.9). All the structural elements are made of Fe360 steel having a characteristic yield strength of 235 N/mm^2 and a characteristic ultimate strength of 360 N/mm^2. A concrete slab supported by coffer steel A55/P600 section with 0.8 mm thickness is provided on both the first and second floors (Figure 4.10).

The frame is supported on special sliding 1D guides positioned under the base beams, close to the columns, which allow the frame to move in the longitudinal X direction only. The sliding guides were kept locked during the above mentioned dynamic characterization tests.

Figure 4.8 Plate (at the top of the braces) to house damping device.

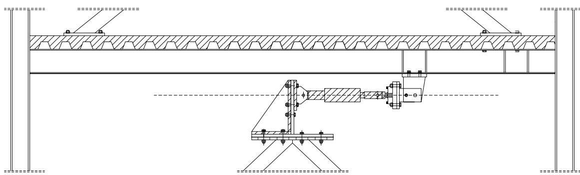

Figure 4.9 Connection detail.

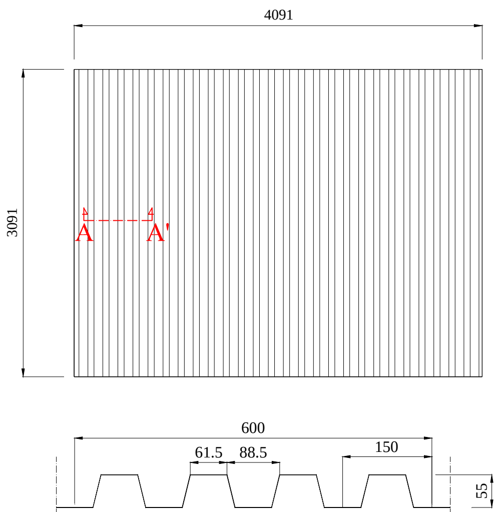

Figure 4.10 Details of coffer support for RC slab: plan and section AA’.

It is well known that the efficacy of semi-active devices in controlling the dynamic response of a structure increases with the increase of the ratio between the first vibration period of the structure and the time reactivity of the device. In order to elongate the vibration periods of the test frame, a modified symmetrical configuration has been obtained by adding four concrete blocks on each floor. Table 4.2 shows the designation of the additional masses comprised of concrete blocks, along with their dimensions and the geometric coordinates of their centre. (Ponzo *et al.*, 2007). Figure 4.11 describes the position of these additional masses.

Table 4.2 Additional masses locations of the concrete blocks for symmetric configuration frame (CS).

Added Mass Identification	Floor	Position near to column	Mass (kg)	Dimensions (mm)		Coordinates of the block center (mm)	
				D_X	D_Y	X	Y
MA-I	I	A	338	960	760	1050	500
MB-I	I	B	340	960	760	2950	500
MC-I	I	C	336	960	760	2950	2500
MD-I	I	D	336	960	760	1050	2500
MA-II	II	A	336	960	760	1050	500
MB-II	II	B	340	960	760	2950	500
MC-II	II	C	338	960	760	2950	2500
MD-II	II	D	330	960	760	1050	2500

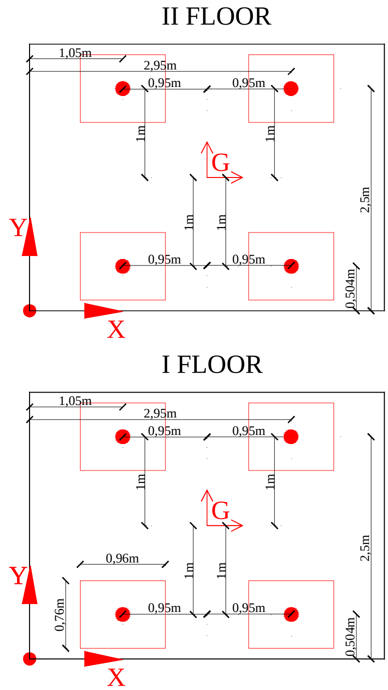

Figure 4.11 Position of additional masses for symmetric configuration (CS).

In order to investigate the capability of passive and semi-active energy dissipating devices in controlling the torsional behavior of asymmetric steel framed building, a modified configuration of the mock-up frame has been considered with only two additional concrete blocks on both the first and the second floors, creating eccentricity with respect to the mass center. Figure 4.11 shows the designation of the additional masses given by the concrete blocks, along with their dimensions and the geometric coordinates of their centers, while Table 4.3 describes the position of these additional masses.

Table 4.3 Additional masses locations of the concrete blocks for asymmetric configuration frame (CN).

Mass Identification	Floor	Position near to column	Mass (Kg)	Dimensions (mm)		Coordinates of block center (mm)	
				D_X	D_Y	X	Y
MA-I	I	A	352	960	760	1050	500
MB-I	I	B	354	960	760	2950	500
MA-II	II	A	350	960	760	1050	500
MB-II	II	B	354	960	760	2950	500

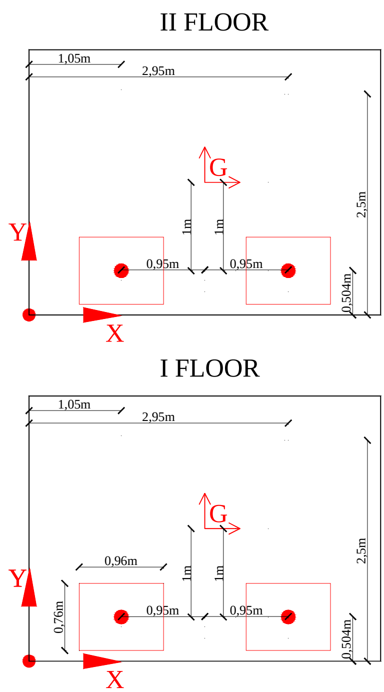

Figure 4.12 Position of additional mass for asymmetric configuration (CN).

4.2 Analytical models of a JETPACS frame

Based on the detailed description of the JETPACS Mock-up model, attempt has been made to closely simulate the test specimen using the SAP-2000 software in order to match the experimental results of the dynamic characterization tests conducted at Structural Engineering Laboratory of the University of Basilicata in Potenza.

The finite element model developed software consists of 39 nodes and 35 elements: 8 HEB140 column elements for the two storeys and further 4 elements extended beyond the second floor; 4 beam elements of IPE180 at each of the two upper levels and 5 beam elements of HEB220 at the ground floor; 2 HEA160 elements for horizontal bracing at ground floor and 8 HEA100 elements for the vertical bracings at the upper floors (Spizzuoco *et al.*, 2008). Material characteristics are assigned as steel with a density of 7850 kg/m^3 and elastic moduli of E=2x10^5 N/mm^2 and ν=0.3, respectively. A master node at centre of each floor, to which the mass in each floor shall subsequently be assigned, is modeled with two translational (along X and Y axes) and one rotational degrees-of-freedom. Diaphragm constraints are assigned to the nodes of each floor with respect to their corresponding master node in order to ensure a rigid diaphragm action. All the four column nodes in the ground floor are assigned with restraints in all the three translational directions, making them fixed support. Figure 4.13 shows the extruded geometry and nodes identification number of the SAP model.

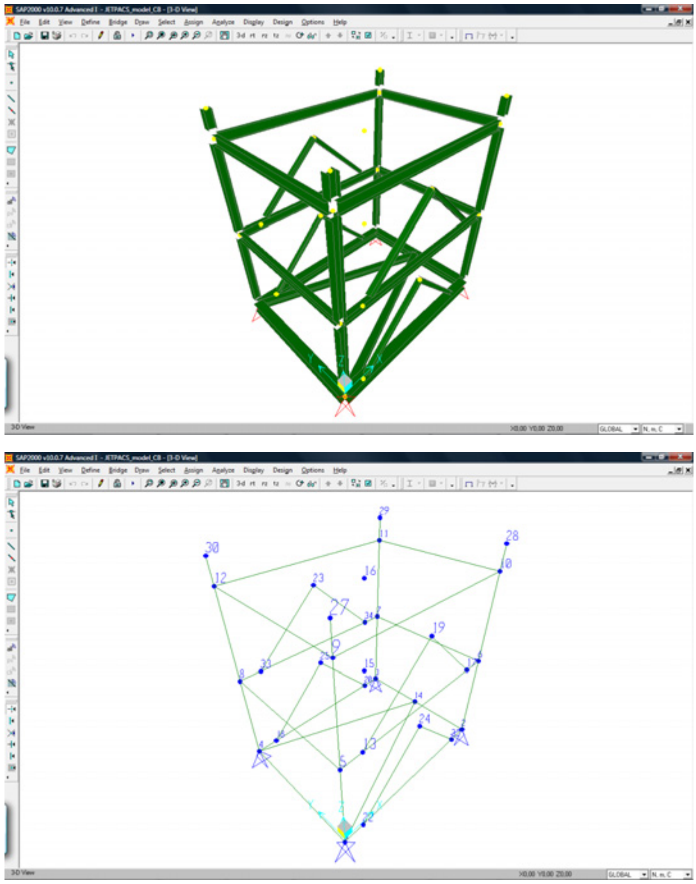

Figure 4.13 Analytical model simulated in SAP software: extruded view and nodes identification number.

The end offsets of column, beam and brace elements (i.e. the length of overlap for a given element with the other connecting element at a joint) are computed automatically from their intersection: to ensure the connectivity similar to that provided to the experimental mock-up model, factor of rigid zone is assigned as 0.5 (for partial fixity), which means that only half of each end offset is assumed to be rigid for bending and shear deformations. Figure

4.14 explains why the end offsets of the column elements at the base of the frame have been assumed equal to 250 mm.

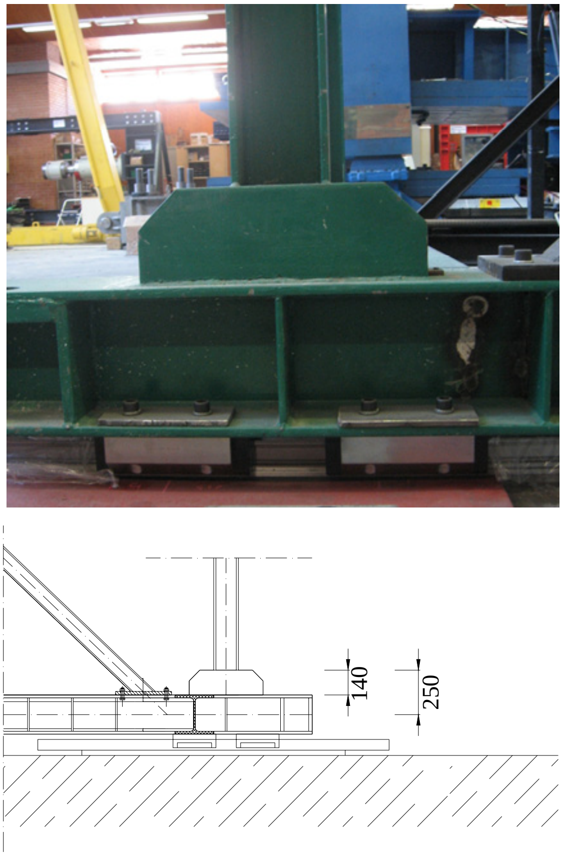

Figure 4.14 Image and sketch of the end offset details at the base used in the analytical model.

The floor slabs are comprised of reinforced concrete, resting on a coffer steel base A55/P600 of 0.8 mm thick (see Figure 4.10). As the span of the beams are large, a considerable sagging effect on the cover slab was observed when concrete was poured to create the cast-in-situ reinforced concrete slab, of course maintaining a horizontal level at the top. Therefore, thickness of the slab is not constant and was not measured and some additional volume of concrete has to be considered to take care of the sagging effect. First, the mass to be assigned to the master node at each floor was computed without considering the above mentioned sagging effect, based on the elements comprising the respective floors and is shown below:

Plan area of the coffer (as measured actually):

$$A_{tot} = 3.091 \cdot 4.091 = 12.634 m^2 \quad (4.2.1)$$

The mass per unit area of coffer is equal to 10.45 kg/m^2 so the mass of coffer steel support is:

$$12.645 \cdot 10.45 = 132 kg \quad (4.2.2)$$

The mass due to the cover slab is computed based on the details of coffer cross-section. It is seen from the Figure 4.10 that cross-section area of the coffer is the sum of 26 sub-elements of trapezoidal shape in X direction. The area of sub-elements is:

$$26 \cdot \frac{1}{2} \cdot 0.055 \cdot (0.0885 + 0.0615) = 0.107250\, m^2 \quad (4.2.3)$$

The volume of the sub-elements is:

$$0.107250 \cdot 3.091 = 0,3315 m^3 \quad (4.2.4)$$

Considering that the total thickness of the cover slab is 100 mm, thickness of concrete over the coffer bottom shall be 45 mm. The volume of reinforced concrete slab alone is:

$$3.091 \cdot 4.091 \cdot 0.045 = 0.569 m^3 \quad (4.2.5)$$

Hence total volume of concrete, including the troughs of the coffer bottom, shall be:

$$V_{tot} = V_{slab} + V_{coffer} = 0.569 + 0.3315 = 0.9005 m^3 \quad (4.2.6)$$

The mass of concrete cover is:

$$0.9005 \cdot 2500 = 2251 kg \quad (4.2.7)$$

and the total mass of RC slab and coffer is:

Mass (Eq. 4.2.2) + Mass (Eq. 4.2.7) = 2383Kg (4.2.8)

The rotational mass moment of inertia was computed considering the mass of the floor slab as uniformly distributed load is given by

$$I_{xy} = \frac{2383}{(3.091 \cdot 4.091)} \left[\frac{3.091 \cdot 4.091^3}{12} + \frac{4.091 \cdot 3.091^3}{12} \right] \text{ so:}$$

$$I_{xy} = 5220 \, kg \cdot m^2 \quad (4.2.9)$$

The mass of the column, beam and bracing elements are automatically computed and inserted in the finite element model by the SAP software, once their mass per unit length has been assigned.

4.3 Additional mass accounting for sagging effect and for symmetric (CS) and asymmetric (CN) configurations

Increase in thickness of slab due to the extra volume of concrete accounting for the sagging effect needs attention and cannot be ignored. Again in order to match the results of dynamic characterization tests, a uniform increase in thickness of 17 mm in the reinforced concrete slab has been considered, which corresponds to an increase of mass as given below:

$$3.091 \cdot 4.091 \cdot 0.017 \cdot 2500 kg / m^3 = 537 kg \quad (4.3.1)$$

Table 4.4 shows the mass values of the elements pertaining to each floor, computed considering all the beams supporting the floor, half of the column above and below each floor, and two complete braces for the first floor only. The revised rotational mass is computed as $I_{xy} = \frac{2920}{(3.091 \cdot 4.091)}\left[\frac{3.091 \cdot 4.091^3}{12} + \frac{4.091 \cdot 3.091^3}{12}\right]$ and will be:

$$I_{xy} = 6396 \; kg \cdot m^2 \tag{4.3.2}$$

Table 4.4 Computation of the mass on both the first and the second floor.

Element	Unit mass (kg/m)	Type	Length (m)		N.	1st floor mass (kg)	2nd floor mass (kg)
			1st floor	2nd floor			
Slab & coffer	(without considering sagging effect)					2383	2383
HEB 140	33.7	Column	2.055	1.50	4	277	202
IPE 180	18.8	Beam	14.0	14.0	1	263	263
HEA 100	16.7	Brace	2.194	2.110	4	147	Nil
Total (without considering the sagging effect)						3070	2848
Slab & coffer	(accounting for sagging effect)					2920	2920
Total (accounting for sagging effect)						**3607**	**3385**

These are the final values considered at master nodes of the first and second floors in the analysis. The slight increase in volume shall be seen as an approximate method accounting for the sagging caused to coffer steel on the bottom side by the weight of cast in situ concrete. Figure 4.15 shows the position and mass of the concrete blocks added in each floor, for symmetric and asymmetric configurations respectively.

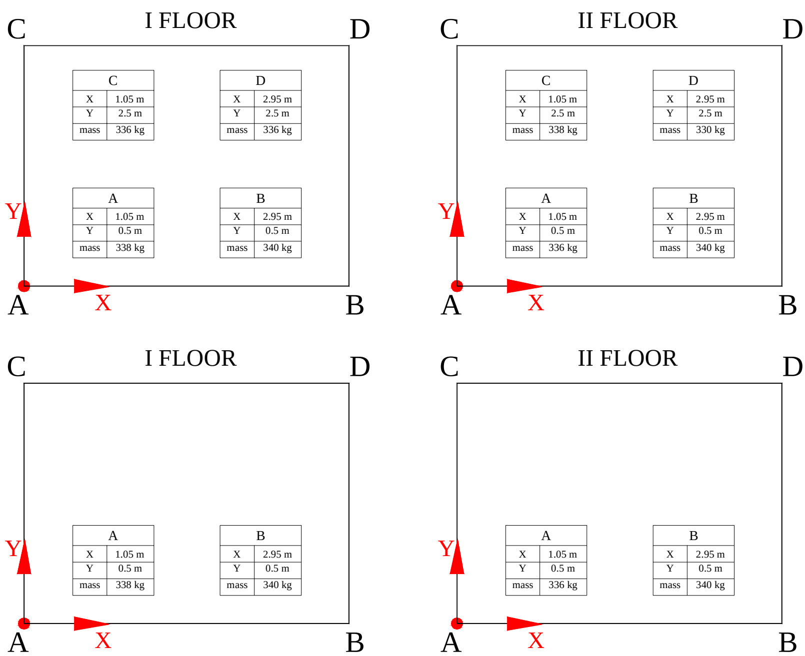

Figure 4.15 Position of additional concrete blocks for different configurations (CS and CN).

Table 4.5 shows rotational mass assigned to center of mass of each concrete block in the first and second floors due to the additional concrete blocks.

For example, for MA-I, we get:

$$I_{xy} = \frac{338}{(0.96 \cdot 0.76)} \left[\frac{0.96 \cdot 0.76^3}{12} + \frac{0.76 \cdot 0.96^3}{12} \right] \Rightarrow \qquad (4.3.3)$$

$$I_{xy} = 42.23 \; kg \cdot m^2$$

Table 4.5 Rotational mass due to additional concrete blocks.

Added Mass Identification	Floor	Position near to column	M (kg)	Rotational mass ($kg \cdot m^2$)
MA-I	I	A	338	42.23
MB-I	I	B	340	42.48
MC-I	I	C	336	41.98
MD-I	I	D	336	41.98
MA-II	II	A	336	41.98
MB-II	II	B	340	42.48
MC-II	II	C	338	42.23
MD-II	II	D	330	41.23

4.4 Connectivity between floor beams and slab

The dynamic characteristics of the analytical model strongly depend on the extent of connectivity between the floor beam and the reinforced concrete slab. Contribution of this monolithic action alters the moment of inertia of the beam to be considered in the analysis. Appropriate moment of inertia, accounting for this monolithic action, in case of full connectivity, is computed based on the current code (Ministerial Decree of 14 January 2008, Clause 4.3.2.3). The effective width can be determined as follows:

$$b_{eff} = b_0 + \beta b_{e1} + b_{e2} \tag{4.4.1}$$

where b_0 is the distance between the connections, b_i is half of the distance between the axes of the two beams, L_e is the longitudinal span of a supported beam and b_{e1} is the minimum between $\frac{L_e}{8}$ and

b_i. The ratio β has been calculated according to the expression $\beta = \left(0.55 + 0.025 \cdot \frac{L_e}{b_{ei}}\right) \leq 1.0$.

Considering the slab having a constant thickness of 100 mm:

a) In the X direction:

$$\beta = 0.55 + 0.025\left(\frac{4000}{3000/2}\right) = 0.616 \leq 1.0 \qquad (4.4.2)$$

$$b_{eff} = 90 + 0.616\left[\min\left(\frac{3000}{2};\frac{4000}{8}\right)\right] = 398mm \qquad (4.4.3)$$

and the effective moment of inertia for n=15 is:

$$I_{33x}^{cls*} = I_{33}^{s} + \left[\frac{398\,x100^3}{12} + (398\cdot 100)140^2\right]\frac{1}{n} \qquad (4.4.4)$$

$$= 1.317\cdot 10^{-5} + 5.42164\cdot 10^{-5} = 6.79864\cdot 10^{-5}\, m^4$$

The ratio of increase in moment of inertia of the floor beam (IPE180, whose moment of inertia is $1.317\cdot 10^{5} m^4$) is given by:

$$\frac{I_{33x}^{cls*}}{I_{33}^{s}} = \frac{6.79864\cdot 10^{-5}}{1.317\cdot 10^{-5}} = 5.16 \qquad (4.4.5)$$

a) In the Y direction:

$$\beta = 0.55 + 0.025\left(\frac{3000}{4000/2}\right) = 0.5875 \leq 1.0 \qquad (4.4.6)$$

$$b_{eff} = 90 + 0.5875\left[\min\left(\frac{4000}{2};\frac{3000}{8}\right)\right] = 310mm \qquad (4.4.7)$$

$$I_{33y}^{cls*} = I_{33}^{s} + \left[\frac{310\cdot 100^3}{12} + (310\cdot 100)140^2\right]\frac{1}{n} \qquad (4.4.8)$$

$$= 1.317\cdot 10^{-5} + 4.22289\cdot 10^{-5} = 5.53989\cdot 10^{-5}\, m^4$$

The ratio of increase in moment of inertia of the floor beam (IPE 180, whose MoI is $1.317 \cdot 10^5 m^4$) is given by:

$$\frac{I_{33y}^{cls*}}{I_{33}^{s}} = \frac{5.53989 \cdot 10^{-5}}{1.317 \cdot 10^{-5}} = 4.21 \qquad (4.4.9)$$

Modal analysis has been performed using the increased moment of inertia for the floor beams, accounting for their connectivity with the reinforced concrete slab. In order to match the results of dynamic characterization tests, it has been found that translational mass along X and Y directions have to be approximately 4290 kg (slab and coffer only). As these values largely differ from those given in first row of Table 4.4 and also considering the fact that during model fabrication, connectivity between floor beams and slab was quite weak and made just to support the vertical loads, it was decided to completely ignore the rigidity between the floor beams and reinforced concrete slab in the further analysis.

4.5 Free vibration analyses results

The dynamic characteristics of the developed analytical models are determined and the results tabulated. Table 4.6 shows the structural frequencies and time periods of all the three configurations, evaluated analytically. Table 4.7 shows the modal participating mass of the analytical models being analyzed.

Table 4.6 Dynamic characterization (analytical) of the frame with different configurations.

Mode description	Bare frame		Symmetric frame with added mass		Asymmetric frame with added mass	
	f (Hz)	T (s)	f (Hz)	T (s)	f (Hz)	T (s)
1st translational mode (Y dir)	3.44	0.291	2.92	0,343	3.13	0.320
1st translational mode (X dir)	4.08	0.245	3.46	0.289	3.70	0.270
1st torsional mode	5.56	0.180	4.90	0.204	5.24	0.191
2nd translational mode (Y dir)	10.5	0.095	8.93	0.112	9.62	0.104
2nd translational mode (X dir)	14.5	0.069	12.3	0.081	13.2	0.076
2nd torsional mode	18.2	0.055	16.1	0.062	17.2	0.058

Table 4.7 Modal participating mass of the analytical models in different configurations.

Mode description	Bare frame	Symmetric frame with added mass	Asymmetric frame with added mass
1^{st} translational mode (Y dir)	79%	80%	80%
1st translational mode (X dir)	79%	81%	79%
1^{st} torsional mode	24%	23%	28%
2^{nd} translational mode (Y dir)	7.2%	7.5%	7.4%
2^{nd} translational mode (X dir)	9.9%	10%	9.9%
2^{nd} torsional mode	2.5%	2.5%	3.3%

Figure 4.16, Figure 4.17 and Figure 4.18 finally show the graphical representation of different vibrating modes of all the three configurations. It can be seen that first translational mode occurs along Y axis followed by the one along X axis for all the cases investigated. As expected, time period of the frame increases with addition of masses to each floor. The modal participating mass ratios (Table 4.7) clearly indicate the dominant axis of mode vibration in the case of bare frame and symmetric frame with added mass while show marginal contribution of participating mass in the torsional mode indicating asymmetric effect in case of the frame with eccentric added mass.

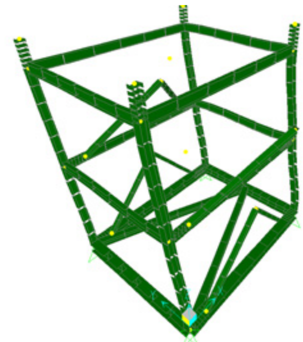	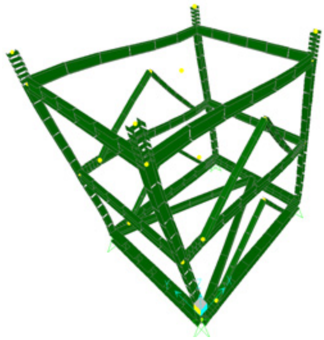
1st translational mode in Y direction (3.44 Hz)	1st translational mode in X direction (4.08 Hz)
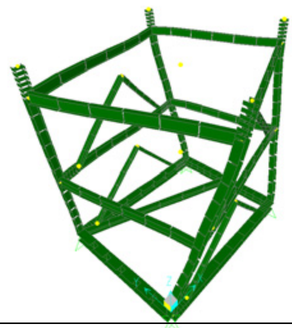	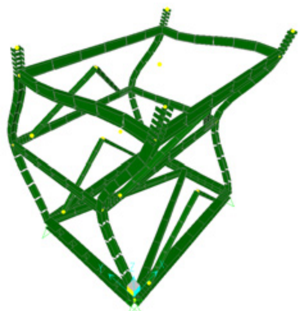
1st torsional mode (5.56 Hz)	2nd translational mode in Y direction (10.5 Hz)
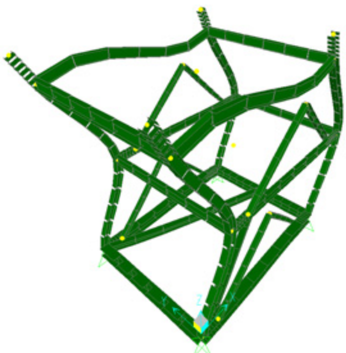	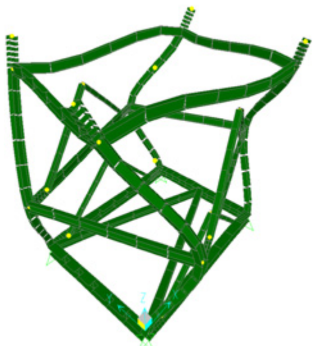
2nd translational mode in X direction (14.2 Hz)	2nd torsional mode (18.2 Hz)

Figure 4.16 Mode shapes of the bare frame (CB).

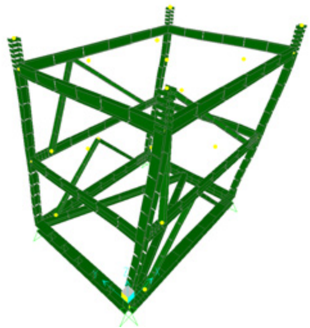	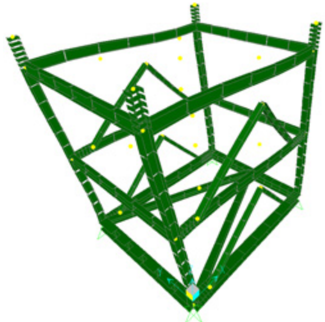
1st translational mode in Y direction (2.92 Hz)	1st translational mode in X direction (3.46 Hz)
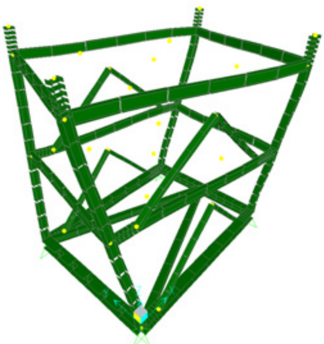	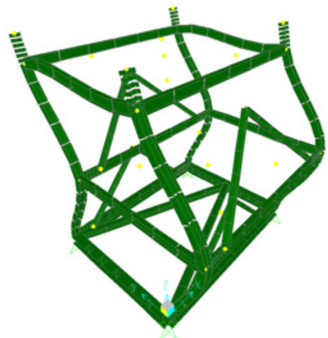
1st torsional mode (4.90 Hz)	2nd translational mode in Y direction (8.93 Hz)
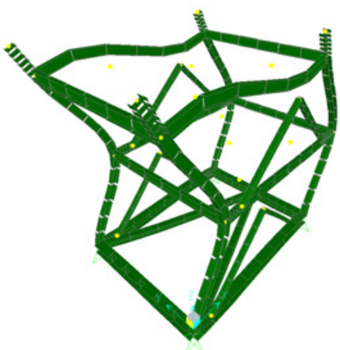	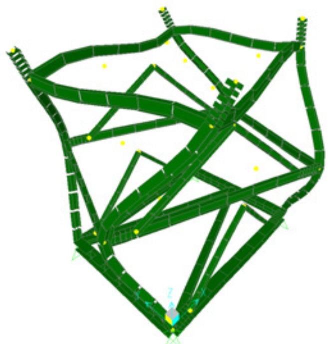
2nd translational mode in X direction (12.3 Hz)	2nd torsional mode (16.1 Hz)

Figure 4.17 Mode shapes of the frame structure in configuration CS.

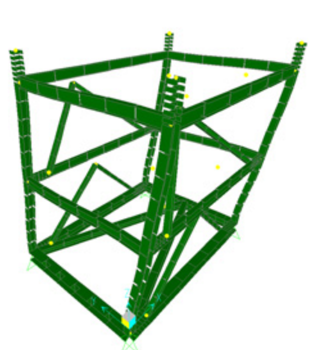	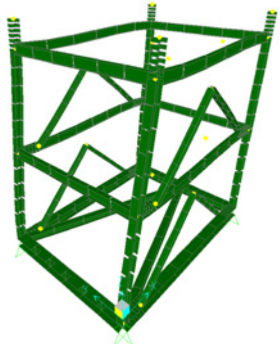
1st translational mode in Y direction (3.13 Hz)	1st translational mode in X direction (3.70 Hz)
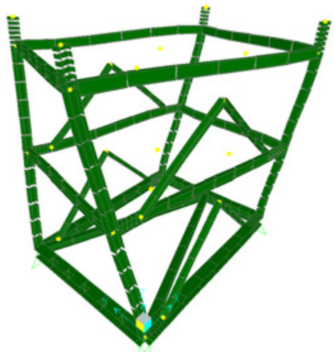	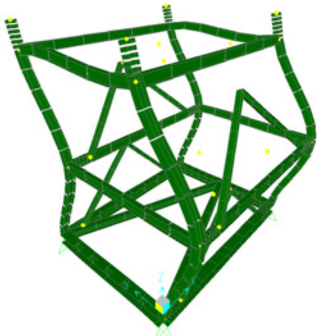
1st torsional mode (5.24 Hz)	2nd translational mode in Y direction (9.62 Hz)
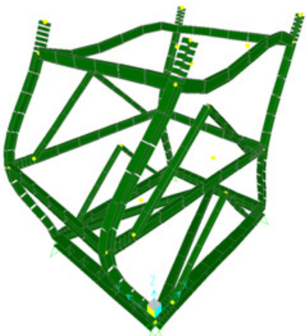	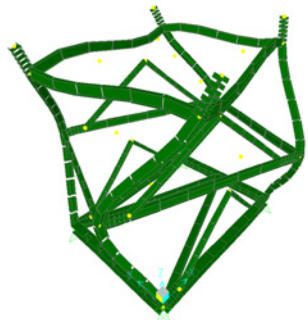
2nd translational mode in X direction (0.081 Hz)	2nd torsional mode (17.2 Hz)

Figure 4.18 Mode shapes of the frame structure in configuration CN.

4.6 Comparison with dynamic characterization test results

The results obtained from the analytical models are compared with those obtained from the experimental characterization tests conducted at University of Basilicata, Potenza (Gattulli *et al.*, 2007).

Table 4.8 shows the comparison of the results.

Table 4.8 Comparison of the analytical and experiemntal results of the frame in different configurations.

Mode description	Bare frame f (Hz)		Symmetric frame with added mass f (Hz)		Asymmetric frame with added mass f (Hz)	
	Analytical	Exp.	Analytical	Exp.	Analytical	Exp.
1st translational mode (Y dir)	3.44	3.38	2.92	2.85	3.13	3.08
1st translational mode (X dir)	4.08	4.23	3.46	3.58	3.70	3.84
1st torsional mode	5.56	5.89	4.90	5.11	5.24	5.51
2nd translational mode (Y dir)	10.5	9.41÷ 11.3	8.93	8.42	9.62	8.91
2nd translational mode (X dir)	14.5	14.6	12.3	12.4	13.2	13.0
2nd torsional mode	18.2	18.7	16.1	16.2	17.2	17.6

The masses used in the analytical tests are compared with those identified by experimental methods (Gattulli *et al.*, 2007) and the comparison is shown in Table 4.9.

Table 4.9 Comparison of masses of the analytical and experimental model.

Description	Method of analysis	First floor mass [kg]	Second floor mass [kg]
Bare frame	SAP model	3607	3385
	Experimental	3391.7	3351.0
Symmetric frame with added mass	SAP model	1350	1344
	Experimental	1350	1344

The rotational moment of inertia, accounting for the contributions from the floor beams, columns and additional mass is computed for comparing them with the experimental verifications. The revised rotational mass computed from Eq. 4.3.2 shows the contribution from the floor slab only. The contributions from other elements namely: *i)* the columns; *ii)* the floor beams; as well as *iii)* the additional mass is computed as below:

COLUMNS:

$$I_{xy,columns} = n_i \cdot \lambda_i h_i \cdot \left[\left(\frac{L_x}{2} \right)^2 + \left(\frac{L_y}{2} \right)^2 \right] \qquad (4.6.1)$$

where λ_i is the mass per unit length, h_i is the height of the column pertaining to each floor, n_i is the number of the columns per floor (Table 4.4) and L_x and L_y are the spans along X and Y directions, respectively.

a) first floor: $I_{xy,columns} = 277 \cdot \left[\left(\frac{3}{2} \right)^2 + \left(\frac{4}{2} \right)^2 \right] = 1731.25\, kg \cdot m^2$

b) second floor: $I_{xy,columns} = 202 \cdot \left[\left(\frac{3}{2} \right)^2 + \left(\frac{4}{2} \right)^2 \right] = 1262.5 kg \cdot m^2$

BEAMS:

For beams spanning along X axis the rotational MoI (Moment of Inertia) is given by:

$$I_{beamsX} = \mu \frac{L^3}{12} + \mu L a^2 \tag{4.6.2}$$

$$I_{beamsX} = 18.8 \frac{4^3}{12} + 18.8 \cdot 4 \cdot (1.5)^2 = 269.47\, kg \cdot m^2$$

where μ is the mass per unit length of the element, which is equal to 18.8 kg/m; a equals 3/2=1.5 m and L equals 4/2=2 m. Similarly for the beam spanning along Y axis, the rotational MoI is:

$$I_{beamsY} = \mu \frac{L^3}{12} + \mu L a^2 \tag{4.6.3}$$

$$I_{beamsY} = 18.8 \frac{3^3}{12} + 18.8 \cdot 3 \cdot (2)^2 = 267.9\, kg \cdot m^2$$

where a equals 4/2=2 m and L equals 3/2=1.5. Hence for all the four beams in each floor, it is computed as below:

a) for beams in first floor:

$$I_{xy,beams} = 2 \cdot (269.47 + 267.9) = 1074.74\, kg \cdot m^2$$

b) for beams in second floor:

$$I_{xy,beams} = 2 \cdot (269.47 + 267.9) = 1074.74\, kg \cdot m^2$$

BRACES:

For braces, projected length on the XY plane is determined. The mass per unit length of the element is given by:

$$\mu' = \frac{\mu}{\cos\theta} \tag{4.6.4}$$

$$\mu' = \frac{16.7}{\cos 39^\circ} = 21.489 \frac{kg}{m}$$

For braces of projected length on XY plane as 3.568 m, rotational MoI of each brace is given by:

$$I_{brace} = \mu \frac{L^3}{12} + \mu L a^2 \tag{4.6.5}$$

$$I_{brace} = 21.489 \frac{3.568^3}{12} + 21.489 \cdot 3.568 \cdot (1.5)^2$$

$$I_{brace} = 253.85 kg \cdot m^2$$

Therefore rotational MoI of braces is given by:

a) for braces on the first floor:

$$I_{xy,brace} = (2 \cdot 253.85) = 507.7 kg \cdot m^2$$

b) There is no contribution of the braces in the second floor.

Total rotational MoI, contributed from the above elements are summarized in Table 4.10:

Table 4.10 Computation of MoI for each element.

Element	Floor designation	
	First floor I_{xy} [kg·m^2]	Second floor I_{xy} [kg·m^2]
Column	1731.25	1262.5
Beams	1074.74	1074.74
Braces	507.71	Nil
Slab	6369	6369
Total I_{xy}	**9709.7**	**8733.24**

ADDITIONAL MASS FOR SYMMETRIC CONFIGURATION (similarly for asymmetric configuration):

For additional mass, the MoI is given by:

$$I_{add,mass} = I_{xy} + ma^2 \tag{4.6.6}$$

where I_{xy} is the rotational mass calculated as in equation 4.3.3, m is the mass of each concrete block and a is the distance from the center of each block to the center of the mass of the slab. Table 4.11 shows the computations.

Table 4.12 shows the comparison of rotational MoI determined analytically and experimentally.

Table 4.11 MoI for additional mass (CS configurations).

Added Mass	Floor	Position near to column	Mass [kg]	a [m]	I_{xy} [kg·m^2]
MA-I	I	A	338	1.362	669.23
MB-I	I	B	340	1.375	685.29
MC-I	I	C	336	1.377	679.08
MD-I	I	D	336	1.379	680.93
MA-II	II	A	336	1.362	665.27
MB-II	II	B	340	1.375	685.29
MC-II	II	C	338	1.377	683.12
MD-II	II	D	340	1.379	668.77

Table 4.12 Comparison of rotational MoI.

Description	Method of analysis	First floor mass [kg·m^2]	Second floor mass [kg·m^2]
Bare frame	SAP model	9709.7	8733.24
	Experimental	8162.2	8353.1
Symmetric frame with added mass	SAP model	12424.23	11435.69
	Experimental	10915.1	11093.7
Asymmetric frame with added mass	SAP model	11064.22	10083.80
	Experimental	9488.3	9679.1

4.7 Very good matching with experimental results

An extensive program of dynamic experimental tests named JetPacs (Joint Experimental Testing on Passive and semiActive Control Systems), involving several partners from different Italian Universities, has been scheduled to be carried out at the Structural Laboratory of the University of Basilicata, Potenza, (Italy). Analytical FEM model of a composite two-storey steel framed structure with reinforced concrete floors has been prepared, to closely match the prototype frame having been experimentally investigated in Potenza. Three different configurations have been considered in order to investigate the effect of different types of devices on the behaviour of the steel frame. The fist one is constructed with the bare frame without any additional mass and is designated as CB; the second one is the frame with four additional concrete blocks at first and second floors close to each corner, designated as CS; the third one is the frame with two additional concrete blocks on first and second floors placed eccentric with respect to mass center, designated as CN. The model has been carried out considering the sagging effect on the both floors observed when the concrete was poured to create the cast-in-situ reinforced concrete slab. The response of the JET-PACS mock-up structure has been evaluated by applying properly scaled natural earthquakes. Comparison between the natural frequencies of the analytical models and those obtained from the dynamic characterization tests indicate a very good matching with the experimental results, for all the three different configurations.

Chapter V

5. BUCKLING AND ROLLOUT IN SEISMIC ISOLATION SYSTEMS

Many isolation systems, particularly in the early years of diffusion of the technology, adopted bearings that used dowelled shear connectors or were held in place by recessed plate connections. These were used since they were much simpler to design and manufacture than bolted connections but more importantly they reduced the possibility of tension stresses when the bearings are displaced in lateral shear. It was assumed at the time that the elastomer was not able to take much tension and the dowelled or recessed connection helped to eliminate these stresses. This was not a trivial concern since the quality of steel-rubber bonding at the time was not as well developed as it is today. After many years of improving the bonding of steel and rubber and many extensive bearing test programs it is now accepted that bearings are capable of sustaining quite high tensile stresses and it now common to use bolted connections (Marsico and Kelly 2008a).

However non-bolted connections have some advantages; they are cheap, their use avoids the contentious issue of how the bolts and the end plates have to be designed and they reduce the tensile stresses that could develop in the elastomer and in the bonding thus allowing a less strict bonding technique. The dowelled bearing was first used in the United States in the Foothill Communities Law and Justice Centre built in Rancho Cucamungo in 1983. (Figure 5.1 and Figure 5.2)

Figure 5.1 Foothill Communities Law and Justice Center. First isolated building in the United States. Dowelled isolators.

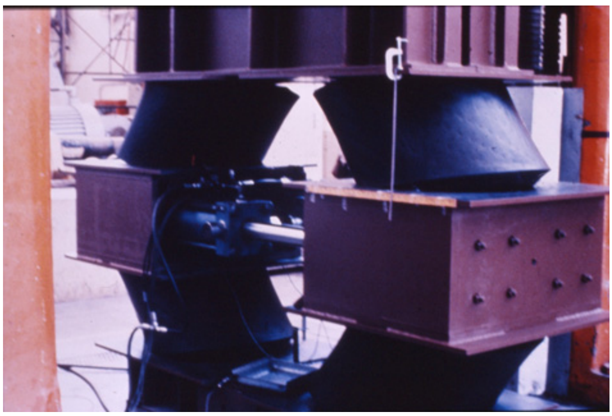

Figure 5.2 Testing of dowelled isolators at EERC showing uplift at edges of bearings.

The recessed connection was used in the SIP project in Ancona, Italy (Figure 5.3) in 1988. It was the first base isolated building in Italy.

Figure 5.3 Ancona SIP Building using Recessed Bearings.

The recessed connection has been used in projects in China and Indonesia and remains an option in projects in developing countries where a low-cost isolator system is essential. There are several isolated building projects in Armenia that use the recessed connection detail and an example of one these projects is a fifteen storey apartment building in Yerevan, shown in Figure 5.4 under construction.

The dowelled isolation bearing, even if stable against buckling under its design load, can experience another form of instability, called “roll-out”, that is associated with lateral displacement and which puts a limit on the maximum displacement that the bearing can sustain. Because the bearing cannot sustain tension, the balancing moment at the top and bottom of the bearing is produced by a change in the line of action of the resultant of the vertical load, as shown in Figure 5.5. The limit of the migration of the resultant is reached when the resultant is at the edge of the bearing, and the displacements beyond this will cause the isolator to roll, under decreasing load, away from its dowels or out of the recess in the end plate if recessed.

Figure 5.4 A five bearing set of recessed isolators in Yerevan building showing recessed connection.

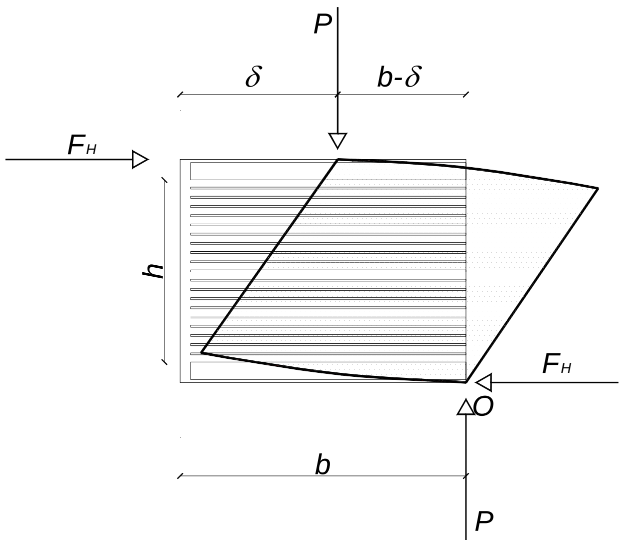

Figure 5.5 Mechanics of rollout for dowelled bearings.

There is also the issue of buckling load itself since the analysis of the buckling behaviour of a multilayer elastomeric isolator is based on fixed boundary conditions at the top and bottom of a bearing. Exactly how the doweled or recessed connection should be treated as a boundary condition for a buckling analysis is not clear.

5.1 Mechanics of Roll-Out and Buckling in Recessed Bearings

Several parameters control the buckling of a multilayer rubber bearing but the two most important are the shape factor usually denoted by S which is a measure of the thinness of each individual rubber layer in the bearing and the second shape factor S_2 which is a measure of the overall slenderness of the entire bearing. The first shape factor S enables the designer of the system to decide if the material can be considered incompressible or if the bulk modulus must be taken into account. For low to moderate values, up to perhaps 15, the material can be assumed incompressible but beyond this the material must be assumed compressible, a fact that considerably complicates the analysis.

Consider a bearing where t_r is the total height of rubber, t is the single layer thickness, t_s is the steel plate thickness and there are n layers so that $t_r = n \cdot t$ and the total height of the bearing is $h = t_r + (n-1)t_s$. To calculate the area we have to know the radius $R = \frac{\phi}{2}$ so the area is $A_{tot} = \pi R^2$. The horizontal initial stiffness is

$$K_H^0 = \frac{G \cdot A_{tot}}{t_r} \tag{5.1.1}$$

and the vertical stiffness is:

$$K_V = \frac{E_c \cdot A_{tot}}{t_r} \tag{5.1.2}$$

The value of the compression modulus E_c for a single rubber layer is controlled by the shape factor S which for a circular pad of diameter R and thickness t is:

$$S = \frac{R}{2t} \tag{5.1.3}$$

For a circular bearing with a moderate shape factor this compression modulus E_c is equal to $6GS^2$, with the assumption of incompressibility, and substituting the latter in the Eq.5.1.2 the vertical stiffness becomes:

$$K_V = \frac{6GS^2 \cdot A_{tot}}{t_r} \tag{5.1.4}$$

We denote the Euler load for the standard column by P_E and the shear stiffness per unit length by $P_S=GA_S$, in terms of which for most types of bearings where S is more than 5 and $P_E >> P_S$, the critical load P_{crit} can be approximated by:

$$P_{crit} = \left(P_S P_E\right)^{\frac{1}{2}} \tag{5.1.5}$$

where $P_S = GA\frac{h}{t_r}$, $P_E = \frac{\pi^2}{h^2}\left(\frac{1}{3}E_c I\right)\frac{h}{t_r}$, then

$$P_{crit} = \left(GA\frac{h}{t_r}\right)^{\frac{1}{2}}\left[\frac{\pi^2}{h^2}\left(\frac{1}{3}E_c I\right)\frac{h}{t_r}\right]^{\frac{1}{2}} \text{ so:}$$

$$P_{crit} = \left(\frac{\sqrt{2}\pi GASr}{t_r}\right) \tag{5.1.6}$$

where the radius of gyration r is $\phi/4$ for a circular bearing with diameter ϕ and $b/2\sqrt{3}$ for a square bearing with side dimension b.

The critical pressure $p_{crit}=P_{crit}/A$, can be expressed in terms of S and the quantity S_2, referred to as the aspect ratio or the second shape factor, denoted by $S_2=\dfrac{\phi}{t_r}$. Thus, assuming that the material can be considered incompressible, as previously mentioned, the estimate of the pressure at which a circular bearing will buckle is:

$$p_{crit}=\frac{\pi\cdot G}{2\sqrt{2}}S\cdot S_2 \qquad (5.1.7).$$

The basis of our approach to the buckling of the recessed bearing is the postulate that the onset of instability under lateral displacement is the critical pressure p_{crit} applied to the reduced area A_r, where A_r is defined to be the overlap area between the top and the bottom.

For a square bearing with area *bxb* where the displacement δ is parallel to one side, the reduced area is:

$$A_r=b\cdot(b-\delta) \qquad (5.1.8)$$

while for a circular bearing the reduced area and the lateral displacement are given respectively by:

$$A_r=2R^2\left(\frac{\pi}{2}-\varphi-\sin\varphi\cos\varphi\right) \qquad (5.1.9)$$

and

$$\delta=2R\cdot\sin\varphi \qquad (5.1.10)$$

where φ is shown in Figure 5.6 which also shows the overlap area A_r for a circular bearing with a generic displacement δ.

Thus the postulate is that the onset of instability in the displaced bearing is:

$$P_{crit} = p_{crit} \cdot A_r \tag{5.1.11}$$

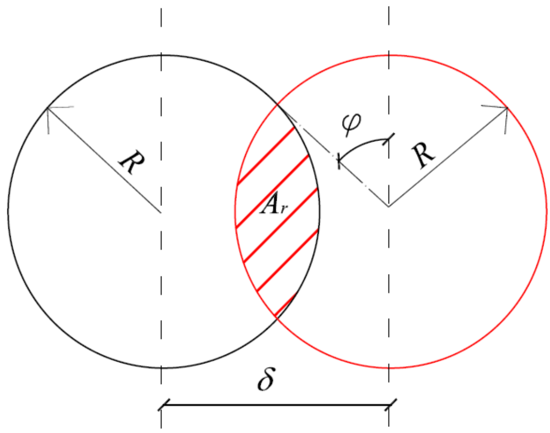

Figure 5.6 Displacement of a circular bearing.

The displacement due to roll-out is given by:

$$\delta_r = b\frac{1}{1+\dfrac{K_H h}{W}} \quad \text{for a square bearing} \tag{5.1.12}$$

$$\delta_r = \Phi\frac{1}{1+\dfrac{K_H h}{W}} \quad \text{for a circular bearing} \tag{5.1.13}$$

but if a vertical load W is present, the horizontal stiffness K_H is reduced through the application:

$$K_H(W) = K_H^0\left(1-\left(\frac{W}{P_{crit}}\right)^2\right) \tag{5.1.14}$$

The problem is to fix the applied vertical load W and then to apply a displacement and calculate the displacement that causes the bearing to be unstable either in terms of buckling δ_b or in terms of roll-out δ_r. We expect that for light loads W compared to P_{crit} in the undeformed position (denoted by P_{crit}^0) the instability will be roll-out but for large loads the instability will be buckling. We define a load parameter $w = \frac{W}{P_{crit}^0} = \frac{pA}{p_{crit}^0 A} = \frac{p}{p_{crit}^0}$ in terms of which the critical load producing the buckling is:

$$P_{crit}\left(\delta_b\right) = \frac{W}{p_{crit}\cdot A_r} = \frac{pA}{p_{crit}\cdot A_r} = w\cdot\left(\frac{A}{A_r}\right) \tag{5.1.15}$$

and the roll-out displacement becomes:

$$\delta_r = \phi\frac{1}{1+\dfrac{K_H^0\left(1-\left(\dfrac{W}{P_{crit}^0}\right)^2\right)h}{W}} = \phi\frac{1}{1+\dfrac{K_H^0\left(1-\left(w\right)^2\right)h}{w\cdot P_{crit}^0}}$$

$$\delta_r = \phi\frac{1}{1+\dfrac{\left(1-w^2\right)}{w}\cdot\dfrac{K_H^0 h}{P_{crit}^0}} \tag{5.1.16}$$

Considering Eq.5.1.16 we define the ratio $\frac{K_H^0 h}{P_{crit}^0} = \frac{\frac{GA}{t_r}\cdot h}{\frac{\sqrt{2}\pi GASr}{t_r}} = \frac{h}{\sqrt{2}\pi rS}$ where for a circular bearing with radius *R*, the radius of gyration is $r = \sqrt{\frac{I}{A}} = \frac{R}{2}$ so that the ratio becomes:

$$\frac{K_H^0 h}{P_{crit}^0} = \frac{h}{\sqrt{2}\pi \frac{R}{2} S} = \frac{\sqrt{2}h}{\pi RS} \tag{5.1.17}$$

and from this the roll-out displacement becomes:

$$\delta_r = \phi \frac{1}{1 + \frac{\left(1 - w^2\right)}{w} \cdot \frac{\sqrt{2}h}{\pi RS}} \tag{5.1.18}$$

For square bearing $r = \frac{b}{2\sqrt{3}}$ and the ratio from the Eq. 5.1.16 is:

$$\frac{K_H^0 h}{P_{crit}^0} = \frac{h}{\sqrt{2}\pi \frac{b}{2\sqrt{3}} S} = \frac{\sqrt{2}\sqrt{3}h}{\pi bS} \tag{5.1.19}$$

giving in this case the roll-out displacement:

$$\delta_r = \phi \frac{1}{1 + \frac{\left(1 - w^2\right)}{w} \cdot \frac{\sqrt{2}\cdot h}{\pi bS}} = b \frac{1}{1 + \frac{\left(1 - w^2\right)}{w} \cdot \frac{\sqrt{2}\cdot\sqrt{3}\cdot h}{\pi bS}} \tag{5.1.20}$$

while the buckling displacement $\frac{\delta_b}{b} = (1-w)$. The total height h depends on the design of the bearing but we can assume that it is typically of order of 1.2 t_r. which allows us to express the result in terms of the two shape factors as:

$$\delta_r = b\frac{1}{1+\frac{(1-w^2)}{w}\cdot\frac{\sqrt{2}\cdot\sqrt{3}\cdot 1.2}{\pi S S_2}} \qquad (5.1.21).$$

The shear-strain factor at design displacement D is denoted:

$$\gamma = \frac{D}{t_r} \qquad (5.1.22)$$

5.2 Inclusion of Bulk Compressibility

The Eq. 5.1.4 is the general formula for K_V where E_c depends from S. When the shape factor is larger we have to consider the effect of bulk compressibility K so the compression modulus is calculated as below:

$$\frac{1}{E_c} = \frac{1}{E_c^{\infty}} + \frac{1}{K} \qquad (5.2.1)$$

where E_c^{∞} is the effective compression modulus assuming incompressibility. Then $1 = \frac{E_c}{6GS^2} + \frac{E_c}{K} = E_c\left(\frac{1}{6GS^2} + \frac{1}{K}\right)$ and

$$E_c = \frac{6GS^2K}{K+6GS^2} = E_c^* \qquad (5.2.2).$$

in terms of which the Eq.5.1.4 becomes $K_V = \frac{E_c^* \cdot A_{tot}}{t_r}$. The bending stiffness for a single pad with a large shape factor is $\left(EI\right)_{eff} = 2GS^2 I\left(1 - \frac{3GS^2}{K}\right)$ where $I = Ar^2$. Then considering the P_E and P_S and substituting the value of K_V, the Euler load will be $P_E = \frac{\pi^2}{h^2} 2GS^2 I\left(1 - \frac{3GS^2}{K}\right)\frac{h}{t_r}$ and the critical load and the critical pressure become respectively:

$$P_{crit} = \frac{GS\pi Ar}{t_r}\left[2\left(1 - \frac{3GS^2}{K}\right)\right]^{\frac{1}{2}} \tag{5.2.3}$$

and

$$p_{crit} = \frac{P_{crit}}{A} \tag{5.2.4}$$

To calculate the displacement due to buckling we use the relation between the critical pressure and the reduced area as:

$$P_{crit}\left(\delta_b\right) = p_{crit} \cdot A_r = W \tag{5.2.5}$$

then from Eqs. 5.1.9 and 5.1.10 we obtain δ_b. The Eq. 5.1.16 becomes $\delta_r = \phi \frac{1}{1 + \frac{\left(1 - w^2\right)}{w} \cdot Z}$ where the ratio

$$Z = \frac{K_H^0 h}{P_{crit}^0} = \frac{h}{\pi Sr\left[2\left(1 - \frac{3GS^2}{K}\right)\right]^{\frac{1}{2}}}.$$

If we introduce the parameters $\delta_1 = \dfrac{\delta_r}{\phi}$ and $\delta_2 = \dfrac{\delta_b}{\phi}$ we can plot the function δ_1 (red line) and δ_2 (blue line) versus w as shown in Figure 5.7 referring to a circular bearing. We can observe that for large load the instability is buckling and for small load the instability is roll-out.

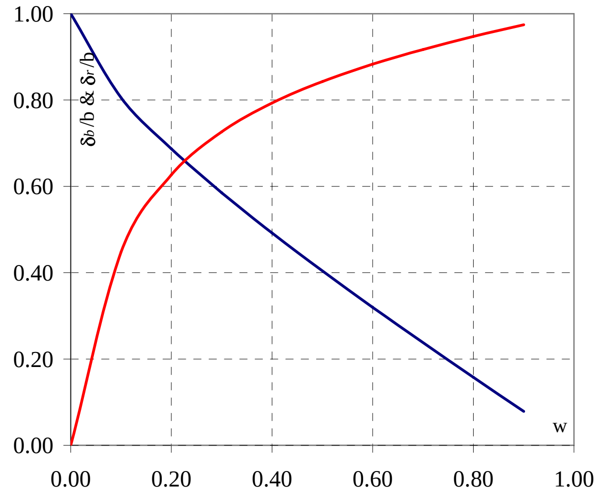

Figure 5.7 Buckling and roll-out displacement for circular bearing at the variation of *w*.

Like a circular bearing, we can introduce for a square bearing two parameters, $\delta_1 = \dfrac{\delta_r}{b}$ and $\delta_2 = \dfrac{\delta_b}{b}$, and observe the behaviour increasing w, as shown in Figure 5.8.

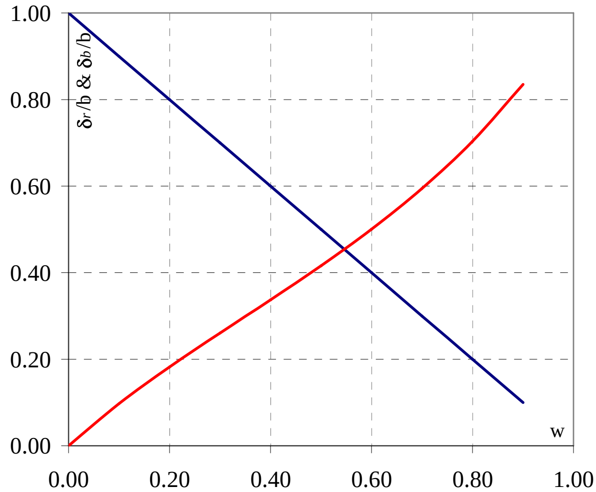

Figure 5.8 Buckling and roll-out displacement for square bearing at the variation of *w*.

5.3 Example: Application to Armenia design strategy

To illustrate the effect of these formulas we will apply them to bearings used in Armenia (Melkumyan, 2005) in several large apartment buildings both completed and currently under construction in Yerevan. As shown in Figure 5.4 the approach uses a set of smaller bearings, in this case five, each of 400 mm diameter instead of a single bearing as would be the case in other countries. The basis of this design approach is that a large number of smaller bearings is less expensive than a smaller number of large bearings with variable sizes that need to be designed for different column loads. The idea is that it is possible to adjust to the variable column loads by using one, two, three, four or five bearings under each column. There is also the feeling that having a set of several bearings will provide a redundancy not available when only a single bearing is used.

The only question of concern is that of the stability of a set of bearings as compared to a single bearing with the same horizontal stiffness. In this example we will base the design on five bearings with 400 mm diameter and study the stability, in terms of both roll-out and buckling, as compared to a single bearing of the same total area. The pressure, height of rubber and horizontal stiffness of the larger bearing will be the same as the five smaller bearings but the shape factor will differ. The design displacement will be assumed to be 250 mm.

We start with a rubber bearing with 16 rubber layers with the thickness of 8 mm each and 15 steel layers with diameter of 400 mm and thickness of 2 mm each; the pressure p is 6 MPa and the shear modulus G is 0.6 MPa. We want to design one large bearing to replace five identical 400 mm diameter bearings with the same number and thickness of rubber and steel layers as the latter, the same pressure and shear modulus. We apply a vertical load $5W_{(si)}$, equal to five times the vertical load applied to the single isolator and the horizontal stiffness of the large bearing is equal to five times the single horizontal stiffness.

Smaller bearing

First of all we design the small bearing where the height of rubber t_r is $t_r = n \cdot t = 16 \cdot 8 = 128mm$ and the total height is

$h = t_r + (n-1)t_s = 128 + (16-1)2 = 158mm$. We know the radius $R = \frac{\phi}{2} = \frac{400}{2} = 200mm$ so is possible to calculate the total area A_{tot} as $A_{tot} = \pi R^2 = \pi \cdot 200^2 = 125664mm$ to which is applied the load $W_{si} = p \cdot A_{tot} = 6 \cdot 125664 = 753982N$. The horizontal initial stiffness is, Eq. 5.1.1, $K_H^0 = \frac{G \cdot A_{tot}}{t_r} = \frac{0.6 \cdot 125664}{128} = 589N/mm$ and the vertical stiffness (Eq. 5.1.2), considering the shape factor (Eq. 5.1.3) given by $S = \frac{R}{2t} = \frac{200}{2 \cdot 8} = 12.5$ giving the compression modulus E_c for a circular bearing as $E_c = 6GS^2 = 6 \cdot 0.6 \cdot 12.5^2 = 562.5N/mm$, leading to $K_V = \frac{6GS^2 \cdot A_{tot}}{t_r} = \frac{562.5 \cdot 125664}{128} = 552233N/mm$.

The radius of gyration for this circular bearing of diameter ϕ as $r = \frac{\phi}{4} = \frac{400}{4} = 100mm$, and the critical load according to Eq. 5.1.6 is $P_{crit} = \left(\frac{\sqrt{2}\pi GASr}{t_r}\right) = 3271343N$. The shear-strain factor (Eq. 5.1.22) at design displacement D=250 mm is $\gamma_{(250)} = \frac{D}{t_r} = \frac{250}{128} = 1.95$. The reduced area associated with the displacement due to buckling (Eq. 5.2.5) depends on the critical pressure (Eq. 5.1.7), calculated in terms of the shape factor S and the second shape factor $S_2 = \frac{\phi}{t_r} = \frac{400}{128} = 3.13$, and is $A_r = \frac{W_{si}}{p_{crit}} = \frac{753982}{21.5} = 34961 mm^2$. Then we can calculate the angle φ and the buckling displacement (Eq. 5.1.10) respectively as $\varphi = 0.857 rad$ and $\delta_b = 2R \cdot \sin\varphi = 302 mm$.

The ratio between the applied load and the critical load *P* (or *W*) is $w = \frac{P}{P_{crit}^0} = \frac{753982}{3271343} = 0.23$ so the displacement δ_r (Eq. 5.1.18) is:

$$\delta_r = \phi \frac{1}{1 + \frac{\left(1 - w^2\right)}{w} \cdot \frac{\sqrt{2} \cdot h}{\pi SR}} = 400 \frac{1}{1 + \frac{\left(1 - 0,23^2\right)}{0,23} \cdot \frac{\sqrt{2} \cdot 158}{\pi 12,5 \cdot 200}} = 358 mm$$

Larger bearing

The load applied on the larger bearing is five times the load applied on the single one as $W_B = W_{si} \cdot 5 = 753982 \cdot 5 = 3769911 N$ so the total area of the big one will be $A = \frac{W}{p} = \frac{3769911}{6} = 628318 mm^2$. The radius is $R = \sqrt{\frac{A_B}{\pi}} = \sqrt{\frac{628318}{\pi}} = 447 mm$ and then the diameter is $\phi = 2R = 2 \cdot 447 = 894 mm$. The horizontal stiffness is $K_{H(B)} = 5 \cdot K_{H(si)} = 5 \cdot 589 = 2945 N/mm$ and the shape factor is

$S_B = \dfrac{R}{2t} = \dfrac{447}{2\cdot 8} = 28$. In this case the shape factor, more than 10-15, is so large enough that we have to introduce the bulk modulus *K*, (equal to 2000 MP) and calculate the effective compression modulus using (Eq. 5.2.2) giving $E_c = \dfrac{6GS^2K}{K+6GS^2} = E_c^* = \dfrac{2000\cdot 6\cdot 0,6\cdot 28^2}{2000+6\cdot 0,6\cdot 28^2} = 1169N/mm^2$. The vertical stiffness (Eq. 5.1.4) becomes $K_{V(B)} = \dfrac{E_c^* \cdot A_{tot}}{t_r} = \dfrac{1169\cdot 628318}{128} = 5737486N/mm$ and the critical load (Eq. 2.23) and the critical pressure (Eq. 5.2.4) are $P_{crit} = \dfrac{0.6\cdot 28\cdot \pi\cdot 628318r}{128}\left[2\left(1-\dfrac{30.6\cdot 28^2}{2000}\right)\right]^{\frac{1}{2}} = 44560786N$ where the radius of gyration $r = \dfrac{\phi}{4} = \dfrac{2\cdot 447}{4} = 223mm$ and $p_{crit} = \dfrac{P_{crit}}{A} = \dfrac{44560786}{628318} = 71N/mm^2$.

The buckling displacement (Eq. 5.1.10) is $\delta_b = 2R\cdot \sin\varphi = 2\cdot 447\cdot sin(0.973) = 739mm$ where the angle φ, calculated from Eq. 5.1.9, is $\varphi = 0,973rad$, and the roll-out displacement is $\delta_r = 2\cdot 447\dfrac{1}{1+\dfrac{\left(1-0.08^2\right)}{0.08}\cdot 0,01} = 796mm$ where the ratio $w = \dfrac{P}{P_{crit}^{0}} = 0.08$ and $Z = \dfrac{K_H^0 h}{P_{crit}^{0}} = \dfrac{\dfrac{0.6 \cdot 628318 \cdot 158}{128}}{44560786} = 0.01$

and the reduced area $A_r = \dfrac{3769911}{71} = 53157 mm^2$.

The conclusion that can be drawn from these results is that the set of smaller bearings will buckle at a displacement of 302 mm at the pressure of 6 MPa and that buckling is more critical than roll-out for this pressure. The single large bearing is also more susceptible to buckling than to roll-out and the buckling displacement is 739 mm. Both alternatives are stable at the design displacement of 250 mm but the safety factor is much large for the single bearing. The question for the design engineer is whether the increase in cost for the single bearing solution is justified by the increase in safety.

5.4 Stability and Post-Buckling Behaviour in Non-Bolted Elastomeric Isolators

The recent earthquakes in India, Turkey and South America have again emphasized the fact that the major loss of life in earthquakes happens when the event occurs in developing countries. Even in relatively moderate earthquakes in areas with poor housing many people are killed by the collapse of brittle heavy unreinforced masonry or poorly constructed concrete buildings. Modern structural control technologies such as active control or energy dissipation devices can do little to alleviate this but it is possible that seismic isolation could be adapted to improve the seismic resistance of poor housing and other buildings such as schools and hospitals in these countries.

The theoretical basis of seismic isolation shows that the reduction of seismic loading produced by the isolation systems depends primarily on the ratio of the isolation period to the fixed base period. Since the fixed base period of a masonry block or brick building may be of the order of 1/10 second, an isolation period of 1 sec. or longer would provide a significant reduction in the seismic loads on the building and would not require a large isolation displacement. For example, the current Uniform Building Code for seismic isolation (UBC, 2007) has a formula for minimum isolator displacement which, for a 1.5 second system, would be around 15 cm (6 inches).

The problem with adapting isolation to developing countries is that conventional isolators are large, expensive, and heavy. An individual isolator can weight one ton or more and cost as much as $10,000. To extend this valuable earthquake-resistant strategy to housing and commercial buildings, it is necessary to reduce the cost and weight of the isolators.

The primary weight in an isolator is due to the steel reinforcing plates, which are used to provide the vertical stiffness of the rubber-steel composite element. A typical rubber isolator has two large end-plates (25 mm) and 20 thin reinforcing plates (3 mm). The high cost of producing the isolators results from the labor involved in preparing the steel plates and laying-up of the rubber sheets and steel plates for vulcanization bonding in a mold. The steel plates are cut, sand-blasted, acid cleaned, and then coated with bonding compound. Next, the compounded rubber sheets with the interleaved steel plates are put into a mold and heated under pressure for several hours to complete the manufacturing process. Both the weight and the cost of isolators can be reduced by using thinner steel reinforcing plates, no end plates and no bonding to the support surfaces. Since the demands on the bonding between the rubber and the reinforcing plates are reduced, a simpler and less expensive manufacturing process can be used.

The manufacturing process for conventional isolators has to be done very carefully because the testing requirements in the current codes for seismic isolation require that the isolators be tested prior to use for very extreme loading conditions. The bond between the rubber and the steel reinforcement and between the rubber and the end plates must be very good for the bearing to survive these tests. The effect of a large shear displacement of the isolator is to generate an unbalanced moment that must be equilibrated by tensile stresses. The compression load is carried through the overlap region between top and bottom surfaces and the unbalanced moment is carried by tension stresses in the regions outside the overlap as shown in Figure 5.9. Bridge bearings are much less expensive than seismic bearings for buildings. The in-service demands on these bearings are, of course, much lower but the tests reported here have shown that even if displacements of seismic demand magnitude are applied to them they can deform without damage. The primary reason for this is the fact that the top and bottom surfaces can roll off the support surfaces and no tension stresses are produced. The unbalanced moments are resisted by the vertical load through offset of the force resultants on the top and bottom surfaces.

The bearings as tested in this test series survived very large shear strains comparable to those expected of conventional seismic isolators under seismic loading. However their cost is in the hundreds of dollars as compared to the cost of conventional isolators in the thousands of dollars.

While these isolators can undergo large displacements there is a concern with their stability. The conventional analysis for the buckling of isolators has focused only on isolators that are bolted at each end to rigid surfaces. The analysis is also based on the assumption that the steel reinforcing plates are essentially rigid but here the shims are very thin and bending of the shims could have an effect on the stability of these bearings. We will study the buckling of such a bearing and attempt to clarify the post-buckling behaviour based on the postulate that the vertical load in the buckled configuration is carried through the overlap area between top and bottom and that the triangular areas outside the overlap area are free of stresses. The approach will be done first for a bearing in the form of an infinite strip and then will be applied to a circular bearing. The reason for studying the strip is that the solution can be easily checked by a two-dimensional numerical model which might be considered as an experimental test.

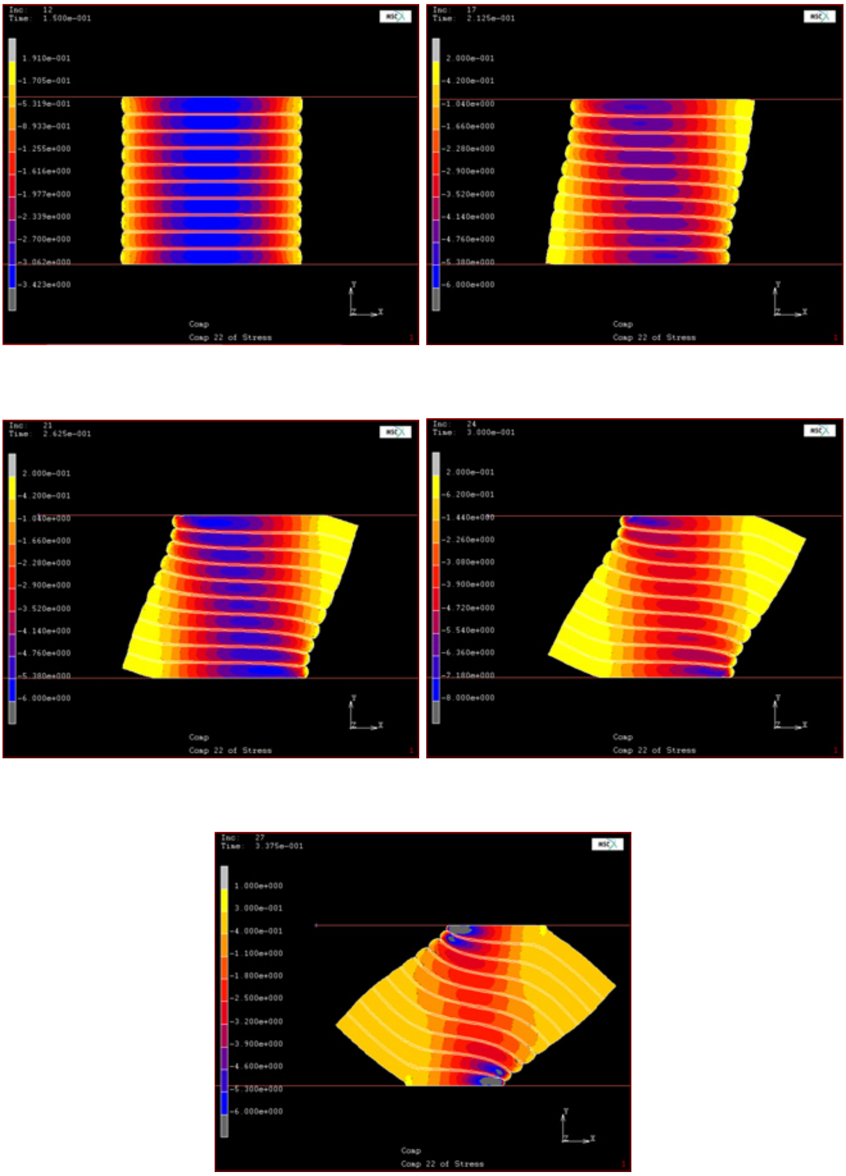

Figure 5.9 Tension stresses.

5.5 Numerical Experiment

The analysis to be covered in this paragraph is based on the idea that the isolator is placed in a displacement controlled test machine and subjected to a steadily increasing vertical displacement which will be denoted here by δ_V. This displacement manifests itself in the bearing in two parts, the first which is due to the axial shortening of the bearing due to pure compression and denoted by δ_V^O and the second due to the end shortening when the load reaches the critical load denoted by δ_V^G. When the displacement at which the load reaches the critical load is further increased the bearing can accommodate the increased load by lateral displacement and this lateral displacement denoted here by δ_H can be calculated from the end shortening part of the total vertical displacement.

The numerical experiment was done using the finite element program MARC. The model is two dimensional, corresponding to a long strip isolator and the reinforcing plates are modeled by elements which have an axial stiffness but no bending resistance. This is an extreme case of plate flexibility but it is used to simplify the numerical analysis. The model has contact elements at the top and bottom surfaces that allow it roll off the rigid supports and a small horizontal load is applied at the top to act as an imperfection and cause it to displace to one side when the load gets close to the buckling load.

The results are shown in the sequence of diagrams in Figure 5.9. The two triangular regions below and above the two roll out areas are free of stresses. When the vertical load is plotted against the vertical displacement (Figure 5.10) the load rises linearly until it gets close to the buckling load, then levels and then as the lateral displacement increases the vertical load diminishes.

This then is, at least qualitatively, the behaviour that we will attempt to reproduce analytically for a strip bearing and a circular bearing in the next two paragraphs.

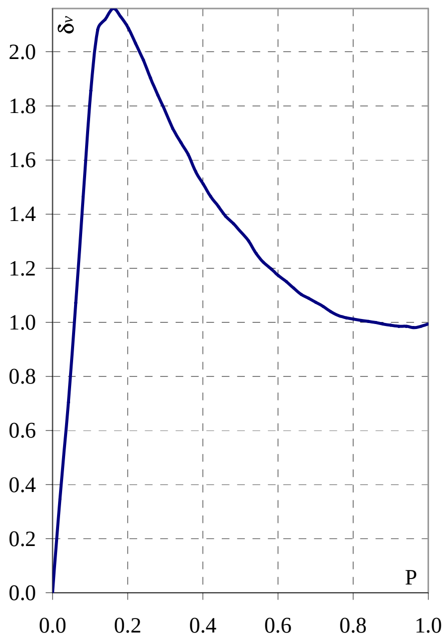

Figure 5.10 Unbonded bearing: diagram vertical force - vertical displacement.

5.6 Vertical Displacement of the Top of a Bearing for an Infinite Strip

The downward displacement of the top of a bearing due to a horizontal displacement is often needed in the design process, and this can be also calculated using the buckling analysis (Kelly and Marsico, 2008). The vertical displacement can be subdivided in two parts: the first one δ_V^G depends on the geometric characteristics and the second one δ_V^0 depends on the applied load.

For values of P between P_S=GA$_S$ and P_E, the Euler load for the standard column, the formula relating the vertical and the horizontal displacement is given by:

$$\delta_V^G = \frac{\alpha\beta h}{4}\left[\frac{\pi p - \sin \pi p}{(1-\cos \pi p)}\right]\frac{\delta_H^2}{h} \tag{5.6.1}$$

where $\alpha h\beta = \frac{Ph}{\left(EI_S GA_S\right)^{\frac{1}{2}}}\frac{GA_S}{P} = \frac{GA_S h}{\left(EI_S GA_S\right)^{\frac{1}{2}}} = \left(\frac{GA_S}{EI_S}\right)^{\frac{1}{2}} h$ with

$\alpha^2 h^2 = \frac{P^2 h^2}{EI_S GA_S}$, $\beta = \frac{GA_S}{P}$, and p equals to $\frac{P}{P_{crit}}$. When P=P_{crit} , the ratio $p=1$ and the Eq.5.6.1 becomes:

$$\delta_V^G = \frac{1}{4}\left(\frac{GA_S}{EI_S}\right)^{\frac{1}{2}}\frac{\pi}{2}\delta_H^2 \tag{5.6.2}$$

For an infinite strip of width 2b (Figure 5.11) the ratio $\frac{GA_S}{EI_S} = \frac{15t^2}{4b^4}$ because the area $A = 2b$; the compression modulus $E = 4GS^2$, the effective inertia $I_{eff} = \frac{1}{5}I$, the inertia $I = \left(\frac{2}{3}b^3\right)$ and the shape factor $S = \frac{b}{t}$.

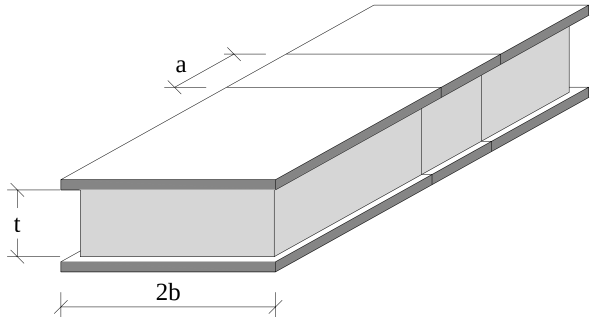

Figure 5.11 An infinite strip pad of width 2b.

If a load $P < P_{crit}$ is applied and the lateral displacement is not present, the effective area is the total area and the vertical displacement δ_V^G is:

$$\delta_V^G = \frac{1}{4}\frac{t}{4b^2}\sqrt{15}\pi\delta_H^2 = \frac{\pi}{16}\frac{t}{b^2}\sqrt{15}\delta_H^2 \tag{5.6.3}$$

On the other hand, the vertical displacement depending on the load, as $\delta_V^0 = \dfrac{Ph}{EA_S}$, considering the effective area $A_S = 2b\dfrac{h}{t_r}$ and the height $h = t_r$ is:

$$\delta_V^0 = \frac{Pt_r}{4G\dfrac{b^2}{t^2}2b} = \frac{Pt_r}{8G\dfrac{b^3}{t^2}} \tag{5.6.4}$$

If $P = P_{crit}$, where the critical load for an infinite strip is $P_{crit} = \dfrac{2\pi G 2b^3}{t \cdot t_r\sqrt{15}}$, the value of δ_V^0 will be:

$$\delta_V^0 = \frac{2\pi G 2b^3}{t \cdot t_r\sqrt{15}} \cdot \frac{t_r \cdot t^2}{8Gb^3} = \frac{\pi t}{2\sqrt{15}} \tag{5.6.5}$$

It means that when $P = P_{crit}$, δ_V^0 is a constant and it is not depending on the load. The total vertical displacement is equal to the sum of the two displacements calculated before as $\delta_V^t = \delta_V^G + \delta_V^0$.

The analysis of the experimental behaviour of the bearing can be subdivided in three steps:

1. the lateral displacement δ_H is not present, the vertical load P is $0 \le P < P_{crit}$, and the vertical displacement δ_V is applied (for example with a machine) (Figure 5.12);
2. the lateral displacement δ_H is not present, the vertical load P is $P = P_{crit}$, and the vertical displacement δ_V is applied (Figure 5.13);
3. the horizontal displacement δ_H is applied and the vertical load P is $P = P_{crit}$ calculated on the reduced area (Figure 5.14).

We define all the three steps calculated for an infinite strip as below:

<u>STEP 1</u>

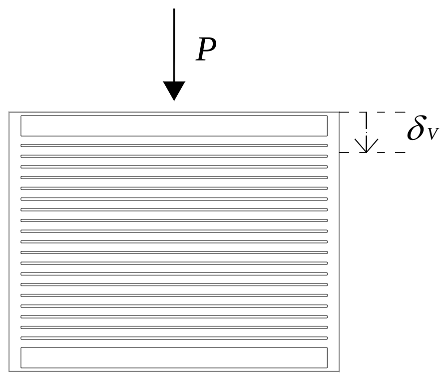

Figure 5.12 Step 1.

From Eq. 5.6.3 we know the total vertical displacement depending on the geometry, but because the horizontal displacement δ_H is not applied, the vertical displacement will be $\delta_V^G = 0$. From Eq. 5.6.4 we know the vertical displacement depending on the load, $\delta_V^0 = \dfrac{P t_r t^2}{8Gb^3}$ where $0 \le P < P_{crit}$. Then the total vertical displacement is:

$$\delta_V^t = 0 + \frac{P t_r t^2}{8Gb^3} = \frac{P t_r t^2}{8Gb^3} \tag{5.6.6}$$

<u>STEP 2</u>

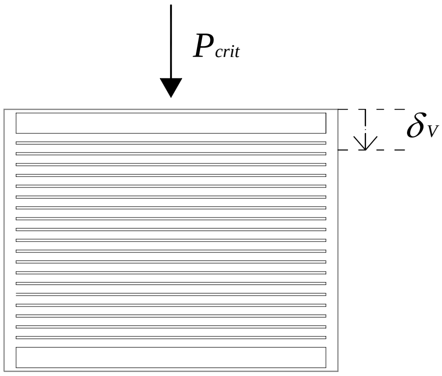

Figure 5.13 Step 2.

The vertical displacement depending on the geometry is the same of that calculated in the step 1. The vertical displacement depending on the load, when *P*= P_{crit} (Eq. 5.6.5) is $\delta_V^0 = \dfrac{\pi t}{2\sqrt{15}}$ so the total vertical displacement is:

$$\delta_V^t = 0 + \frac{\pi t}{2\sqrt{15}} = \frac{\pi t}{2\sqrt{15}} \tag{5.6.7}$$

STEP 3

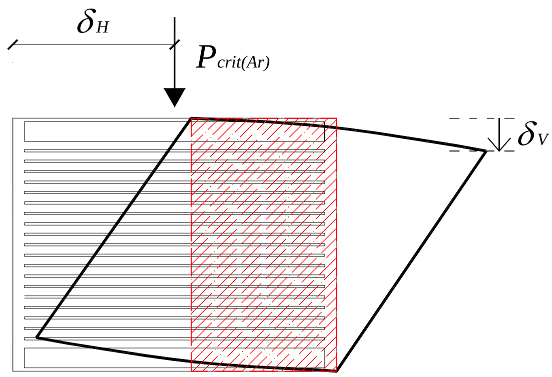

Figure 5.14 Step 3.

The value of the vertical displacement δ_V^G of width equals *2b* is given in the Eq. 5.6.3 but when is applied a horizontal displacement the effective area of the bearing is reduced and the width is $2b-\delta_H$. Therefore b becomes $b-\dfrac{\delta_H}{2}$ and the expression of δ_V^G becomes $\delta_V^G=\dfrac{\pi}{16}\dfrac{t}{\left(b-\dfrac{\delta_H}{2}\right)^2}\sqrt{15}\delta_H^2$ where $0\le\delta_H\le 2b$. When is applied the critical load on the reduced area the Eq.5.6.5 becomes $\delta_V^0=\dfrac{P_{crit(Ar)}t_r t^2}{8G\left(b-\dfrac{\delta_H}{2}\right)^3}$ and the expression of the total vertical displacement is:

$$\delta_V^t=\frac{\pi}{16}\frac{t}{\left(b-\dfrac{\delta_H}{2}\right)^2}\sqrt{15}\delta_H^2+\frac{\pi t}{2\sqrt{15}} \qquad (5.6.8)$$

where the value of δ_V^0 is a constant. Introducing $x = \dfrac{\delta_H}{2b}$ and $\delta = \dfrac{\pi t}{2\sqrt{15}}$ the Eq.5.6.8 becomes $\delta_V^t = \delta\left(1 + 15 \cdot \dfrac{x^2}{4(1-x)^2}\right)$ with $x \geq 0$, while the ratio $\dfrac{P_{crit(Ar)}}{P_{crit}} = \left(1 - \dfrac{\delta_H}{2b}\right)^3 = (1-x)^3$. Figure 5.15 shows the plot function of $y_1 = \dfrac{\delta_V^t}{2b}$ versus $y_2 = \dfrac{P_{crit(Ar)}}{P_{crit}}$ (blue line) and $y_1 = \dfrac{\delta_V^t}{2b}$ versus $y_3 = \dfrac{\delta_H}{2b}$ (pink line).

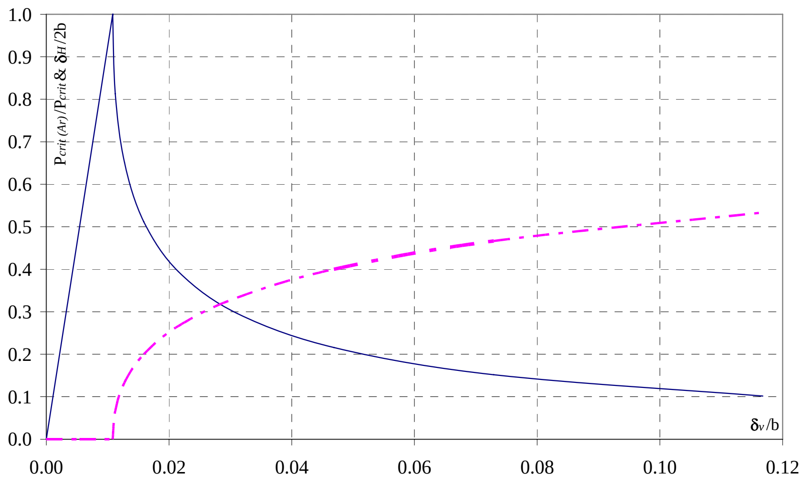

Figure 5.15 P_{crit}, horizontal and vertical displacement for an infinite strip bearing.

5.7 Vertical Displacement of the Top of a circular bearing

For a circular bearing the parameters to calculate the vertical displacement depending on the geometry are: $GA_S = G\left(\pi R^2\right)\frac{h}{t_r}$, the elasticity modulus $E_c = 6GS^2$, the shape factor $S = \frac{R}{2t}$ with R the radius, the effective inertia $I_{eff} = \frac{1}{3}I$, so the ratio $\frac{GA_S}{E_c I_S} = \frac{8t^2}{R^4}$.

At the end δ_V^G when $P < P_{crit}$ is:

$$\delta_V^G = \frac{1}{4}\frac{t\pi}{R^2}\sqrt{2}\delta_H^2 \qquad (5.7.1)$$

Using the Eq.5.6.4 with $P = P_{crit(Ar)} = \frac{\sqrt{2}\pi GASr}{t_r}$, denoted by $r = \frac{\phi}{4}$ the radius of gyration, the vertical displacement depending on load becomes:

$$\delta_V^0 = \frac{\sqrt{2}\pi t}{6}\frac{t_r}{h} \qquad (5.7.2).$$

For a circular bearing are valid the same procedures, regarding Steps 1 and 2, used for the infinite strip.

<u>STEP 1</u>

The stability condition of the bearing is that the horizontal displacement is not applied, and the load is $0 \le P \le P_{crit}$. The vertical displacement depending on the geometry is $\delta_V^G = \frac{1}{4}\frac{t\pi}{R^2}\sqrt{2}\delta_H^2 = 0$, the other one depending on the load is $\delta_V^0 = \frac{2P}{3G\pi h}\sqrt{\frac{t_r t}{R^2}}$, so the total vertical displacement is:

$$\delta_V^t = 0 + \frac{2P}{3G\pi h}\sqrt{\frac{t_r t}{R^2}} \tag{5.7.3}$$

STEP 2

Now the vertical load riches the value of the critical load $P = P_{crit}$ and the horizontal displacement is not applied, $\delta_H = 0$, so the vertical displacement depending on the geometry is $\delta_V^G = \frac{1}{4}\frac{t\pi}{R^2}\sqrt{2}\delta_H^2 = 0$ and the other one depending on the load is $\delta_V^0 = \frac{\pi\sqrt{2}t \cdot t_r}{6h}$. The latter like we know from the analysis of an infinite strip, is a constant (per $P = P_{crit}$). The total vertical displacement is:

$$\delta_V^0 = 0 + \frac{\pi\sqrt{2}t \cdot t_r}{6h} \tag{5.7.4}$$

STEP 3

When we applied a lateral displacement the effective area reduces. For an infinite strip the changed shape is square or rectangular but for a circle is not easy to define the new shape. We can consider approximately a circle with reduced radius with limit of leading the analysis for not large displacements (Figure 5.16).

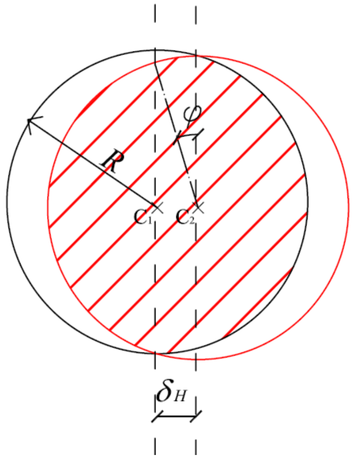

Figure 5.16 Overlap area.

The overlap area is denoted by $A_r = 2R^2\left(\frac{\pi}{2} - \varphi - \sin\varphi\cos\varphi\right) \cong 2R^2\left(\frac{\pi}{2} - 2\varphi\right)$ and the radius *R'* of the reduced circle is calculated as $R' = \sqrt{\frac{A_r}{\pi}} = \sqrt{\frac{2R^2\left(\frac{\pi}{2} - 2\varphi\right)}{\pi}}$. To know the vertical displacement depending on the geometry is used the Eq.5.6.3 where the ratio $\frac{GA_S}{EI_{rS}} = \frac{2}{S_r^2 R'^2}$ with $GA_S = G\pi R'^2 \frac{h}{t_r}$, the compression modulus $E_c = 6GS_r^2$ the shape factor $S_r = \frac{R'}{2t}$ and the effective inertia $I_{eff} = \frac{\pi R'^4}{12}$ so $\delta_V^G = \frac{1}{4S_r^2 R'^2}\sqrt{2}\frac{\pi}{2}\delta_H^2$. The Eq.5.6.4, expressed as $\delta_V^0 = \frac{Pt_r}{E_c A_{rS}}$ for a circular bearing, allows knowing the vertical displacement depending on the load as $\delta_V^0 = \frac{\sqrt{2}\pi t}{6}\frac{t_r}{h}$. At the end the total vertical displacement will be:

$$\delta_V^t = \frac{\sqrt{2}}{4S_r R'}\frac{\pi}{2}\delta_H^2 + \frac{\sqrt{2}\pi t}{6}\frac{t_r}{h} \tag{5.7.5}$$

Figure 5.17 shows $y_1 = \frac{\delta_V^t}{\phi}$ versus $y_2 = \frac{P_{crit(Ar)}}{P_{crit}}$ (blue line) and $y_1 = \frac{\delta_V^t}{\phi}$ versus $y_3 = \frac{\delta_H}{\phi}$ (pink line) for a circular bearing. We can observe the same curve progress defined for the infinite strip.

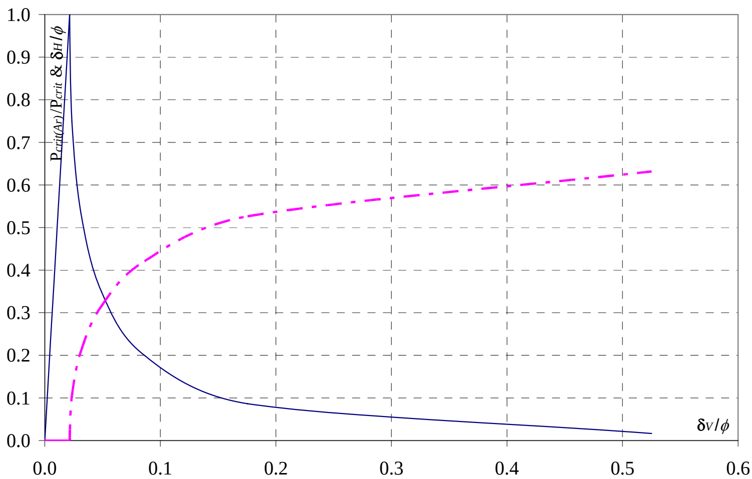

Figure 5.17 P_{crit}, horizontal and vertical displacement for a circular bearing.

5.8 Buckling Displacement of an Infinite Strip Bearing

Buckling and roll-out are the two fundamental problems of the stability analysis of these kinds of bearings. The theory used by many researches to study these phenomena is based on linearly elastic analysis. It is an approximation of the real behaviour of the devices but the results are satisfactory to the design process. The effects of the axial load (Figure 5.18) on the bearing are well known but the computation of the horizontal displacement is not clear because the buckling or the roll-out phenomenon are involved. The latter is present when the action line of the resultant of the load applied changes the initial position. So the equilibrium of the moment depends on the new configuration of the load and causes lateral displacements.

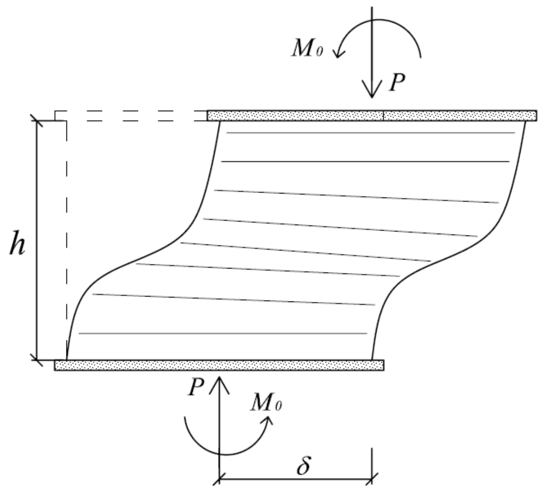

Figure 5.18 Bearing under vertical load.

The scope is to know the values of the horizontal displacement depending on the buckling or on the roll-out and define which one happens first. In this way we can define the cause of the instability for a certain applied load. The theoretical approach considers different types of geometry of the bearings and here we will demonstrate the behaviour by analyzing the stability of only the infinitely long strip. This is important also in its own right as it can be used to approximate the behaviour of long strip isolators that can be used in buildings with masonry walls.

A multilayered elastomeric bearing can be susceptible to a buckling type of instability similar to that of an ordinary column, but dominated by the low-shear stiffness of a bearing. The bearing in according its geometric characteristic can be studied as circular, square or infinite strip. The shape properties are known for all the types above listed but for the purpose of demonstrating the result using a simple approach the analysis is carried out only for the infinite strip bearing. In particular the behaviour under critical load is investigated. We consider an infinite strip where the shorter dimension is *2b* and the larger dimension is a unit length *a* as shown in Figure 5.11.

The scope is to know the critical load on the reduced area and investigate how this reduction depends on the increasing of the load. The calculation of the critical load based on the idea that buckling in the horizontally displaced position is associated with the overlap area between top and bottom which we will refer to as the effective total area. Given a shear modulus *G* and the area per unit length $A_{tot} = 2b \cdot a$, the buckling instability depends on the critical load $P_{crit} = (P_S \cdot P_E)^{\frac{1}{2}}$, and to know it we have to define some geometric characteristics of the isolator such as the shape factor, $S = \frac{b}{t}$, the radius of gyration, $r = \frac{b}{\sqrt{3}}$, the moment of inertia,

$I = \frac{2}{3}b^3$ and the compression modulus, $E_c = 4GS^2$, from which we have $(EI)_{eff} = \frac{4}{5}GS^2 I$ and then $P_{crit} = \frac{2\pi}{\sqrt{15}} G \frac{2b^3}{t \cdot t_r}$.

The procedure is to visualize that a certain value of horizontal displacement *D*, is applied aligned with the longitudinal dimension of the strip, for example by a machine, and then to calculate the critical load defined from the critical pressure on the reduced area of the section. As shown in Figure 5.19, as the horizontal displacement increases, the reduced area decreases and the critical load, given by $P_{crit}(D) = \frac{4\pi}{t \cdot t_r \sqrt{15}} G \left(b - \frac{D}{2} \right)^3$ decreases too.

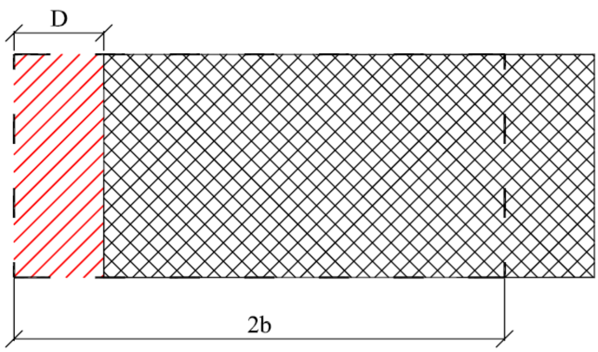

Figure 5.19 Reduced area.

We analyze the infinite strip bearing under an axial load and without the lateral displacement applied. We can then apply a lateral displacement to the top of the bearing increasing up to the maximum value corresponding to the width of the strip. In this case the maximum lateral displacement will be *2b* and the effective area reduced to zero. We can introduce two functions, $y_1 = \frac{D}{2b}$ and $y_2 = \frac{P_{crit}(D)}{P_{crit}^0} = \left(1 - \frac{D}{2b}\right)^3$, to describe the progress of the curve. The critical load is a cubical function of the displacement as shown in Figure 5.20 where y_2 is represented by the vertical axis and y_1 by the horizontal axis. The displacement starts at *0* where the critical load is calculated on the total area; as the critical load decreases as the effective area gets smaller and the displacement increases (Marsico and Kelly, 2008b).

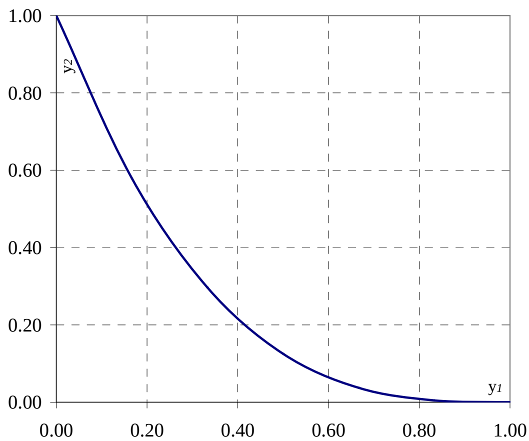

Figure 5.20 P_{crit} versus displacement.

We can apply a generic load on the bearing but is important to know the ratio with respect to the critical load. For this reason we define a parameter $f = \frac{W}{P_{crit}^0}$ where $0 \le f \le 1$, therefore *f* is equal 1 when the applied load is the critical load on the total area. If we want apply a load on the reduced area $W = P_{crit}(D)$, we have to impose $f = \left(1 - \dfrac{D}{2b}\right)^3$ (or $\dfrac{D}{2b} = 1 - \sqrt[3]{f}$). We can describe the progress of the lateral displacement at the variation of the load P. The functions $y_3 = \dfrac{\delta_b}{2b}$ and $y_4 = \dfrac{P}{P_{crit}}$ are represented in Figure 5.21) respectively on the vertical axis and on the horizontal axis where δ_b is the bucking displacement. The load applied is an inverse cubical function of the displacement.

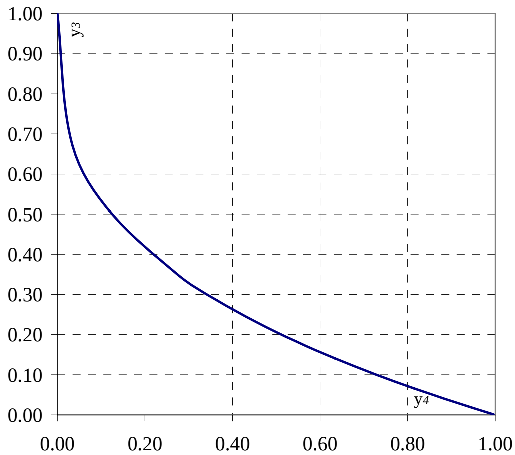

Figure 5.21 *P* versus displacement.

5.9 Roll-out for an infinite strip bearing with Horizontal stiffness affected by vertical load

Roll-out is another form of instability and it depends on the combination of the vertical and lateral force applied on the isolator. Figure 5.22 shows the roll-out mechanism during a test conducted at the Earthquake Engineering Center (University of California, Berkeley, USA) on a bearing which is not bonded top or bottom and where the shear transfer is through dowels allowing uplift at the edge. The limit of the migration of the resultant in the roll-out phenomenon is given by balance of moment as $F_H \cdot h = W\left(2b - D\right)$ considering the reduced area under a certain lateral displacement *D*. The relation between the lateral force F_H and the displacement *D* depends on the horizontal stiffness K_H so $F_H = D \cdot K_H$.

Figure 5.22 Roll-out test.

The horizontal stiffness is influenced by the lateral displacement *D* in fact when the effective area is reduced as $A_r = \left(2b - D\right)$ because *D*, it becomes $K_H\left(D\right) = \frac{dF_H}{dD} = \frac{G \cdot 2b}{t_r}\left(1 - \frac{2D}{2b}\right)$ and the lateral force F_H will be $F_H = \frac{G \cdot \left(2b - D\right)}{t_r} D$. When a vertical load is applied the general formula of the horizontal stiffness may be modified. We introduce a parameter f that relates a generic applied vertical load with the critical load of the bearing in undeformed configuration as $W = f \cdot P_{crit}^{0}$.

Many studies, based on the relation between the lateral force and the axial load, have led to an approximation of K_H valid when P is near P_{crit} given by $K_H = \frac{GA_S}{h}\left[1-\left(\frac{P}{P_{crit}}\right)^2\right]$. The horizontal force in terms of f is $F_{H(D)} = \frac{G \cdot D}{t_r}\left(2b-D\right)\cdot\left[1-\frac{f^2}{\left(1-\frac{D}{2b}\right)^6}\right]$ with the critical load on the reduced $P_{crit(D)} = \left(1-\frac{D}{2b}\right)^3 \cdot P_{crit}^{0}$. We can define the expression of the P_{crit} of the total area as $P_{crit}^{0} = \frac{2\pi}{\sqrt{15}}\cdot G \cdot \frac{2Sb^2}{t_r}$ so the equilibrium becomes: $D\cdot\left[1-\frac{f^2}{\left(1-\frac{D}{2b}\right)^6}\right] = f \cdot \frac{2\pi}{\sqrt{15}}\cdot\frac{2Sbr}{t_r \cdot h}$ where the radius of gyration is $r = \frac{b}{\sqrt{3}}$. The most common shape factor values of used bearings are 10-15. If we take for example S=10, the ratio

$\frac{r}{h} \approx 1$ and we introduce the function $x = \frac{D}{2b}$ we can know the curve progress of $x \cdot \left[1 - \frac{f^2}{(1-x)^6}\right] - f \cdot \frac{2\pi}{\sqrt{15}} \cdot S = 0$.

We observe that the force F_H in terms of the first and second shape factor, and normalized as $\frac{F_H}{P_{crit}^0}$ is equal zero as per $\frac{D}{2b} = 0$ and per $\frac{D}{2b} = 1$. Figure 5.23 shows an example for an infinite strip with *2b*=80 cm where the parameter $z = \frac{F_H}{P_{crit}^0}$ is represented on the vertical axis and the displacement is represented on the horizontal axis. When the lateral force increases, the displacement increases but there is a limit value after that the force decreases but the displacement increases so it has a parabolic behaviour.

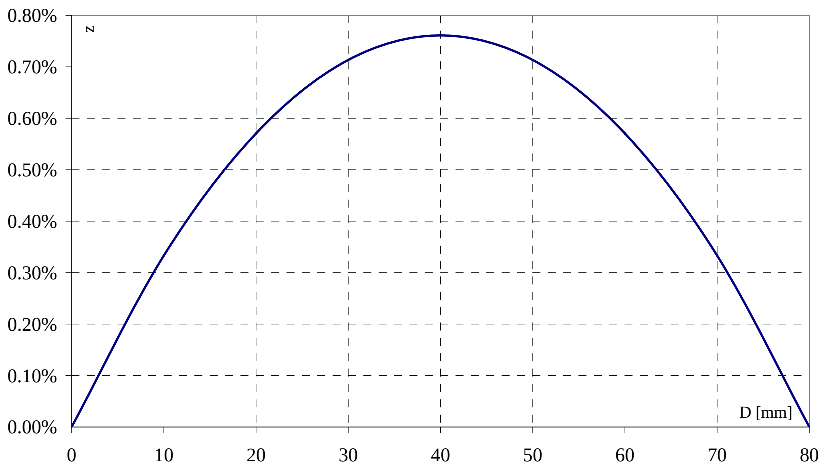

Figure 5.23 Example of lateral displacement versus *z*.

Considering the behaviour of the lateral force we can rewrite the equilibrium for the roll-out, normalized with respect to $2b \cdot P^0_{crit}$ as $\frac{F_H h}{2b \cdot P^0_{crit}} = \frac{f P^0_{crit}\left(2b - D\right)}{P^0_{crit}\, 2b \cdot} = f\left(1 - \frac{D}{2b}\right) = z_1$ and obtain that per $\frac{D}{2b} = 0, \frac{F_H h}{2b \cdot P^0_{crit}} = f$ and per $\frac{D}{2b} = 1, \frac{F_H h}{2b \cdot P^0_{crit}} = 0$. Figure 5.24 shows the rollout displacement for different values of *f*.

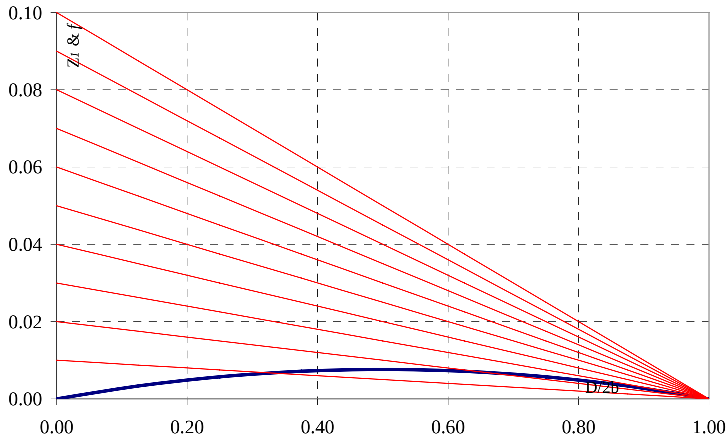

Figure 5.24 Roll-out equilibrium.

When the red line intersects the blue parabolic line there is the roll-out for a fixed value of *f* considering a certain horizontal force and therefore a lateral displacement. For large values of *f* the roll-out is in the descending part of the parabolic blue line so it happens after the buckling.

5.10 Effects of buckling and roll-out on the bearings

The instability due to the buckling and roll-out is an important phenomenon for non-bolted bearings. Is been hypothesized that the onset of instability under lateral displacement is the critical pressure p_{crit} applied to the reduced area A_r . For square bearings is very simple to calculate the reduced area but for circular bearings some approximations are necessary, in fact the reduced area is not a circle but is taken a circle when the analysis is led for not large displacements. The compression modulus used to define the critical load depends on the geometry and for bearings with large shape factor, this modulus changes because the effect of bulk compressibility K. Afterwards many analyses conducted on circular and square bearings it was deduced that in case of loads W lighter than P_{crit} of the bearing in the undeformed position, the instability is correlated to the roll-out; on the contrary, buckling is the main reason of the instability for loads larger than the critical value. These results are valuable for the design and the optimization of the geometric characteristics and to define the number of the isolators to put under each column of a structure. A good solution, but yet in experimental phase is the replacement of a big bearing with a set of small bearings. The problem is to know if the increase of the cost for a big one justifies a larger safety factor of the latter.

When a certain vertical load and a horizontal force are applied, a downward displacement at the top of the bearing is produced. The increase of the vertical load until the critical value can be accommodated by lateral displacement and this lateral displacement, δ_H, can be calculated as the end shortening part, δ_V^G, of the total vertical displacement. The analytical results are very good matching with the numerical results deduced from a Finite Element Model elaborated by Earthquake Engineering Center, Berkeley, California.

A parameter *f*, calculated as the load with respect to the critical load applied to the reduced area, can be introduced to know the behaviour of an infinite strip bearing with width *2b* and with a certain horizontal displacement applied. In particular smaller is *f*, easier is the roll-out. With these results we can know that the instability behaviour of the non-bolted bearings when are applied lateral and vertical loads and we can introduce the defined formulas in the design processes.

CONCLUSIONS

The research enveloped in this thesis was conducted in order to investigate the behaviour of structures with isolation and energy dissipation devices. The results are significant for the diffusion and application of these methodologies.

The most popular approach is to define Finite Element Models (with all the composing elements or with some approximations) for all the structures we are going to analyzed to simulate the response under seismic events.

The seismic isolation survey was conducted on the “Santuario della Madonna delle Lacrime”. Was carried out the complete mode of the Shine, with more than 2000 frames to know the modes and the stress tensions in all the elements. The seismic input is represented by 7 couples of artificial accelerograms compatible with the elastic response spectrum defined by the new code (Ministerial Decree of 14 January 2008) and for each accelerogram a duration of 26 s has been assumed. The results show that the intervention of seismic isolation of the dome from the columns determines a considerable reduction of the shear forces and bending moments in the piers, at the same time introducing dome’s displacements widely lower than those allowed by the new bearings.

The energy dissipation matter was worked out through the definition of the model of the scaled steel frame available at the Structural Engineering Laboratory of the University of Basilicata in

Potenza, Italy. The analysis had thee scope to design the mechanical and geometrical characteristics of the devices to be tested and the approach has been used to study a scaled frame. Were analyzed three different configurations both to elongate the vibration periods of the test frame and to consider the efficacy of the passive and semi-active devices in controlling the torsional behaviour The comparison between the natural frequencies of the analytical models and those obtained from the dynamic characterization tests indicate a very good matching with the experimental results, for all the three different configurations analyzed.

The common system of isolation is realized interposing structural elements with low horizontal stiffness between the structure and the foundation. Are usually used multilayer rubber bearing that produce however high stress tension. The solution could be the use of non-bolted bearing device because they reduce the tensile stresses that could develop in the elastomer and in the bonding thus allowing a less strict bonding technique and the simplification in the design.

It is well known that the behaviour of the non-bolted devices is associated with the horizontal displacements and the instability reaches for buckling and roll-out. Both these limit displacements under vertical loadings (i.e. in conditions of reduced stiffness) were considered.

For the bearings is possible to define the first and the second shape factors considering the geometric characteristics. When the primary shape factor is large, the effect of bulk compressibility K influences the compression modulus and the value of the critical load changes. In the case of loads W lighter than P_{crit} in the undeformed position, the instability is correlated to the roll-out; on the contrary, buckling is the main reason of the instability for large loads.

And important phenomenon of these devices is the vertical displacement. It can be divided in two parts: the first one δ_V^G depends on the geometric characteristics of the bearing and the second one δ_V^O depends on the load. Three different bearing configurations under vertical loads and lateral displacements were studied to know the real their self behaviour. The buckling analysis applied to all these models revealed that the bearing has significant horizontal drift under large vertical loads and the critical buckling load increases upon increasing the shape factor.

It was observed that when a certain horizontal displacement is applied, the effective area is reduced and the value of P_{crit} decreases, while the displacement increases. For an infinite strip bearing was defined the ratio f between the load and the critical load applied to the reduced area. The roll-out instability depends on f and smaller is f, easier is the roll-out.

REFERENCES

L'Industria Italiana del Cemento (IIC) (2001). *The "Santuario della Madonna delle Lacrime" in Siracusa*, , Year LXXI, n° 5, May 2001, p. 394-415.

L'Industria Italiana del Cemento (IIC) (2006). *The "Santuario della Madonna delle Lacrime"*, Special issue in the Italian r.c. structures for the 2° fib Congress, Napoli 5-8 June 2006, Year LXXVI, n° 5, May 2006, p. 350-353.

Bozorgnia Y., Bertero V. (2004). *Earthquake Engineering, form Engineering Seismology to Performance-Based Engineering,* pp.11.1-11.32.

Constantinou M.C. , Soong T.T. and Dargush G.F. (1998). Passive *Energy Dissipation Systems for structural Design and Retrofit,* Multidisciplinary Center for Earthquake Engineering Research, CAL.

Constantinou M.C. and Sigaher A.N. (2000). *Energy dissipation system configurations for improved performance*, 2000 Structures Congress, American Society of Civil Engineers, Philadelphia, PA.

Constantinou M.C., Tsopelas P., Hammel W. and Sigaher A.N. (2001). *Toggle-brace-damper seismic energy dissipation systems*, J. Structural Engineering, ASCE, 127, pp.105-112.

Federal Emergency Management Agency (FEMA) (2000). *NEHRP recommended provisions for seismic regulations for new buildings and other structures*, Chapter 9: Seismic isolation and energy dissipation, FEMA 356/ November 2000.

Federal Emergency Management Agency (FEMA) (2001). *Prestandard and commentary for the seismic design of new buildings*, Chapter 13: Seismic isolation and energy dissipation. FEMA 386/ November 2001.

Gattulli, V., Lepidi M., Potenza F. (2007). *Identification of analytical and finite element models for the JETPACS three-dimensional frame,* DPC-ReLUIS 2005-2008, Report No. 2, November 2007.

International Conference of Building Officials (ICBO) (1994). *Earthquake regulations for seismic-isolated structures,* Uniform Building Code, Appendix Chapter 16.

International Conference of Building Officials (ICBO) (1997). *Earthquake regulations for seismic-isolated structures*, Uniform Building Code, Appendix Chapter 16.

Kelly, J.M. (1988). *Base isolation in Japan*, Report No. UCB/EERC-88/20, Earthquake Engineering Research Center, University of California Berkeley, CA.

Kelly, J.M. (1990). *Base isolation: linear theory and design*, J. Earthquake Spectra, 6, 223-244.

Kelly, J.M. (2004). *Seismic isolation*, *Earthquake Engineering, form Engineering Seismology to Performance-Based Engineering*, pp.11.1-11.32.

Kelly, J.M. and Marsico, M.R. (2008). *Stability and Post-Buckling Behaviour in Non-Bolted Elastomeric Isolators*, J. Earthquake Spectra, *under review*.

Liu, W., M. Tong, Y. Wu, G. Lee. (2004). *Optimized damping device configuration design of steel frame structure based in building performance indices*, Eq. Spectra, Vol. 20, No. 1, pp. 67-89.

Marsico, M.R. and Kelly, J.M. (2008a). *Buckling and Roll-Out in Non-Bolted Elastomeric Isolators*, J. Earthquake Spectra, *under review*.

Marsico, M.R. and Kelly, J.M. (2008b). *Stability Analysis of an Infinite Strip Bearing*, J. Earthquake Spectra, *under review*.

Melkumyan, M.G. (2005). *State-of the art on application, R&D and design rules for seismic isolation of civil structures in Armenia*, 9th World Seminar Isolation, Energy Dissipation and Active Vibration Control of Structures, Kobe, Japan, June 13-16.

Ministry of Infrastructures, Ministerial Decree of 14 January 2008. *Nuove Norme tecniche per le Costuzioni* (Official Gazette No. 29 of 4 February 2008 – Ordinary Supplement No. 30) (In Italian).

Nicoletti, M., La Monaca, B.G. and Spina, D. (2005). *The Italian network for seismic monitoring of structures: Design, present level of realisation and further development.* Sixth European Conference on Structural Dynamics (EURODYN 2005), 4-7 September 2005 Paris, France.

Ponzo, F.C., Cardone D., Di Cesare A., Moroni C., Nigro D., Vigoriti G. (2007). D*ynamic tests on JETPACS steel frame: Experimental model setup*, JETPACS Report No. 3, Executive Project 2005-2008, ReLuis Project No. 7.

President of the Council of Ministers, Ordinance No. 3274 (2003). *First elements regarding the general criteria for the seismic classification of the national territory and technical standards for the constructions in seismic zone,* Roma, 20 March 2003 (In Italian).

President of the Council of Ministers, Ordinance No. 3431 (2005). *Further modifications and integrations to the Ordinance of the PCM n. 3274 of 20.03.2003,* Roma, 3 May 2005 (In Italian).

ReLUIS (2006). 1st year Report, Research Project No. 7, *Technologies for the seismic isolation and control of structures and infrastructures*, Executive Project 2005–2008.

Serino, G., Chandrasekaran, S., Marsico, M.R. and Spizzuoco, M. (2008). *Description and Analytical Modeling of the JET-PACS Prototype Steel Frame*, Report No. 1 - Research Project No. 7 - ReLUIS Executive Project 2005-2008, January 2008.

Serino, G., Spizzuoco, M., Marsico, M. R. (2006). *Prove in situ di carico e scarico su appoggi antisismici di una copertura in c.a*. Convegno Nazionale "Sperimentazione su materiali e strutture" Venezia, Italia 6-7 Dicembre 2006 (In Italian).

Serino, G., Spizzuoco, M., Marsico, M. R. (2007a). *Isolamento sismico del Santuario "Madonna delle Lacrime" in Siracusa*, XII Convegno Nazionale "L'Ingegneria Sismica in Italia" ANIDIS Pisa, 10-14 Giugno 2007 (In Italian).

Serino, G., Spizzuoco, M. and Marsico, M.R. (2007b). *The "Santuario della Madonna delle Lacrime" in Siracusa as Recent Application of Structural Isolation and Health Monitoring*, Secon International Conference "Experimental Vibration Analysis for Civil Engineering Structures" (EVACES'07), 24-26 October 2007 Porto (Portugal).

Serino, G., Spizzuoco, M., Marsico, M.R. and Chandrasekaran, S. (2008a). *The monitoring system of an isolated religious building in Italy: a recent acquisition of the Italian "OSS"* Fourth European Conference on Structural Control (4ECSC), 8-12 September 2008 St.Petersburg (Russia).

Serino, G., Spizzuoco, M., Marsico, M.R. and Chandrasekaran S. (2008b). *Seismic Isolation and Modeling of a Worship Structure*, Fourth European Conference on Structural Control (4ECSC), 8-12 September 2008 St.Petersburg (Russia).

Serino, G., Spizzuoco, M., Marsico (2008c). *Application of Structural Isolation and Monitoring. "The Our Lady of Tears Shrine" in Siracusa (Italy)*, Structure and Infrastructure Engineering - Maintenance, Management, Life-Cycle Design &Performance, *under review*.

Spizzuoco, M., Londoño, J.M., Serino, G., Marsico, M.R. (2008). *Design of non-linear viscous dampers for a steel braced mock-up structure*, Fourth European Conference on Structural Control (4ECSC), 8-12 September 2008 St.Petersburg (Russia).

Sigaher A.N. and Constantinou M.C. (2003). S*cissor-jack-damper energy dissipation system*, J. Earthquake Spectra, 19, pp.133-158.

Soong, T.T. and Dargush, G.F. (1997). *Passive Energy Dissipation Systems in Structural Engineering*, John Wiley & Sons, New York.

Staudacher, K. (1982). *Integral earthquake Protection of Structures Iv: Full Base Isolation and Seismic Mass Analogy*, Zurich, Switzerland.

Structural Engineers Association of California (SEAOC) (1985). *Recommended Lateral Design Requirements and Commentary*, Blue Book.

Structural Engineers Association of California (SEAOC) (1989). *General Requirements for the Design and Construction of Seismic-Isolated Structures*, Ad Hoc Base Isolation Subcommittee of the seismology Committee, Appendix to Chapter 1 of the SEAOC Blue Book.

Structural Engineers Association of Northern California (SEAONC) (1986). *Tentative Seismic Isolation Design Requirements*, Yellow Book.

UBC (2007). *Uniform Building Code*, International Code Council, Chapters 16-17.

Watanabe, A., Hitomi, Y., Saeki, E., Wada, A., and Fujimoto, M. (1988). *Properties of brace encased in buckling restrained concrete and steel tube*, Ninth World Conference on Earthquake engineering, Tokyo, Japan, 4, 719-723.